NASA TECHNICAL REPORT

NASA TR R-411

NASA TR R-411

CASE FILE COPY

REACTING VISCOUS-SHOCK-LAYER SOLUTIONS WITH MULTICOMPONENT DIFFUSION AND MASS INJECTION

by James N. Moss

Langley Research Center
Hampton, Va. 23665

NATIONAL AERONAUTICS AND SPACE ADMINISTRATION • WASHINGTON, D. C. • JUNE 1974

1. Report No. NASA TR R-411	2. Government Accession No.	3. Recipient's Catalog No.
4. Title and Subtitle REACTING VISCOUS-SHOCK-LAYER SOLUTIONS WITH MULTICOMPONENT DIFFUSION AND MASS INJECTION		5. Report Date June 1974 6. Performing Organization Code
7. Author(s) James N. Moss		8. Performing Organization Report No. L-8861
9. Performing Organization Name and Address NASA Langley Research Center Hampton, Va. 23665		10. Work Unit No. 502-07-01-05 11. Contract or Grant No.
12. Sponsoring Agency Name and Address National Aeronautics and Space Administration Washington, D.C. 20546		13. Type of Report and Period Covered Technical Report 14. Sponsoring Agency Code

15. Supplementary Notes

This paper is based in part upon a thesis entitled "Solutions for Reacting and Nonreacting Viscous Shock Layers With Multicomponent Diffusion and Mass Injection" submitted in partial fulfillment of the requirements for the degree of Doctor of Aerospace Engineering, Virginia Polytechnic Institute and State University, Blacksburg, Virginia, 1972.

16. Abstract

This study presents numerical solutions of the viscous-shock-layer equations where the chemistry is treated as being either frozen, equilibrium, or nonequilibrium. Also the effects of the diffusion model, surface catalysis, and mass injection on surface transport and flow parameters are considered. The flow is treated as a mixture of five inert and thermally perfect species. The viscous-shock-layer equations are solved by using an implicit-difference scheme.

All calculations are for hyperboloids with included angles of 20° and 45°. The flight conditions are those for various altitudes and velocities in the Earth's atmosphere. Data are presented to show the effects of the chemical models; diffusion models; surface catalysis; and mass injection of air on heat transfer; skin friction; shock standoff distance; wall pressure distribution; and tangential velocity, temperature, and species profiles.

The results show that an equilibrium analysis can substantially overpredict the heat-transfer rates for flow conditions experienced by earth-orbital entry vehicles. Moreover, at such conditions surface catalysis significantly influences heat-transfer and flow-field properties. If a binary rather than a multicomponent diffusion model is assumed, negligible errors in most flow properties result. Quantitative results are presented that show the effect of mass injection on flow properties within and downstream of the injection region.

17. Key Words (Suggested by Author(s)) Viscous shock layer Nonequilibrium Equilibrium Catalytic reactions Multicomponent diffusion		18. Distribution Statement Unclassified – Unlimited STAR Category 12	
19. Security Classif. (of this report) Unclassified	20. Security Classif. (of this page) Unclassified	21. No. of Pages 149	22. Price* $4.75

*For sale by the National Technical Information Service, Springfield, Virginia 22151

REACTING VISCOUS-SHOCK-LAYER SOLUTIONS WITH MULTICOMPONENT DIFFUSION AND MASS INJECTION*

By James N. Moss
Langley Research Center

SUMMARY

This study presents numerical solutions of the viscous-shock-layer equations where the chemistry is treated as being either frozen, equilibrium, or nonequilibrium. Also the effects of the diffusion model, surface catalysis, and mass injection on surface transport and flow parameters are considered. The flow is treated as a mixture of five inert and thermally perfect species. The viscous-shock-layer equations are solved by using an implicit-difference scheme.

All calculations are for hyperboloids with included angles of 20° and 45°. The flight conditions are those for various altitudes and velocities in the Earth's atmosphere. Data are presented to show the effects of the chemical models; diffusion models; surface catalysis; and mass injection of air on heat transfer; skin friction; shock standoff distance; wall pressure distribution; and tangential velocity, temperature, and species profiles.

The results show that an equilibrium analysis can substantially overpredict the heat-transfer rates for flow conditions experienced by earth-orbital entry vehicles. Moreover, at such conditions surface catalysis significantly influences heat-transfer and flow-field properties. If a binary rather than a multicomponent diffusion model is assumed, negligible errors in most flow properties result. Quantitative results are presented that show the effect of mass injection on flow properties within and downstream of the injection region.

INTRODUCTION

Analysis of the flow about a hypersonic vehicle must account for the interactions that occur between the reacting outer flow and the vehicle surface. This problem can be complicated in many cases because of either surface catalytic effects or mass injection. Furthermore, assumptions concerning the flow field, chemistry, and diffusion models may significantly affect the accuracy of an analysis for such a problem.

Numerical solutions to the aforementioned problem have been either inviscid-boundary-layer solutions (refs. 1 to 5, for example) or viscous-shock-layer solutions

---

*This paper is based in part upon a thesis entitled "Solutions for Reacting and Nonreacting Viscous Shock Layers With Multicomponent Diffusion and Mass Injection "submitted in partial fulfillment of the requirements for the degree of Doctor of Aerospace Engineering, Virginia Polytechnic Institute and State University, Blacksburg, Virginia, 1972.

(refs. 6 to 18, for example). The viscous-shock-layer equations as proposed by Davis and Flügge-Lotz (ref. 19) result in one set of equations uniformly valid throughout the shock layer. Consequently, the viscous-inviscid interactions are accounted for in a straightforward manner.

The most recent numerical solutions of the viscous-shock-layer equations are those given in references 6 to 10. These solutions are for stagnation and downstream flow and, with the exception of reference 9, are not restricted to the thin-shock-layer approximations. The viscous-shock-layer solutions presented in references 11 to 18 are for flow along the stagnation streamline. For the stagnation and downstream solutions, reference 7 considers atomic and molecular oxygen species by use of finite-rate chemistry; reference 8 considers the effects of injecting argon, air, and helium into air where air is treated as one species and the chemistry is either frozen or equilibrium; reference 9 considers nonequilibrium air as a reacting mixture of seven chemical species with constant but arbitrary Prandtl and Lewis numbers; and reference 10 extends the viscous-shock-layer solutions for both equilibrium and nonequilibrium chemistry to include all the following features: downstream solution capability, mass injection, and multicomponent diffusion. Also, the effect of the injection of water and ablation species into equilibrium air are considered in reference 10.

This study presents numerical solutions of the viscous-shock-layer equations for air. The chemistry is treated as being either frozen, equilibrium, or nonequilibrium. Particular attention is devoted to the effects of chemistry model, surface catalysis, diffusion model, and mass injection. The flow is treated as a mixture of five thermally perfect species (O, O_2, N, N_2, and NO). All calculations are for hyperboloids with included angles of 20° and 45°. The flight conditions are those for various altitudes and velocities in the Earth's atmosphere. Data are presented showing the effects of the chemical models; diffusion models; surface catalysis; and mass injection of air on heat transfer; skin friction; shock stand-off distance; wall pressure distribution; and tangential velocity, temperature, and species profiles. The results reported in reference 10 and herein are the first stagnation and downstream viscous-shock-layer solutions where the diffusion is treated as multicomponent.

SYMBOLS

a^*	body nose radius of curvature
a_1,a_2,a_3,a_4 a_5,a_6,a_7	coefficients of polynomial curve fits for thermodynamic properties (eqs. (B1) to (B3))
$B_{\ell k}$	quantity defined by equation (21)

Δb_{ik}	mass diffusion parameter defined by equation (18)
$\Delta \tilde{b}_{ik}$	mass diffusion parameter defined by equation (22)
C_f	skin-friction coefficient (eq. (45))
C_i	mass fraction of species i, ρ_i/ρ
$\tilde{C}_\ell$	mass fraction of element ℓ (eq. (10))
C_p	frozen specific heat of mixture, $\sum_i C_i C_{p,i}$
$C_{p,i}$	specific heat of species i, $C^*_{p,i}/C^*_{p,\infty}$
D^*_{ij}	multicomponent diffusion coefficients
$\mathcal{D}^*_{ij}$	binary diffusion coefficients
F^*	free energy of mixture
F^*_i	free energy of species i
H	total enthalpy of mixture (eq. (9)), H^*/U^{*2}_∞
h	enthalpy of mixture, $\sum_i C_i h_i$
h_i	enthalpy of species i, h^*_i/U^{*2}_∞
i, k, ℓ	integers
J_i	diffusion mass flux of species i, $J^*_i a^*/\mu^*_{ref}$
$\tilde{J}_\ell$	diffusion mass flux of element ℓ (eq. (12))
K	thermal conductivity of mixture, $K^*/\mu^*_{ref} C^*_{p,\infty}$
K^*_i	thermal conductivity of species i
K^*_{ij}	matrix coefficients defined by equation (B16)

$\bar{\bar{K}}^*_{ii}$	matrix coefficients (see eq. (B15))
$k^*_{b,r}$	backward rate constant
$k^*_{f,r}$	forward rate constant
L	arbitrary constant defined by equation (22)
M_∞	free-stream Mach number
M^*_i	molecular weight of species i
$\overline{M}^*$	molecular weight of mixture
$\dot{m}$	mass-injection rate, $\dot{m}^*/\rho^*_\infty U^*_\infty$
N_j	sum of reacting species and catalytic bodies
N_r	number of chemical reactions
N_s	number of reacting species
$N_{Le,i}$	Lewis number defined by equation (19)
$N_{Le,ik}$	multicomponent Lewis number, $\dfrac{\rho^* C^*_p D^*_{ij}}{K^*}$
N_{Pr}	Prandtl number defined by equation (A2)
$N_{Re,s}$	shock Reynolds number, $\rho^*_\infty U^*_\infty a^*/\mu^*_s$
$N_{Re,\infty}$	free-stream Reynolds number, $\rho^*_\infty U^*_\infty a^*/\mu^*_\infty$
N_{St}	Stanton number defined by equation (44)
n	coordinate measured normal to the body, n^*/a^*
PL_i	parameter defined by equation (C12e)
$\widetilde{PL}$	parameter defined by equation (C13e)

PM_i	parameter defined by equation (C12f)
$\widetilde{PM}_{\ell}$	parameter defined by equation (C13f)
p	pressure, $p^*/(\rho^*_\infty U^{*2}_\infty)$
p_i	partial pressure of species i
q	wall heat-transfer rate, $q^*/(\rho^*_\infty U^{*3}_\infty)$
R^*	universal gas constant
r	radius measured from axis of symmetry to a point on the body surface, r^*/a^*
s	coordinate measured along the body surface, s^*/a^*
T	temperature, $T^*\big/\left(U^{*2}_\infty\big/C^*_{p,\infty}\right)$
T^+	reduced temperature defined by equation (B12)
t^*	time
U^*_∞	free-stream velocity
u	velocity component tangent to body surface, u^*/U^*_∞
v	velocity component normal to body surface, v^*/U^*_∞
$\dot{w}_i$	mass rate of formation of species i, $\dot{w}^*_i a^*\big/\rho^*_\infty U^*_\infty$
X^*_i	concentration of species i, moles/volume
x_i	mole fraction of species i
α	shock angle defined in figure 1
$\alpha_{i,r}$	stoichiometric coefficients for reactants
α_r	quantity defined by equation (55)
$\alpha_1, \alpha_2, \alpha_3, \alpha_4$	coefficients in equation (C8)

$\beta_{i,r}$	stoichiometric coefficients for products
β_r	quantity defined by equation (56)
$\beta_1, \beta_{2,i}$	coefficients in equation (C27)
$\tilde{\beta}_1, \tilde{\beta}_{2,\ell}$	coefficients in equation (C32)
γ_j^*	mole mass ratio of species j (eq. (49))
γ_∞	free-stream ratio of specific heats
$\delta_{i\ell}$	number of atoms of ℓth element in species i
ϵ	Reynolds number parameter (eq. (A3))
ϵ_i^*	maximum energy of attraction of colliding i molecules
ϵ_{ij}^*	maximum energy of attraction of colliding unlike molecules
ζ	binary Lewis number
ζ_{ij}	variable binary Lewis number
$\hat{\zeta}$	constant binary Lewis number
η	transformed n coordinate, n/n_s
θ	body angle defined in figure 1
κ	body curvature, $\kappa^* a^*$
μ	viscosity of mixture, μ^*/μ_{ref}^*
μ_{ref}^*	reference viscosity (eqs. (A1))
ξ	coordinate measured along the body surface, $\xi = s$
ρ	density of mixture, ρ^*/ρ_∞^*

σ_i^*	collision diameter of species i
σ_{ij}^*	collision diameter for unlike species (eq. (B13))
ϕ_{ij}	quantity defined by equation (B9)
ψ	quantity defined by equation (C11e)
$\Omega_{ij}^{*(1,1)}$	collision integral for diffusion
$\Omega_{ij}^{*(2,2)}$	collision integral for viscosity

Subscripts:

i,j,k	ith, jth, and kth species
ℓ	ℓth elements
o	stagnation-point value
r	denotes rth reaction (see eqs. (52))
s	shock value
w	wall value
∞	free-stream condition
–	gas-solid interface value resulting from mass injection (see fig. 2)

Superscripts:

$C2_r$	a constant in equation that defines forward rate constant (eq. (53))
$D2_r$	a constant in equation that defines backward rate constant (eq. (54))
o	standard state (pure substance at 1 atmosphere of pressure)
j	zero for plane flow and one for axisymmetric flow

–	quantity divided by its corresponding shock value
*	dimensional quantity
'	total differential
''	shock oriented velocity components (see fig. 1)

ANALYSIS

A detailed development of the viscous-shock-layer analysis is presented because of the unique features of this analysis for studying problems such as those considered in this study and, also, the potential application of this analysis for studying much higher energy flow problems. The conservation equations and their associated boundary conditions are presented for the laminar viscous shock layer about an axisymmetric or two-dimensional body. These equations and boundary conditions account for mass injection and treat the diffusion as either multicomponent or binary. Equations convenient for solving frozen, equilibrium, and nonequilibrium flow are presented. Nondimensionalizing quantities are given, along with the transformation used to facilitate the numerical solution of the equations.

Shock-Layer Equations

The conservation equations that describe a reacting multicomponent gas mixture can be found in the literature. (For example, see ref. 20 or 21.) The viscous-shock-layer equations are obtained from the conservation equations by using the same procedure as given in reference 6. First, the conservation equations are written in the body-oriented coordinate system shown in figure 1. Then these equations are nondimensionalized in each of two flow regions with variables which are of order one. That is, the equations are nondimensionalized in the region near the body surface (boundary layer for large Reynolds numbers), and then the same set of equations is nondimensionalized in the essentially inviscid region outside the boundary layer. Terms in each of the two resulting sets of equations are retained up to second order in the Reynolds number parameter ϵ. By combining these two sets of equations so that terms up to second order in both the inner and outer regions are retained, a set of equations uniformly valid to second order in the entire shock layer is obtained.

The terms used to nondimensionalize the viscous-shock-layer equations are given in appendix A. The nondimensional viscous-shock-layer equations for a chemically reacting multicomponent gas mixture can be written as follows:

Global continuity:

$$\frac{\partial}{\partial s}\left[(r + n \cos\theta)^j \rho u\right] + \frac{\partial}{\partial n}\left[(1 + n\kappa)(r + n\cos\theta)^j \rho v\right] = 0 \tag{1}$$

s-momentum:

$$\rho\left(\frac{u}{1+n\kappa}\frac{\partial u}{\partial s} + v\frac{\partial u}{\partial n} + \frac{uv\kappa}{1+n\kappa}\right) + \frac{1}{1+n\kappa}\frac{\partial p}{\partial s}$$

$$= \epsilon^2\left\{\frac{\partial}{\partial n}\left[\mu\left(\frac{\partial u}{\partial n} - \frac{u\kappa}{1 + n\kappa}\right)\right] + \mu\left(\frac{2\kappa}{1 + n\kappa} + \frac{j\cos\theta}{r + n\cos\theta}\right)\left(\frac{\partial u}{\partial n} - \frac{u\kappa}{1 + n\kappa}\right)\right\} \tag{2}$$

n-momentum:

$$\rho\left(\frac{u}{1 + n\kappa}\frac{\partial v}{\partial s} + v\frac{\partial v}{\partial n} - \frac{u^2\kappa}{1 + n\kappa}\right) + \frac{\partial p}{\partial n} = 0 \tag{3}$$

Energy (temperature):

$$\rho C_p\left(\frac{u}{1 + n\kappa}\frac{\partial T}{\partial s} + v\frac{\partial T}{\partial n}\right) - \left(\frac{u}{1+n\kappa}\frac{\partial p}{\partial s} + v\frac{\partial p}{\partial n}\right)$$

$$= \epsilon^2\left[\frac{\partial}{\partial n}\left(K\frac{\partial T}{\partial n}\right) + \left(\frac{\kappa}{1 + n\kappa} + \frac{j\cos\theta}{r + n\cos\theta}\right)K\frac{\partial T}{\partial n} - \sum_{i=1}^{N_s} J_i C_{p,i}\frac{\partial T}{\partial n}\right.$$

$$\left. + \mu\left(\frac{\partial u}{\partial n} - \frac{\kappa u}{1 + n\kappa}\right)^2\right] - \sum_{i=1}^{N_s} h_i \dot{w}_i \tag{4}$$

Species continuity:

$$\rho\left(\frac{u}{1 + n\kappa}\frac{\partial C_i}{\partial s} + v\frac{\partial C_i}{\partial n}\right) = \dot{w}_i - \frac{\epsilon^2}{(1 + n\kappa)(r + n\cos\theta)^j}\left\{\frac{\partial}{\partial n}\left[(1 + n\kappa)(r + n\cos\theta)^j J_i\right]\right\} \tag{5}$$

and state:

$$p = \rho T\left(\frac{R^*}{\bar{M}^* C^*_{p,\infty}}\right) \tag{6}$$

This set of equations has a hyperbolic-parabolic nature (ref. 6), where the hyperbolic nature comes from the normal momentum equation. If the thin-shock-layer approximation is made, the normal momentum equation becomes

$$\frac{\partial p}{\partial n} = \frac{\rho u^2 \kappa}{1 + n\kappa} \tag{7}$$

When equation (3) is replaced with equation (7), the resulting set of equations is parabolic. Consequently, the equations can be solved by using numerical methods similar to those used in solving boundary-layer problems. After an initial iteration using equation (7), the final flow-field solution is obtained by replacing equation (7) with equation (3); thus the thin-shock-layer approximation is removed.

Equations (1) to (7) are the governing viscous-shock-layer equations. This set of equations is convenient to apply when the flow-field chemistry is assumed to be either nonequilibrium or frozen. However, when the flow field is assumed to be in chemical equilibrium, the production terms $\dot{w}_i$ that appear in the energy and species continuity equations cannot be obtained from the chemical kinetics. In this case, the production terms in the energy equation are eliminated by formulating this equation in terms of enthalpy. The energy equation in terms of total enthalpy is

$$\begin{aligned}
&\rho\left(\frac{u}{1 + n\kappa}\frac{\partial H}{\partial s} + v\frac{\partial H}{\partial n}\right) - v\frac{\partial p}{\partial n} + \frac{\rho\kappa u^2 v}{1 + n\kappa} \\
&\quad = \epsilon^2\left\{\frac{\partial}{\partial n}\left[\frac{\mu}{N_{Pr}}\frac{\partial H}{\partial n} - \frac{\mu}{N_{Pr}}\sum_{i=1}^{N_s} h_i\frac{\partial C_i}{\partial n} - \sum_{i=1}^{N_s} h_i J_i + \frac{\mu}{N_{Pr}}\left(N_{Pr} - 1\right)u\frac{\partial u}{\partial n} - \frac{\mu\kappa u^2}{1 + n\kappa}\right]\right. \\
&\qquad + \left(\frac{\kappa}{1 + n\kappa} + \frac{j\cos\theta}{r + n\cos\theta}\right)\left[\frac{\mu}{N_{Pr}}\frac{\partial H}{\partial n} - \frac{\mu}{N_{Pr}}\sum_{i=1}^{N_s} h_i\frac{\partial C_i}{\partial n} - \sum_{i=1}^{N_s} h_i J_i\right. \\
&\qquad \left.\left. + \frac{\mu}{N_{Pr}}\left(N_{Pr} - 1\right)u\frac{\partial u}{\partial n} - \frac{\mu\kappa u^2}{1 + n\kappa}\right]\right\}
\end{aligned} \tag{8}$$

where

$$H \equiv h + \frac{u^2}{2} \tag{9}$$

The production terms that appear in the species continuity equations are eliminated by introducing the concept of elemental mass fractions. As long as no nuclear reactions occur, the elemental mass fractions remain fixed and unchanged during chemical reactions. The relation between the elemental and species mass fractions (the Shvab-Zeldovich transformation (ref. 22)) is given by

$$\tilde{C}_\ell = \sum_{i=1}^{N_s} \delta_{i\ell} \frac{M_\ell^*}{M_i^*} C_i \tag{10}$$

The elemental continuity equations for the elements can be obtained by multiplying equation (5) by $\delta_{i\ell} \frac{M_\ell^* C_i}{M_i^*}$ and summing over i. The resulting elemental continuity equations are

$$\rho\left(\frac{u}{1 + n\kappa} \frac{\partial \tilde{C}_\ell}{\partial s} + v \frac{\partial \tilde{C}_\ell}{\partial n}\right) = -\frac{\epsilon^2}{(1 + n\kappa)(r + n \cos\theta)^j}\left\{\frac{\partial}{\partial n}\left[(1 + n\kappa)(r + n \cos\theta)^j \tilde{J}_\ell\right]\right\} \tag{11}$$

where

$$\tilde{J}_\ell = \sum_{i=1}^{N_s} \delta_{i\ell} \frac{M_\ell^*}{M_i^*} J_i \tag{12}$$

Introducing the elemental mass fraction not only eliminates the production terms in equations (4) and (5) but also reduces the number of equations to be solved, since there is one equation (eq. (11)) for each element rather than one equation (eq. (5)) for each species.

Equations (1) to (7) are the governing relations for frozen and nonequilibrium flow. Equations (4) and (5) are replaced with equations (8) and (11), respectively, for equilibrium flow. In these equations, additional relations are necessary to specify mixture quantities and the diffusion mass fluxes. Appendix B presents the relations that are used to calculate the thermodynamic and transport properties for each chemical species and the mixture transport properties. The values for the remaining mixture quantities are determined by the following relations:

Frozen specific heat:

$$C_p = \sum_{i=1}^{N_S} C_i C_{p,i} \tag{13}$$

where

$$C_i = \frac{\rho_i}{\rho} \tag{14}$$

Molecular weight:

$$\overline{M}^* = \frac{1}{\sum_{i=1}^{N_S} \frac{C_i}{M_i^*}} \tag{15}$$

Enthalpy:

$$h = \sum_{i=1}^{N_S} h_i C_i \tag{16}$$

where h_i includes the enthalpy of formation of the ith species.

The mass flux due to concentration gradients can be written as (ref. 1)

$$J_i = -\frac{\mu}{N_{Pr}} \sum_{k=1}^{N_S} \Delta b_{ik} \frac{\partial C_k}{\partial n} \tag{17}$$

where

$$\Delta b_{ik} = \left\{ \begin{array}{ll} N_{Le,i} & (i = k) \\ N_{Le,i} - \left[\frac{M_i^*}{\overline{M}^*} N_{Le,ik} + \left(1 - \frac{M_i^*}{M_k^*}\right) \sum_{j=1}^{N_S} N_{Le,ij} C_j \right] & (i \neq k) \end{array} \right\} \tag{18}$$

and

$$N_{Le,i} = \frac{\displaystyle\sum_{\substack{j=1 \\ j\neq i}}^{N_s} \frac{C_j}{M_j^*}}{\displaystyle\sum_{\substack{j=1 \\ j\neq 1}}^{N_s} \frac{C_j}{\zeta_{ij} M_j^*}} \tag{19}$$

In equations (18) and (19), $N_{Le,ij}$ are the multicomponent Lewis numbers and ζ_{ij} are the binary Lewis numbers. The relative mass flux for the elements can be written as

$$\tilde{J}_\ell = -\frac{\mu}{N_{Pr}} \left(L \frac{\partial \tilde{C}_\ell}{\partial n} + \sum_{k=1}^{N_s} B_{\ell k} \frac{\partial C_k}{\partial n} \right) \tag{20}$$

where

$$B_{\ell k} = \sum_{i=1}^{N_s} \delta_{i\ell} \frac{M_\ell^*}{M_i^*} \Delta\tilde{b}_{ik} \tag{21}$$

$$\Delta\tilde{b}_{ik} = \left\{ \begin{array}{ll} N_{Le,i} - L & (i = k) \\ \Delta b_{ik} & (i \neq k) \end{array} \right\} \tag{22}$$

and L is an arbitrary constant (generally taken as one). Equations (17) and (20) can be simplified to

$$J_i = -\frac{\mu}{N_{Pr}} \zeta \frac{\partial C_i}{\partial n} \tag{23}$$

and

$$\tilde{J}_\ell = -\frac{\mu}{N_{Pr}} \zeta \frac{\partial \tilde{C}_\ell}{\partial n} \tag{24}$$

respectively, for binary diffusion. Note that ζ is equal to either $\hat{\zeta}$, a constant binary Lewis number, or ζ_{ij}, a variable binary Lewis number.

Boundary Conditions

Conditions at the body surface.- The no-slip boundary conditions are used in this study. The surface conditions for $\eta = 0$ (see fig. 2) are

$$u = 0 \tag{25}$$

$$v = \frac{\dot{m}}{\rho} \tag{26}$$

where the mass-injection rate

$$\dot{m} = (\rho v)_- \tag{27}$$

is specified. In the calculations presented in this paper, the mass-injection distribution along the body surface is assumed to be

$$\dot{m} = \dot{m}_o e^{-3.47r^2} \tag{28}$$

where $\dot{m}_o$ is a specified stagnation-point mass-injection rate. This distribution is used to demonstrate the effect of mass injection on flow-field properties and to demonstrate the capability of the present analyses to account for distributed mass injection. The same distribution is used in reference 8.

The wall temperature for this study is specified as

$$T_w = \text{Constant} \tag{29}$$

The surface total enthalpy is given as

$$H = \sum_{i=1}^{N_s} h_i C_i \tag{30}$$

The surface boundary conditions for the elemental and species equations are derived as follows. (See fig. 2.) The species i are transported away from the surface at the rate J_i by diffusion and at the rate $\rho v C_i$ by convection. At the same time, the species i are being convected to the surface at the rate $\rho v C_{i-}$. This flux may be considered to be that from an ablating surface or the injectant from a porous solid. The surface species concentrations are given by

$$\rho v C_i + \epsilon^2 J_i = (\rho v C_i)_- \tag{31}$$

Since $\rho v = (\rho v)_- = \dot{m}$ (32)

equation (31) may be written as

$$\left(C_i - C_{i-}\right)\dot{m} = -\epsilon^2 J_i \tag{33}$$

and in terms of elemental boundary conditions as

$$\left(\tilde{C}_\ell - \tilde{C}_{\ell-}\right)\dot{m} = -\epsilon^2 \tilde{J}_\ell \tag{34}$$

Conditions at the shock.- The conditions imposed at the shock are calculated by using the Rankine-Hugoniot relations. The flow is assumed to be either in chemical equilibrium or frozen at the free-stream composition. The nondimensional shock relations are as follows:

Mass:

$$\rho_s v''_s = -\sin \alpha \tag{35}$$

$$u''_s = \cos \alpha \tag{36}$$

Momentum:

$$p_s = \frac{1}{\gamma_\infty M_\infty^2} + \sin^2 \alpha \left(1 - \frac{1}{\rho_s}\right) \tag{37}$$

Energy:

$$h_s = \frac{1}{M_\infty^2(\gamma_\infty - 1)} + \frac{\sin^2 \alpha}{2}\left(1 - \frac{1}{\rho_s^2}\right) \tag{38}$$

State:

$$p_s = \frac{\rho_s T_s R^*}{\bar{M}_s^* C^*_{p,\infty}} \tag{39}$$

Enthalpy:

$$h_s = \sum_{i=1}^{N_s} h_{i,s} C_{i,s} \tag{40}$$

Elemental composition:

$$\tilde{C}_{\ell,s} = \tilde{C}_{\ell,\infty} \tag{41}$$

and when the chemistry is frozen across the shock,

Species composition:

$$C_{i,s} = C_{i,\infty} \tag{42}$$

Surface transport.- The rate at which heat q is transferred to the surface boundary is given by the sum of the convective, conductive, and diffusion contributions. The net nondimensional heat transfer to the solid interior is given by

$$q = -\left[\epsilon^2\left(-K\frac{\partial T}{\partial n} + \sum_{i=1}^{N_s} J_i h_i\right) + \dot{m}\sum_{i=1}^{N_s}\left(C_i h_i - C_{i-} h_{i-}\right)\right]_w \tag{43}$$

The Stanton number is given by

$$N_{St} = -\frac{q}{H_\infty - H_w} \tag{44}$$

and the skin-friction coefficient is given by

$$C_f = 2\epsilon^2\left(\mu\frac{\partial u}{\partial n}\right)_w \tag{45}$$

A transformation is applied to the previous nondimensional viscous shock-layer equations and boundary conditions to simplify the numerical computations. The transformation relations and the transformed equations and boundary conditions are given in appendix C.

Chemical Composition

Analyses of chemically reacting flows are frequently simplified by considering the limiting cases of frozen and equilibrium chemical behavior. However, the question naturally arises: Which of these two limiting cases is more descriptive of reality? Of course, to answer this question the detailed finite-rate behavior of the chemical reactions must be accounted for. An analysis of a complex chemically reacting gas mixture, where the chemistry is nonequilibrium, presents problems that are not associated with either frozen or equilibrium treatments. These problems are primarily those of defining a realistic reactions model, of obtaining the appropriate rate constants, and of obtaining a numerical solution. In general, it is the latter problem that precludes a nonequilibrium treatment of reacting flows.

In this study, the chemical reactions will be confined to a system of neutral air species (O, O_2, N, N_2, and NO). However, the chemical models are not limited to this system of species.

Equilibrium.- The equilibrium chemical composition C_i is determined (for a given temperature, pressure, and elemental composition) by using a free-energy minimization analysis that is described in reference 23. Since the criterion for equilibrium at constant temperature and pressure is that the change in free energy be zero, $dF^* = 0$, the equilibrium composition is determined when the total free energy of the mixture is made a minimum with respect to any possible change in composition. Details concerning the equilibrium calculation can be found in reference 23.

Nonequilibrium.- When chemical reactions proceed at a finite rate, the rate of production terms $\dot{w}_i$ are required. The production terms appear in the energy equation (eq. (4)) when formulated in terms of temperature and in the species continuity equations (eq. (5)). For a multicomponent gas with N_s reacting chemical species and N_r chemical reactions, the chemical equation describing the overall change from reactants to products may be written in the general form

$$\sum_{i=1}^{N_j} \alpha_{i,r} X_i^* \underset{k_{b,r}^*}{\overset{k_{f,r}^*}{\rightleftharpoons}} \sum_{i=1}^{N_j} \beta_{i,r} X_i^* \tag{46}$$

where $r = 1, 2, \ldots, N_r$ and N_j is equal to the sum of the reacting species (N_s) plus the number of catalytic bodies. The quantities $\alpha_{i,r}$ and $\beta_{i,r}$ are the stoichiometric coefficients for reactants and products, respectively, whereas $k_{f,r}^*$ and $k_{b,r}^*$ are the forward and backward rate constants. The quantities X_i^* denote the concentrations in moles per volume. The catalytic bodies ($N_j - N_s$) may be chemical species or linear combinations of species that do not undergo a chemical change during the reaction. The rate of change of any species as a result of a particular reaction (ref. 24) is

$$\left(\frac{dX_i^*}{dt^*}\right)_r = \left(\beta_{i,r} - \alpha_{i,r}\right)\left(k_{f,r}^* \prod_{j=1}^{N_j} X_j^{*\,\alpha_{j,r}} - k_{b,r}^* \prod_{j=1}^{N_j} X_j^{*\,\beta_{j,r}}\right) \tag{47}$$

Equation (47) may be rewritten as

$$(\dot{w}_i^*)_r = M_i^*\left(\beta_{i,r} - \alpha_{i,r}\right)\left(k_{f,r}^* \prod_{j=1}^{N_j} (\gamma_j^* \rho^*)^{\alpha_{j,r}} - k_{b,r}^* \prod_{j=1}^{N_j} (\gamma_j^* \rho^*)^{\beta_{j,r}}\right) \tag{48}$$

where the mole-mass ratio γ_j^* is defined as

$$\gamma_j^* = \left\{\begin{array}{ll} \dfrac{X_j^*}{\rho^*} = \dfrac{C_j}{M_j^*} & (j = 1, 2, \ldots, N_S) \\ \displaystyle\sum_{i=1}^{N_S} Z_{(j-N_S),i}\, \gamma_i^* & (j = N_{S+1}, \ldots, N_j) \end{array}\right\} \tag{49}$$

and

$$\dot{w}_i^* = M_i^* \frac{dX_i^*}{dt^*} = \frac{d\rho_i^*}{dt^*} \tag{50}$$

The constants $Z_{(j-N_S),i}$ are determined from linear dependence of the catalytic bodies upon the N_S species. Values of these constants are given in reference 11 and in table I.

In order to find the net mass rate of production of the ith species per unit volume, equation (48) must be summed over all reactions r. Thus, one obtains

$$\dot{w}_i^* = M_i^* \sum_{r=1}^{N_r} (\beta_{i,r} - \alpha_{i,r}) \left[k_{f,r}^* \prod_{j=1}^{N_j} (\gamma_j^* \rho^*)^{\alpha_{j,r}} - k_{b,r}^* \prod_{j=1}^{N_j} (\gamma_j^* \rho^*)^{\beta_{j,r}}\right] \tag{51}$$

which is the general rate equation for a gas mixture.

The chemical reactions used in the study are as follows:

$$\left.\begin{array}{ll} r = 1 & O_2 + M_1 \rightleftarrows 2O + M_1 \\ r = 2 & N_2 + M_2 \rightleftarrows 2N + M_2 \\ r = 3 & N_2 + N \rightleftarrows 2N + N \\ r = 4 & NO + M_3 \rightleftarrows N + O + M_3 \\ r = 5 & NO + O \rightleftarrows O_2 + N \\ r = 6 & N_2 + O \rightleftarrows NO + N \end{array}\right\} \tag{52}$$

The reaction constants for these equations are expressed in the modified Arrhenius form, where the forward rate is given as

$$k^*_{f,r} = T^{*\,C2^*_r} \exp\left(\log_e C0_r - \frac{C1^*_r \times 10^3}{T^*}\right), \frac{1}{s}\left(\frac{mole}{cm^3}\right)^{-\alpha_r} \tag{53}$$

and the backward rate is given as

$$k^*_{b,r} = T^{*\,D2^*_r} \exp\left(\log_e D0_r - \frac{D1^*_r \times 10^3}{T^*}\right), \frac{1}{s}\left(\frac{mole}{cm^3}\right)^{-\beta_r} \tag{54}$$

where

$$\alpha_r = \sum_{i=1}^{N_j} \alpha_{i,r} - 1 \tag{55}$$

and

$$\beta_r = \sum_{i=1}^{N_j} \beta_{i,r} - 1 \tag{56}$$

Values for the coefficients in equations (53) and (54) are taken from the compilation of experimentally determined rate constants given in reference 25 and are tabulated in table II. Therefore, for a specified temperature, density, and species composition, equations (51) to (54) are used to determine the production rate of a multicomponent gas. The manner in which the production terms are written for numerical solution is discussed in appendix C. (See eqs. (C17) and (C19).)

Method of Solution

The procedure for solving the viscous-shock-layer equations is presented herein. First, the finite-difference expressions used to transform the differential expressions to algebraic expressions are presented. Then the solution procedure is discussed.

Finite-difference expressions.- The derivatives are converted to finite-difference form by using Taylor's series expansions. A variable grid spacing (fig. 3) is used in the η-direction so that the grid spacing can be made small in the region of large gradients. Three-point differences are used in the η-direction, and two-point fully implicit differences are used in the ξ-direction. Truncation terms of order $\Delta \xi_m$ (first order accuracy) and either $\Delta\eta_n \, \Delta\eta_{n-1}$ or $(\Delta\eta - \Delta\eta_{n-1})$ (second order accuracy) are neglected. A typical finite-difference expansion of the standard differential equation (see appendix C, eq. (C8)) gives

$$A_n W_{m,n-1} + B_n W_{m,n} + C_n W_{m,n+1} = D_n \tag{57}$$

The coefficients A, B, C, and D are used to represent the coefficients after the finite-difference expansion of equation (C8). The subscript n denotes the grid points along a line normal to the body surface, whereas the subscript m denotes the grid stations along the body surface. Equations (57) along with the boundary conditions constitute a system of the tridiagonal form, for which efficient computational procedures are available. (See ref. 26.)

Overall solution procedure.- For specified free-stream conditions and body geometry, a stagnation streamline solution is obtained. With the stagnation streamline solution providing the initial conditions, the conditions at the shock providing the outer boundary conditions, and the conditions at the wall taken as the inner boundary conditions, the numerical solution is marched downstream to the desired body location ξ. The first solution pass provides only an approximate flow-field solution, because the following assumptions are used in the first solution pass:

(a) The thin-shock-layer form of the n-momentum equation (eq. (C15b)) is used

(b) The stagnation streamline solution is independent of downstream influence (approximation of local similarity where $n_{2s} = 0$)

(c) The term $dn_s/d\xi$ is equated to zero at each body station

(d) The shock angle α is assumed to be the same as the body angle θ.

These assumptions are then removed by making one or more additional solution passes. For the current study, a total of two solution passes are used since the two passes resulted in a converged flow-field solution. For the second solution pass, the thin-shock-layer form of the normal momentum equation (eq. (C15b) is replaced with equation (C15a).) The $\bar{v}$ component of velocity that is used in equation (C15a) is the average of the first and second pass values. Also, once the first solution pass has been computed, the values of n_{2s} and $dn_s/d\xi$ are calculated and used in the second solution pass to remove approximations b, c, and d. Hence, the viscous-shock-layer equations are solved as parabolic equations, and yet retain effects which are elliptic and hyperbolic in nature. This solution procedure is programed for the Control Data 6600 computer.

Shock solution.- The shock solution procedure at any location is identical for the first and subsequent solution passes. However, the shock angle α is defined differently for the first and subsequent solution passes. The shock angle α is set equal to the local body angle θ for the first solution pass. For subsequent solution passes, the shock angle is defined as

$$\alpha = \theta + \tan^{-1} \frac{n'_s}{1 + \kappa n_s} \tag{58}$$

Figures 4(a) and 4(b) present the solution flow diagrams for equilibrium and frozen shocks, respectively.

Solution procedure at station m.- The viscous-shock-layer equations are solved at any body station m (see fig. 3) in the order shown in figure 5(a) for equilibrium flow and in the order shown in figure 5(b) for either frozen or nonequilibrium flow. The governing equations are uncoupled and the dependent variables are solved one at a time in the order shown in figure 5. First, the shock conditions are calculated to establish the outer boundary conditions. Then the converged profiles at station m - 1 are used as the initial guess for the profiles at station m. The solution is then iterated locally until convergence is achieved. For the stagnation streamline (m = 1), guess values for the profiles are used to start the solution.

Each of the second-order partial differential equations are individually integrated numerically by using the tridiagonal formalism (eq. (57)). The global continuity equation is used to obtain both the shock standoff distance and the $\bar{v}$ components of velocity. By integrating equation (C14) between the limits of $\eta = 0$ and $\eta = 1$ at station m, an implicit equation for n_s is obtained. For the $\bar{v}$ component of velocity at η, equation (C14) is integrated with respect to η between the limits of 0 to η. The pressure $\bar{p}$ is determined at station m by integrating the normal momentum equations (C15) with respect to η between the limits of 1 to η. The equation of state is used to determine the density.

VERIFICATION OF ANALYSIS

In order to assess the overall results obtained for the present analyses, comparisons are made of the results for each of the three chemistry models with data reported in the literature. Table III gives a summary of the viscous-shock-layer and boundary-layer analyses for which comparisons are made with the present analyses.

All computations employed a constant step size of 0.2 in the ξ-direction and a variable step size in the η-direction. A total of 50 grid points is used at each body station m. Also, two solution passes are made in the ξ-direction. The two solution passes provide a converged shock shape and flow-field solution for the problems considered in this study. Table IV summarizes the altitude, velocity, and free-stream properties used. The free-stream properties are those given by the U.S. Standard Atmosphere (see ref. 27).

For each body station, the convergence criterion is that the relative difference between the current and previous iteration values be less than 0.001 for both the temperature and tangential velocity derivatives at the wall. This criterion is used for all calculations except for those where the temperature gradient approaches zero because of mass injection. For this condition, only the velocity derivative is checked. A minimum of three interations is required at each body station.

Frozen Flow Comparisons

The frozen flow calculations are compared with the data of Whitehead (ref. 8). Even though the solution procedure used herein is essentially the same as that used by Whitehead, several differences exist. Whitehead's results account for shock slip at the outer boundary condition and slip and temperature jump at the surface, whereas the present analysis uses the Rankine-Hugoniot relations to describe the shock conditions and assumes no slip or temperature jump at the wall. Furthermore, the expressions used to calculate the thermodynamic and transport properties are not the same as those used by Whitehead.

Figure 6 shows comparisons of the present analysis with that of Whitehead's for shock standoff distance, skin-friction coefficient, and nondimensional heat-transfer rate when the chemistry is frozen at the free-stream composition. The heat-transfer results (fig. 6(c)) are in excellent agreement; however, the agreement is not as good for shock standoff distances (fig. 6(a)) or skin-friction coefficients (fig. 6(b)). Table V presents a detailed listing of the shock and wall values that result from the present calculation.

Equilibrium Flow Comparisons

The equilibrium results are compared with the results obtained from six previous studies. Figure 7 compares the present results with those obtained by Whitehead (ref. 8). The Lewis number for comparison purposes is assumed to be one. Whitehead's equilibrium analysis assumes air to be one "effective" species with a constant molecular weight equal to the free-stream value, whereas the present analysis treats air as a multicomponent mixture of five species. The present calculation predicts greater values for shock standoff distance (fig. 7(a)) (as would be expected because of Whitehead's assumption concerning the molecular weight), skin-friction coefficient (fig. 7(b)), and heat transfer (fig. 7(c)). Table VI(a) presents a detailed listing of the stagnation shock and wall values for the present calculation.

Results of the equilibrium air calculations are also compared with the stagnation results of Edelman and Hoffman. (See ref. 15.) Comparisons of stagnation temperature and species concentration profiles are presented in figure 8. Figures 8(a) and 8(b) show a comparison of the temperature and species profiles, respectively. Table VI(b) presents a detailed listing of the stagnation shock and wall values for the present calculation. Figures 8(c) and 8(d) show the same comparisons for a different set of flow conditions. Table VI(c) presents the stagnation shock and wall values for the present calculation.

When the results of the two calculations for both sets of conditions are compared, two differences are apparent: first, the shape of the temperature profiles, and second, the shock-layer thickness. The curvature of the temperature profiles as calculated by reference 15 decreases monotonically with increasing distance from the surface. Temperature profiles resulting from the present equilibrium calculations are not smooth, especially at the higher altitude (lower pressure) conditions. However, it is believed that the temperature profiles resulting from the present calculations can be substantiated by considering the chemical reactions that occur within the shock layer. A more detailed discussion of this assessment is given in the next section.

The differences in shock-layer thickness are expected since the results presented in reference 15 were for the stagnation streamline only and did not account for the downstream influence on shock standoff distance. When the downstream influence on shock shape is accounted for as in the present analysis, a larger shock-layer thickness results. This effect was shown in reference 6 for an ideal gas.

Figure 9 shows comparisons of the present equilibrium analysis with the stagnation viscous-shock-layer analysis of Goldberg and Scala (ref. 16). Comparisons of static enthalpy, normal velocity, and tangential velocity are presented. The calculations are for a shock Reynolds number of 100. With the exception of shock standoff distance, the results of the two analyses are in good agreement, particularly near the wall where each of the three profiles are in excellent agreement. Table VI(d) gives the shock and wall conditions for the calculation.

As a final comparison of the equilibrium calculations, the viscous-shock-layer results are compared with boundary-layer solutions of Anderson and Lewis, Blottner, and Smith as presented in reference 28. The calculations are for flow over a 10° half-angle hyperboloid. A detailed listing of stagnation shock and wall conditions are given in table VI(e).

The pressure distribution for the boundary-layer calculations was obtained from modified Newtonian theory. This distribution is in excellent agreement with the pressure distribution calculated with the viscous-shock-layer analysis. Therefore, comparison of the two pressure distributions is not presented.

Figure 10 shows comparisons of skin-friction distributions. The three boundary-layer solutions and the viscous-shock-layer solution are in good agreement. The agreement for Stanton number distributions is even better, and therefore, comparisons are not presented.

The aforementioned comparisons of the present equilibrium viscous shock-layer solutions with previous shock-layer and boundary-layer solutions have generally shown good agreement. Where apparent differences exist, such as shock standoff distance, the differences can be rationalized. Note that the comparisons encompass a wide range of flow conditions with shock Reynolds numbers ranging from 100 to 17 931.

Nonequilibrium Comparisons

Results of the nonequilibrium calculations are compared with the stagnation viscous-shock-layer results of Blottner. (See ref. 11.) Comparisons are made of temperature, tangential velocity, and species concentration profiles.

For the chemical kinetics model, Blottner considered two additional species (NO^{+} and e^{-}) and one additional reaction equation ($N + O \rightleftarrows NO^{+} + e^{-}$); however, for the remaining reactions, identical rate expressions are used. The calculations are for an equilibrium catalytic wall. Both analyses use the Rankine-Hugoniot relations to describe the shock conditions and use the no-slip or temperature jump conditions at the wall. Also, for purposes of comparison, the present calculation is made with a constant Lewis number of 1.4.

For two reasons, differences in shock-layer thickness are expected. First, the results of reference 11 do not account for the downstream influence of the stagnation shock standoff distance as does the present analysis. When the downstream effect is neglected, a significant underprediction of stagnation shock standoff distance can occur. (See refs. 6 and 29.) Second, the analysis of reference 11 did not include the effect of shock-layer thickness on the shock radius of curvature as did the present analysis.

Kaiser and Flügge-Lotz (ref. 29, p. 91) found that when the shock-layer thickness contribution to the radius of curvature is neglected, an underprediction of the stagnation shock standoff distance occurs.

Table VII presents a detailed listing of stagnation shock and wall conditions for the present calculation (a constant Lewis number of 1.4). Figures 11(a) and 11(b) show comparisons of temperature and velocity ratio profiles, respectively. The difference in shock standoff distance is readily apparent. These results also show that the temperature and velocity ratio profiles are in good agreement near the wall.

Figure 11(c) shows a comparison of the species concentration profiles for the two analyses. Appreciable differences exist. These differences are due primarily to differences in shock standoff distance. The shock standoff distance for the present analysis is approximately 22 percent greater than that of reference 11. Consequently, a larger distance is available for reactions to occur – in particular, the dissociation reactions. This situation is evident in figure 11(c) which shows that for a given value of n, the amount of dissociated species predicted by the present calculation is greater than that predicted by reference 11.

Significance of Comparisons

The comparisons of the present solutions with previously reported solutions (table III) for frozen, equilibrium, and nonequilibrium flows show generally good agreement. Yet none of the analyses in table III are as detailed as the present analyses. Therefore, for problems similar to those that have been discussed, the more approximate solutions will provide good accuracy. However, this conclusion will not be true for many flow conditions. For example, the importance of including multicomponent diffusion becomes more significant when the species molecular weight disparity becomes greater than that of the neutral air species. (See ref. 4.) Furthermore, it is important to note that the present analyses are more general than those listed in table III. The present analyses provide stagnation and downstream solutions, account for multicomponent diffusion, account for mass injection, and provide solutions where the flow-field chemical species are not limited to the neutral air species.

RESULTS AND DISCUSSION

Numerical solutions to the viscous-shock-layer equations are presented and discussed herein. The solutions are those for flow about a hyperboloid (total included angle of 45°) at an angle of attack of 0°. Results are presented which demonstrate the effects of chemistry model, diffusion model, surface catalycity, and mass injection on flow parameters and surface transport.

All computations are made with the numerical step-size values and convergence criteria that were presented in the previous section. Also, all the subsequent results will be for a free-stream velocity of 6.10 km/s, an altitude of 60.96 km in the earth's atmosphere, a 2.54-cm nose radius, and a surface temperature of 1500 K. These flow conditions are representative of those experienced by slender vehicles and the leading edges of manned entry vehicles when entering the atmosphere from a low earth orbit. Note, however, that the analyses are not restricted to the slender bodies considered in the present study.

Chemistry Models

In this section results of calculations using frozen, equilibrium, and nonequilibrium chemistry are presented. Multicomponent diffusion, no mass injection, and a noncatalytic wall are assumed. First, velocity, temperature, and species concentration profiles are presented for each chemistry model. Next, the equilibrium temperature profiles are shown and their dependence on chemical reactions and pressure variations are discussed. Then the effect of each chemistry model on tangential velocity, temperature, and chemical species profiles, heat transfer, Stanton number, skin friction, shock standoff distance, and wall pressure is shown.

Figures 12 to 15 show the velocity, temperature, and species profiles at various body stations for each chemistry model. There are several features of these profiles that are of interest. The tangential velocity profiles (figs. 12(a) to 12(c)) are practically linear in the outer region of the shock layer; that is, the flow has an outer region of essentially uniform vorticity. This result is in marked contrast to the classical velocity boundary-layer profile that is derived with a zero velocity gradient imposed at the outer boundary. The flow considered here is in the viscous-layer regime (ref. 30) where the viscous effects extend over an appreciable fraction of the shock layer and thereby invalidate the boundary-layer concept.

The equilibrium temperature profiles are shown in figure 13(b). Near the wall, the equilibrium temperature profiles do not show the monotonically decreasing curvature associated with nonequilibrium (fig. 13(a)) and frozen (fig. 13(c)) profiles. The equilibrium temperature profiles have two distinct inflection points. From the body to the shock, the profiles are characterized by concave, convex, and concave segments.

The bulges appearing in the temperature profiles can be explained in terms of chemical reactions. This effect is demonstrated in figure 16, where stagnation temperature profiles and species concentration profiles are shown. Temperature profiles for an equilibrium chemistry solution and a frozen chemistry solution (where the chemistry is frozen at the equilibrium shock composition) are shown. The temperature profile for the equilibrium calculation is much fuller than the profile for the frozen calculation. This condition should exist, of course, because exothermic reactions occur near the wall. Essentially all chemical reactions occur within that half of the shock layer which is adjacent to the wall; that is, essentially all the atom recombinations occur near the wall. The recombinations also occur over two distinct and separate regions. The oxygen recombines between the wall and $\eta = 0.11$. This condition causes the inner bulge in the temperature profile. Then there is a small region (η of 0.11 to 0.16) where the recombination process is negligible. Finally, practically all the atomic nitrogen recombines between η values of 0.16 and 0.5. This recombination causes the outer bulge in the temperature profile.

The extent to which the equilibrium temperature profiles differ from smooth profiles will depend upon the pressure, and hence the altitude for a given free-stream velocity. This effect is demonstrated by Hansen in figure 1 of reference 31. The data of Hansen show that the recombination reactions occur over narrow temperature intervals at low pressures (0.0001 to 0.1 atm); however, the temperature intervals required for nitrogen and oxygen recombination increase significantly with increasing pressure. Furthermore, the temperature interval between the completion of nitrogen recombination and the onset of oxygen recombination decreases with increasing pressure. Consequently, as the pressure increases, the chemical composition experiences a more gradual change with temperature. The pressures are 0.1 atmosphere or less for the temperature profiles shown in figure 13(b); therefore, recombinations over narrow separated temperature intervals would be expected.

Figure 14 shows the nonequilibrium species profiles at different body stations for a noncatalytic wall. The chemistry across the shock is frozen at the free-stream composition $\left(C_O = 0.24;\ C_{N_2} = 0.76\right)$. The figures show that most of the dissociation occurs in the outermost part of the shock layer. Furthermore, only a small amount of recombination occurs near the wall. This effect is due to the low-density flow conditions which reduce the effectiveness of recombination reactions; consequently, the amount of dissociated flow at the wall is significant (approximately one-fifth of the total mass). This result is important because the energy invested in dissociation is not recovered.

Figure 15 shows the equilibrium concentration profiles at different body stations. It is seen that a large percentage of flow is dissociated in the outer part of the shock layer. The amount of dissociation decreases rapidly downstream. Essentially all the dissociated species recombine in a relatively small region near the wall, with the wall composition being approximately that of the free-stream composition. This statement, of course, means that the energy of dissociation is recovered. The significance of this statement in terms of heat-transfer rate will be discussed.

Comparisons of results using the three chemistry models are shown in figures 17 to 23. The effects on tangential velocity and temperature profiles, shock standoff distance, heat-transfer rate, Stanton number, skin friction, and wall pressure are shown. Note that all these quantities are significantly influenced by the chemistry model with the exception of the tangential velocity profiles (fig. 17) and the wall pressure distribution (fig. 23). Of particular significance are the large differences in shock-layer temperatures for the different chemistry models. Figures 18(a) and 18(b) show the temperature profiles at an ξ of 0.0 and 2.0, respectively, for each chemistry model. The conditions at the shock were identical for the frozen and nonequilibrium calculation since the chemical composition was assumed to be frozen across the shock at the free-stream composition. For the stagnation streamline (fig. 18(a)), the frozen shock temperature is more than twice that of the equilibrium shock temperature. Moreover, the equilibrium temperatures across the shock layer are much less than those of the frozen or nonequilibrium values except in the region near the wall. This condition is due to the large amount of energy invested in dissociation rather than in static temperature. Also, the nonequilibrium temperatures are less than the frozen values because some dissociation occurs within the nonequilibrium shock layer. At the downstream station, $\xi = 2.0$ (fig. 18(b)), the temperature differences are noticeably less than those at the stagnation station because the equilibrium and nonequilibrium compositions are more nearly like the frozen composition at the lower temperatures.

Figure 19 shows how the chemistry model influences shock standoff distance. The shock standoff distances corresponding to the equilibrium calculation are considerably less than those for frozen and nonequilibrium calculations. Also, the shock standoff distances for the nonequilibrium calculations are somewhat less than those for the frozen calculations. These results are expected since the shock-layer densities for the nonequilibrium and especially the equilibrium calculations are greater than the frozen flow densities.

Consider next the effect that the chemistry model has on heat-transfer rate distribution. As is shown in figure 20, the chemistry model has a very pronounced effect on nondimensional heat transfer. Both the frozen and equilibrium chemistry models significantly overpredict the heat transfer to a noncatalytic wall. This condition is especially true in the stagnation region where the frozen and equilibrium values are approximately 50 percent greater than the nonequilibrium values. This fact is particularly significant because the entry corridor for slender entry vehicles includes the altitude-velocity conditions used in the present calculations. Furthermore, the heating rates are significant at these conditions, and therefore, the need for nonequilibrium analyses is clearly evident from these results.

When the heat-transfer rate is expressed in terms of Stanton number (fig. 21), the results for the three chemistry models are in closer agreement than were the nondimensional heat-transfer rates (fig. 20). As was pointed out previously (fig. 14), a significant amount of energy is invested in dissociation at the wall in nonequilibrium flow. Consequently, the enthalpy at the wall is larger for the nonequilibrium and noncatalytic wall calculation and the enthalpy potential is smaller. The maximum difference between the equilibrium and nonequilibrium Stanton numbers is about 13 percent and occurs at the stagnation point.

The effect of the chemistry model on skin-friction distribution is shown in figure 22. This figure shows that the skin-friction distributions for the equilibrium and nonequilibrium calculations are about the same. The values for the frozen calculation are greater than the nonequilibrium values, but the differences never exceed 9 percent.

The effect of the chemistry model on wall pressure distribution is shown in figure 23. Also shown is the Newtonian pressure distribution. The nonequilibrium and frozen pressure distributions are identical. The equilibrium and Newtonian pressure values are in close agreement and are less than the nonequilibrium pressure. At $\xi = 3.0$, the nonequilibrium pressure is 10.8 percent greater than the equilibrium and the Newtonian pressures.

Catalytic Wall Effects

Results presented in the previous section demonstrated how the flow-field chemistry can influence flow parameters and surface transport. This section demonstrates how surface catalysis influences the same flow parameters and surface transport. Either noncatalytic or equilibrium catalytic walls are assumed. For the equilibrium catalytic wall, the gas composition at the wall is the equilibrium composition for the wall temperature and pressure. The elemental composition at the wall is governed by multicomponent diffusion and is, therefore, not necessarily equal to the free-stream elemental composition.

Comparison of the noncatalytic and equilibrium catalytic wall calculations is made. The diffusion for both calculations is multicomponent. Table VII provides a detailed listing of the stagnation shock and wall values for the noncatalytic and equilibrium catalytic calculations.

The wall catalytic activity has negligible effect on temperature and velocity profiles, and therefore comparisons are not presented. However, the species profiles for the flow configuration examined are necessarily influenced by the wall catalytic activity. This influence is shown in figures 24(a), 24(b), and 24(c), where comparisons are made at an ξ of 0, 1.0, and 3.0, respectively, of nonequilibrium species profiles with noncatalytic and equilibrium catalytic wall conditions. It is seen that the species profiles for the innermost 70 percent of the shock layer are influenced by the wall catalytic activity.

Figures 25 to 28 show how wall catalytic activity influences shock standoff distance, heat transfer, Stanton number, and skin friction. With the exception of heat transfer, the wall catalytic activity has little effect. The maximum relative differences between the catalytic and noncatalytic calculations are 3.5 percent for shock standoff distance, 4.9 percent for skin friction, and 9.2 percent for Stanton number. The maximum relative difference in heat transfer is 48 percent.

For purposes of comparison, figure 26 also includes the heat-transfer distribution for equilibrium flow. It is seen that the results for nonequilibrium flow with an equilibrium catalytic wall and the results for equilibrium flow are in close agreement. For both of these calculations, the energy invested in dissociation is recovered. However, the results for nonequilibrium flow with a noncatalytic wall show an appreciable amount of dissociation at the wall (see fig. 14), and, hence, the wall heat transfer is substantially reduced.

Diffusion Models

Prior to this study, stagnation and downstream viscous-shock-layer results that treated the diffusion as multicomponent were not available. In this section, comparisons are shown between multicomponent and binary diffusion models. The effects on flow parameters and surface transport are presented for both equilibrium and nonequilibrium air.

One of the binary approximations is that all species have the same diffusion coefficient that is equal to the coefficient for molecular nitrogen diffusing into atomic oxygen. This approach is logical because atomic oxygen and molecular nitrogen are the dominant species in the shock layer. (See figs. 14 and 15.) The multicomponent diffusion coefficients are determined according to equation (B15). Note that this approach for evaluating the binary diffusion coefficient results in a variable Lewis number.

No mass injection and a noncatalytic wall are assumed. With the exception of the species profiles, essentially no effect of diffusion model is observed. Even the effect on species profiles is small as is shown in figures 29 and 30.

Figures 29(a) and 29(b) show comparisons of binary and multicomponent species profiles for equilibrium air at an ξ of 0.0 and 1.0, respectively. More molecular oxygen and less molecular nitrogen are present at the wall for multicomponent diffusion.

The elemental composition is not a constant for multicomponent diffusion as is the case for binary diffusion. However, the departure from elemental invariance is small for the equilibrium air calculation. The elemental composition at the wall is $\tilde{C}_O = 0.278$ and $\tilde{C}_N = 0.722$ at $\xi = 0.0$, and $\tilde{C}_O = 0.279$ and $\tilde{C}_N = 0.721$ at $\xi = 1.0$, as opposed to the free-stream values of $\tilde{C}_O = 0.24$ and $\tilde{C}_N = 0.76$.

Figures 30(a) and 30(b) show comparisons of species profiles for multicomponent and binary diffusion models at ξ values of 0 and 1.0, respectively. The flow is nonequilibrium air. Once again the diffusion model has a small effect on species profiles. The elemental wall concentrations are $\tilde{C}_O = 0.221$ and $\tilde{C}_N = 0.778$ at $\xi = 0$, and $\tilde{C}_O = 0.222$ and $\tilde{C}_N = 0.779$ at $\xi = 1.0$.

The other flow parameters and surface transport values are essentially the same for both diffusion models, and therefore comparisons of results are not presented. For example, the differences in stagnation heat-transfer rates, between binary and multicomponent values, were 0.74 percent for nonequilibrium flow and -0.84 percent for equilibrium flow.

The question of whether a variable binary Lewis number, as previously described, provides better results than a constant Lewis number is now considered. For air, the most frequently used values of Lewis number are 1.0 and 1.4. Calculations are made for both equilibrium and nonequilibrium air (noncatalytic wall) with constant Lewis numbers of 1.0 and 1.4. For the equilibrium calculations, a Lewis number of 1.0 underpredicts and a Lewis number of 1.4 overpredicts the heat-transfer rate. The differences in stagnation heat-transfer rates were 10.3 percent for a Lewis number of 1.4 and -5.5 percent for a Lewis number of 1.0. For the nonequilibrium calculations, the effects of diffusion model on heating rates were negligible since the errors were less than 0.8 percent. Therefore, these results show that the diffusion model has a small effect on most flow-field properties and surface-transport values. However, differences as large as 10 percent can be incurred for equilibrium heat-transfer rates when a constant Lewis number of 1.0 or 1.4 is used in lieu of multicomponent diffusion. Also, the differences introduced by using a binary diffusion approximation can be significantly reduced by using a variable Lewis number where the diffusion coefficient is based on the two dominant species.

Mass Injection

In this section, the results of computations with mass injection are considered. In all cases the mass injection rate distribution is given by equation (28). Figure 31 shows the injection distribution for different values of the nondimensional stagnation injection parameter $\dot{m}_0$. It is seen that the injection rate approaches zero at a ξ of about 1.5.

Figures 32 to 39 and table VIII show how injecting equilibrium air into nonequilibrium air influences flow parameters and surface transport. Multicomponent diffusion and a noncatalytic wall are assumed. Stagnation mass injection rates as large as 0.4 are considered.

Figure 32 shows comparisons of species profiles for no injection and an injection rate of 0.2. These comparisons are made at a ξ of 0, 1.0, and 3.0. At the stagnation point, the shock-layer chemical composition is altered substantially because of mass injection (fig. 32(a)). At the wall, the mass of dissociated flow is 6 percent for a 0.2 injection rate and 24 percent for no injection. Downstream the effect of mass injection on chemical composition decreases (fig. 32(b)) because the injection rate is smaller (eq. (28)). At $\xi = 3.0$, which is beyond the body station where mass injection is zero, the chemical composition of the two shock layers (fig. 32(c)) is about the same.

Figures 33 and 34 show the stagnation tangential velocity and temperature profiles, respectively. These results qualitatively are as one would expect. That is, the shock-layer thickness increases and the tangential velocity and temperature gradients decrease with increasing mass injection rate.

Figure 35 shows the effect of mass injection on shock standoff distance. For stagnation injection rates of 0.2 or greater, the injectant increases the shock standoff distance as far downstream as the calculations are made ($\xi = 3.0$).

Figure 36 shows the effect of injecting equilibrium air into nonequilibrium air on nondimensional heat-transfer distribution. As the injection rate increases, the heat-transfer rate near the stagnation point approaches zero for an $\dot{m}_0$ of 0.4. Downstream, however, the effect of injection rate on heat-transfer rate decreases rapidly. Figure 37 shows that the same conclusions apply to Stanton number distributions.

Figure 38 shows the effect of mass injection on skin-friction coefficient distributions. In the mass-injection region, large reductions in skin friction occur. Downstream, however, the skin-friction values with injection are approaching the no-injection values. For example, for a stagnation mass-injection rate of 0.4, the skin friction at $\xi = 0.4$ is 90 percent less than the no-injection value, but at $\xi = 3.0$ the reduction is only 9 percent.

The effect of mass injection on wall pressure distribution is shown in figure 39. An almost negligible effect is obtained. The wall pressure is less with mass injection but the pressure differences never exceed 4 percent for the mass-injection rates considered. This result is due primarily to the way that the injected mass alters the shock shape and, consequently, the shock pressure. This condition is evident in figure 35, where the shock slope decreases with increasing injection rate. Hence, the local shock angle α (fig. 1) is less and so is the shock pressure. Obviously, the way mass injection alters the shock shape and shock pressure will depend on the assumed mass injection distribution.

For some hypersonic flow conditions, in particular, hypervelocity planetary entries where radiant heating is very large, the mass-injection rates can be large enough to insure that the convective heating is reduced to zero. Calculations were made to demonstrate the present ability to calculate the effect of mass injection on stagnation heat transfer and shock shape at such injection rates. Figures 40 to 42 show such an effect for the injection of equilibrium air into reacting equilibrium air. Figure 40 shows the manner in which the stagnation wall heat-transfer rate decreases with increasing mass injection and becomes zero at a mass-injection rate of about 0.4. Figure 41 shows the influence of injection on stagnation shock standoff distance. For the range of injection rates shown, the shock standoff distance increases linearly with increasing injection rate. Figure 42 shows the effect of even larger injection rates on shock standoff distance. (The results for injection rates greater than 0.4 did not consider the downstream influence on the stagnation solution.) For injection rates greater than 0.4, the shock standoff distance continues to increase with increasing injection rate but the slope of the curve decreases.

CONCLUSIONS

Equations describing reacting and nonreacting viscous shock layers about an axisymmetric body at an angle of attack of 0° are presented. These equations account for mass injection and multicomponent diffusion. An implicit finite-difference technique for solving these equations is discussed. Comparisons of the present results with previously reported solutions are made for a range of flow conditions that include shock Reynolds numbers $\left(\rho_{\infty}^{*}u_{\infty}^{*}a^{*}/\mu_{s}^{*}\right)$ of 100 to 17 931. Calculated results are described which show the effect of chemistry model, surface catalysis, diffusion model, and mass injection on flow parameters and surface transport. Some of the solutions provide information previously unavailable for reacting air. For example, the downstream viscous-shock-layer solutions that treat the diffusion as multicomponent, with or without injection of air, were previously unavailable. These results were obtained for both nonequilibrium and equilibrium flow over slender bodies.

Results of the study lead to the following conclusions:

1. The chemistry model substantially influences flow parameters and surface transport. Results show that the frozen and equilibrium chemistry models overpredict wall heat-transfer rates for the flow conditions considered in this study. For example, the stagnation heating rate obtained with an equilibrium calculation is 54 percent greater than comparable results with a nonequilibrium and noncatalytic wall calculation.

2. Wall catalysis significantly influences wall heat-transfer rate and species composition near the wall but has little influence on the other flow parameters considered. For an equilibrium catalytic wall, the wall heat-transfer rate for nonequilibrium flow is shown to be about the same as that for equilibrium flow.

3. For reacting air, results for multicomponent and binary diffusion models were compared. The binary approximations included both constant Lewis numbers (1.0 and 1.4) and a variable Lewis number, where the diffusion coefficient was the diffusion coefficient for atomic oxygen diffusing into molecular nitrogen. Results show negligible differences in most flow parameters and surface transport when binary diffusion is used in lieu of multicomponent diffusion. The largest effect of diffusion model is on heat-transfer rate and species distributions. When constant Lewis numbers of 1.0 and 1.4 are used, the heat transfer is within 10 percent of the results with multicomponent diffusion. When a variable Lewis number is used, the differences are negligible. This result applies to both nonequilibrium and equilibrium air. For multicomponent diffusion a small amount of elemental diffusional separation is observed, and consequently, a small difference in species profiles occurs.

4. Mass injection significantly alters all flow parameters and surface transport. The effect that mass injection has on the flow field downstream of the injection region

decreases very rapidly with downstream distance. The solutions with mass injection clearly demonstrate the capability of the present analysis to study problems with distributed massive blowing.

Langley Research Center,
National Aeronautics and Space Administration,
Hampton, Va., August 7, 1973.

APPENDIX A

FACTORS USED TO NONDIMENSIONALIZE THE VISCOUS-SHOCK-LAYER EQUATIONS

The viscous-shock-layer equations are nondimensionalized by using the following relations:

$$\left.\begin{array}{ll}
u^* = uU_\infty^* & h^* = hU_\infty^{*2} \\[2ex]
v^* = vU_\infty^* & \dot{w}_i^* = \dfrac{\dot{w}_i \rho_\infty^* U_\infty^*}{a^*} \\[2ex]
T^* = \dfrac{TU_\infty^{*2}}{C_{p,\infty}^*} & J_i^* = \dfrac{J_i \mu_{ref}^*}{a^*} \\[2ex]
p^* = p\,\rho_\infty^* U_\infty^{*2} & s^* = sa^* \\[2ex]
\rho^* = \rho\,\rho_\infty^* & n^* = na^* \\[2ex]
\mu^* = \mu\mu_{ref}^* & \kappa^* = \kappa a^* \\[2ex]
K^* = K\mu_{ref}^* C_{p,\infty}^* & r^* = ra^* \\[2ex]
C_p^* = C_p C_{p,\infty}^* &
\end{array}\right\} \qquad (A1)$$

where

$$\mu_{ref}^* = \mu^* \left(\frac{U_\infty^{*2}}{C_{p,\infty}^*} \right)$$

Also, four dimensionless parameters appear in the shock-layer equations. They are

$$N_{Pr} = \frac{C_p^* \mu^*}{K^*} \qquad (A2)$$

$$\epsilon = \sqrt{\frac{\mu_{ref}^{*}}{\rho_{\infty}^{*} U_{\infty}^{*} a^{*}}} \tag{A3}$$

$$\zeta_{ij} = \frac{\rho^{*} C_{p}^{*} \mathcal{D}_{ij}^{*}}{K^{*}} \tag{A4}$$

$$N_{Le,ij} = \frac{\rho^{*} C_{p}^{*} D_{ij}^{*}}{K^{*}} \tag{A5}$$

APPENDIX B

THERMODYNAMIC AND TRANSPORT PROPERTIES

Thermodynamic properties, $C_{p,i}^{*}$ and h_i^{*}, and transport properties, μ_i^{*}, K_i^{*}, and $\mathcal{D}_{ij}^{*}$, are required for each species considered. For equilibrium calculations, the free energies F_i^{*} are also required. Since the multicomponent gas mixtures are considered to be mixtures of thermally perfect gases, the thermodynamic and transport properties for each species are calculated by using the local static temperature.

Then the properties for the gas mixtures are determined in terms of the individual species properties.

Thermodynamic Properties

Values for the thermodynamic properties as a function of temperature are obtained by using polynomial curve fits for each chemical species. The following polynomial equations are used:

Specific heat:

$$\frac{C_{p,i}^{*}}{R^{*}} = a_1 + a_2 T^{*} + a_3 T^{*2} + a_4 T^{*3} + a_5 T^{*4} \tag{B1}$$

Enthalpy:

$$\frac{h_i^{*}}{R^{*}T^{*}} = a_1 + \frac{a_2 T^{*}}{2} + \frac{a_3 T^{*2}}{3} + \frac{a_4 T^{*3}}{4} + \frac{a_5 T^{*4}}{5} + \frac{a_6}{T^{*}} \tag{B2}$$

and

Free energy:

$$\frac{F_i^{*o}}{R^{*}T^{*}} = a_1 (1 - \log_e T^{*}) - \frac{a_2 T^{*}}{2} - \frac{a_3 T^{*2}}{6} - \frac{a_4 T^{*3}}{12} - \frac{a_5 T^{*4}}{20} + \frac{a_6 - a_7}{T^{*}} \tag{B3}$$

where F_i^{*o} is the free energy of species i at 1 atmosphere pressure (standard state). The development of these curve fits and a tabulation of the polynomial constants (a_1 to a_7) are presented in reference 32. For the species used in this study, the constants are given in table IX.

Transport Properties

The gas mixtures considered are assumed to be mixtures of thermally perfect gases. The expressions used for calculating the transport properties of the pure species will be presented first, and are followed by the expressions used for calculating the transport properties of the mixture.

To a first approximation (first-order kinetic theory), the viscosity for a perfect gas (ref. 33) is given as

$$\mu_i^* = \frac{2.6693 \times 10^{-5} \sqrt{T^* M_i^*}}{\sigma_i^{*2} \, \Omega_{ij}^{*(2,2)}} \tag{B4}$$

and the thermal conductivity for a monatomic gas is given as

$$K_{i,mon}^* = \frac{1.9891 \times 10^{-4} \sqrt{T^*/M_i^*}}{\sigma_i^2 \Omega_{ij}^{*(2,2)}} \tag{B5}$$

or

$$K_{i,mon}^* = \frac{15}{4} \frac{\mu_i^*}{M_i^*} R^* \tag{B6}$$

The thermal conductivity for a polyatomic gas has an additional contribution due to the transfer of energy between translational and internal degrees of freedom. Consequently, the expression for the thermal conductivity of polyatomic molecules is given (ref. 34) as

$$K_i^* = \frac{R^*}{M_i^*} \mu_i^* \left[\frac{15}{4} + 1.32 \left(\frac{C_{p,i}^*}{R^*} - \frac{5}{2}\right)\right] \tag{B7}$$

In the foregoing equations

T^*	temperature, K
M_i^*	molecular weight, g/mole

σ_i^*	collision diameter, Å
μ_i^*	viscosity, g/cm-sec
K_i^*	thermal conductivity, cal/sec-K
$\Omega_{ij}^{*(2,2)}$	collision integral for viscosity

The derivations of equations (B4) and (B5) are based on a very simple gas model (ref. 34); that is, a nonreacting mixture of monatomic gases at relatively low temperatures. However, equations (B4) and (B7) have been found to be reasonably accurate for temperatures that are less than that required for ionization. Figures 43 and 44 show the viscosity and thermal conductivity values, respectively, for each chemical species.

Expressions for the multicomponent viscosity and thermal conductivity according to rigorous kinetic theory are given in reference 33. However, these expressions are cumbersome and computationally time consuming. Consequently, most studies use approximate techniques for evaluating the mixture viscosity and thermal conductivity.

The mixture viscosity is obtained by using the semiempirical formula of Wilke (from ref. 20)

$$\mu^* = \sum_{i=1}^{N_s} \left\{ \frac{x_i \mu_i^*}{\sum_{j=1}^{N_s} x_j \phi_{ij}} \right\} \tag{B8}$$

where

$$\phi_{ij} = \frac{\left[1 + \left(\frac{\mu_i^*}{\mu_j^*}\right)^{1/2} \left(\frac{M_j^*}{M_i^*}\right)^{1/4}\right]^2}{\sqrt{8}\left(1 + \frac{M_i^*}{M_j^*}\right)^{1/2}} \tag{B9}$$

Figure 45 shows the mixture viscosity of equilibrium air as a function of temperature and for a pressure of 1.0 atmosphere (1 atmosphere = 101.3 kN/m^2). Also shown is the viscosity as predicted by Sutherland's equation. Note that the values of viscosity used in this study are greater than those predicted by Sutherland's equation. For most of the calculations made in this study, the wall temperature is 1500 K. At this temperature, the viscosity predicted by the Sutherland equation is 7 percent less than the value used herein.

The mixture thermal conductivity is obtained by a method analogous to that used for viscosity. The relation used (ref. 20) for calculating the mixture conductivity is

$$K^* = \sum_{i=1}^{N_s} \frac{x_i K_i^*}{\sum_{j=1}^{N_s} x_j \phi_{ij}} \tag{B10}$$

where the ϕ_{ij} coefficients are identical with those that appear in the viscosity equation.

Values for the equilibrium air mixture thermal conductivity as a function of temperature and for a pressure of 1 atmosphere are given in figure 46. These values are also compared with the mixture conductivity obtained by assuming a constant Prandtl number equal to 0.72, Sutherland's value of viscosity, and the specific heat as given by equations (13) and (B1). The resulting values of conductivity are less (10 percent less at 1500 K) than the conductivity values used herein.

The binary diffusion coefficients are obtained by using the relation given in reference 33

$$\mathcal{D}_{ij}^* = \frac{(2.628 \times 10^{-3}) T^{*3/2} \sqrt{\dfrac{M_i^* + M_j^*}{2M_i^* M_j^*}}}{P^* \sigma_{ij}^{*2} \Omega_{ij}^{*(1,1)}} \tag{B11}$$

where $\Omega_{ij}^{*(1,1)}$ is the collision integral for diffusion. The collision integrals $\Omega_{ij}^{*(1,1)}$ and $\Omega_{ij}^{*(2,2)}$ are functions of the nondimensional reduced temperature

$$T^+ = \frac{T^*}{\epsilon_{ij}^*/k^*} \tag{B12}$$

where ϵ_{ij}^* is the maximum energy of attraction between colliding molecules and k^* is Boltzmann's constant. The parameters σ_{ij}^* and ϵ_{ij}^* are estimated satisfactorily by

$$\sigma_{ij}^* = \frac{1}{2}\left(\sigma_i^* + \sigma_j^*\right) \tag{B13}$$

and

$$\epsilon_{ij}^* = \sqrt{\epsilon_i^* \epsilon_j^*} \tag{B14}$$

The force constants σ_i^* and ϵ_i^*/k^* for each species considered in this study are given in table X. The force constants are those given in reference 34. The collision integrals were obtained from reference 33 (pp. 1126-1127) where they are tabulated as a function of reduced temperature T^+. These collision integrals are based on the Lennard Jones 6-12 potential for the interaction of colliding molecules.

For the binary diffusion calculations, the diffusion is approximated by two methods. One method assumes that all species have diffusion coefficients equal to an effective binary coefficient. The effective binary coefficients are determined for a preassigned diffusing pair of species. For example, the effective binary diffusion coefficient for air will be that of atomic oxygen diffusing into molecular nitrogen evaluated at the local temperature and pressure according to equation (B11). The second binary diffusion approximation is that the Lewis number is some constant value. Both approximations are used in this study.

The multicomponent diffusion coefficients are dependent on the concentration of the species. These coefficients are obtained by using the relations given in reference 1, which may be written as

$$D_{ij}^* = \overline{\overline{K}}_{ij}^* - \frac{M_i^*}{M_j^*}\overline{\overline{K}}_{ii}^* \tag{B15}$$

where the quantities $\overline{\overline{K}}_{ij}^*$ are coefficients in the matrix which is the inverse of the matrix with the following coefficients:

$$K_{ij}^* = \left\{\begin{matrix} \dfrac{C_i}{\mathcal{D}_{ij}^*} + M_j^* \displaystyle\sum_{\substack{\ell=1 \\ \ell\neq 1}}^{N_S} \frac{C_\ell}{M_\ell^* \mathcal{D}_{i\ell}^*} & (i \neq j) \\ 0 & (i = j) \end{matrix}\right\} \tag{B16}$$

APPENDIX C

TRANSFORMED VISCOUS-SHOCK-LAYER EQUATIONS

This appendix presents the transformed viscous-shock-layer equations and boundary conditions. First, the relations defining the transformed variables and coordinates are given. Next, the general equations and boundary conditions are given. Then the special form of the equations for the stagnation streamline are developed along with the stagnation shock relations.

Transformation Relations

To simplify the numerical computations, a transformation is applied to the viscous-shock-layer equations. This transformation is accomplished by normalizing most of the variables with their local shock values. When the normal coordinate is normalized with respect to the local shock standoff distance, a constant number of finite-difference grid points between the body and shock are used. This procedure eliminates the need for interpolating to determine shock shape and the addition of grid points in the normal direction as the computation moves downstream.

The transformed variables are

$$\left.\begin{array}{lll}
\eta = \dfrac{n}{n_s} & \bar{p} = \dfrac{p}{p_s} & \bar{\mu} = \dfrac{\mu}{\mu_s} \\[2ex]
\xi = s & \bar{\rho} = \dfrac{\rho}{\rho_s} & \bar{K} = \dfrac{K}{K_s} \\[2ex]
\bar{u} = \dfrac{u}{u_s} & \bar{T} = \dfrac{T}{T_s} & \bar{C}_p = \dfrac{C_p}{C_{p,s}} \\[2ex]
\bar{v} = \dfrac{v}{v_s} & \bar{H} = \dfrac{H}{H_s} &
\end{array}\right\} \tag{C1}$$

The transformations relating the differential quantities are

$$\frac{\partial}{\partial s} = \frac{\partial}{\partial \xi} - \frac{n_s'}{n_s} \eta \frac{\partial}{\partial \eta} \tag{C2}$$

where

$$n_s' = \frac{dn_s}{d\xi} \tag{C3}$$

$$\frac{\partial}{\partial n} = \frac{1}{n_s} \frac{\partial}{\partial \eta} \tag{C4}$$

and

$$\frac{\partial^2}{\partial n^2} = \frac{1}{n_s^2} \frac{\partial^2}{\partial \eta^2} \tag{C5}$$

The transformations used to express the shock-oriented velocities u_s'' and v_s'' in terms of the body-oriented coordinate system (fig. 1) are

$$u_s = u_s'' \sin (\alpha + \beta) + v_s'' \cos (\alpha + \beta) \tag{C6}$$

and

$$v_s = -u_s'' \cos (\alpha + \beta) + v_s'' \sin (\alpha + \beta) \tag{C7}$$

Transformed Equations

After the governing equations are written in transformed variables and coordinates, the second-order partial differential equations are written in the following form:

$$\frac{\partial^2 W}{\partial \eta^2} + \alpha_1 \frac{\partial W}{\partial \eta} + \alpha_2 W + \alpha_3 + \alpha_4 \frac{\partial W}{\partial \xi} = 0 \tag{C8}$$

The quantity W represents $\bar{u}$ in the s-momentum equation, $\bar{T}$ in the temperature energy equation, $\bar{H}$ in the enthalpy energy equation, C_i in the species continuity equations, and $\tilde{C}_\ell$ in the elemental continuity equation. The coefficients α_1 to α_4 are written as follows:

s-momentum, $W = \bar{u}$:

$$a_1 = \frac{1}{\bar{\mu}} \frac{\partial \bar{\mu}}{\partial \eta} + \frac{n_s \kappa}{1 + n_s \eta \kappa} + \frac{j n_s \cos \theta}{r + n_s \eta \cos \theta}$$

$$+ \frac{n_s \rho_s u_s n_s'}{\epsilon^2 \mu_s (1 + n_s \eta \kappa)} \frac{\bar{\rho} \bar{u} \eta}{\bar{\mu}} - \frac{n_s \rho_s v_s}{\epsilon^2 \mu_s} \frac{\bar{\rho} \bar{v}}{\bar{\mu}} \tag{C9a}$$

$$a_2 = - \frac{\kappa n_s}{(1 + n_s \eta \kappa)} \frac{1}{\bar{\mu}} \frac{\partial \bar{\mu}}{\partial \eta} - \frac{\kappa^2 n_s^2}{(1 + n_s \eta \kappa)^2} - \frac{j \cos \theta \, n_s^2 \kappa}{(r + n_s \eta \cos \theta)(1 + n_s \eta \kappa)}$$

$$- \frac{\rho_s n_s^2 u_s'}{\epsilon^2 \mu_s (1 + n_s \eta \kappa)} \frac{\bar{u} \bar{\rho}}{\bar{\mu}} - \frac{n_s^2 \rho_s v_s \kappa}{\epsilon^2 \mu_s (1 + n_s \eta \kappa)} \frac{\bar{\rho} \bar{v}}{\bar{\mu}} \tag{C9b}$$

$$a_3 = - \frac{p_s n_s^2}{\epsilon^2 \mu_s u_s (1 + n_s \eta \kappa) \bar{\mu}} \left(\frac{\partial \bar{p}}{\partial \xi} + \frac{p_s' \bar{p}}{p_s} - \frac{n_s' \eta}{n_s} \frac{\partial \bar{p}}{\partial \eta} \right) \tag{C9c}$$

$$a_4 = - \frac{\rho_s u_s n_s^2}{\epsilon^2 \mu_s (1 + n_s \eta \kappa)} \frac{\bar{\rho} \bar{u}}{\bar{\mu}} \tag{C9d}$$

Energy (temperature), $W = \bar{T}$:

$$a_1 = \frac{1}{\bar{K}} \frac{\partial \bar{K}}{\partial \eta} + n_s \left(\frac{\kappa}{1 + n_s \eta \kappa} + \frac{j \cos \theta}{r + n_s \eta \cos \theta} \right) - \frac{n_s \sum_{i=1}^{N_s} J_i C_{p,i}}{K_s \bar{K}}$$

$$- \frac{n_s \rho_s C_{p,s} \bar{\rho} \bar{C}_p}{\epsilon^2 K_s \bar{K}} \left(v_s \bar{v} - \frac{u_s n_s' \bar{u} \eta}{1 + n_s \eta \kappa} \right) \tag{C10a}$$

$$a_2 = \frac{a_4 T'_s}{T_s} - \frac{n_s^2 \dot{w}_{s2}}{\epsilon^2 K_s} \frac{\bar{\dot{w}}_2}{\bar{K}} \tag{C10b}$$

$$a_3 = - \frac{n_s^2 \dot{w}_{s1}}{\epsilon^2 T_s K_s} \frac{\bar{\dot{w}}_1}{\bar{K}} + \frac{n_s^2 \mu_s \bar{\mu}}{T_s K_s \bar{K}_s} \left(\frac{u_s}{n_s} \frac{\partial \bar{u}}{\partial \eta} - \frac{\kappa u_s \bar{u}}{1 + n_s \eta \kappa} \right)^2$$

$$+ \frac{n_s^2 u_s p_s \bar{u}}{\epsilon^2 T_s K_s \bar{K} (1 + n_s \eta \kappa)} \left(\frac{p'_s \bar{p}}{p_s} - \frac{\partial \bar{p}}{\partial \xi} - \frac{n'_s \eta}{n_s} \frac{\partial \bar{p}}{\partial \eta} \right)$$

$$+ \frac{n_s v_s p_s}{\epsilon^2 T_s K_s \bar{K}} \bar{v} \frac{\partial \bar{p}}{\partial \eta} \tag{C10c}$$

$$a_4 = - \frac{n_s^2 p_s C_{p,s} u_s}{\epsilon^2 K_s (1 + n_s \eta \kappa)} \frac{\bar{\rho} \bar{C}_p \bar{u}}{\bar{K}} \tag{C10d}$$

Energy (enthalpy), $W = \bar{H}$:

$$a_1 = \frac{1}{\bar{\mu}} \frac{\partial \bar{\mu}}{\partial \eta} - \frac{1}{\bar{N}_{Pr}} \frac{\partial \bar{N}_{Pr}}{\partial \eta} + n_s \left(\frac{\kappa}{1 + n_s \eta \kappa} + \frac{j \cos \theta}{r + n_s \eta \cos \theta} \right)$$

$$+ \frac{\rho_s N_{Pr,s} \bar{N}_{Pr} n_s}{\epsilon^2 \mu_s \bar{\mu}} \left(\frac{n'_s u_s \eta \bar{u} \bar{\rho}}{1 + n_s \eta \kappa} - v_s \bar{\rho} \bar{v} \right) \tag{C11a}$$

$$a_2 = \frac{a_4 H'_s}{H_s} \tag{C11b}$$

$$a_3 = \frac{N_{Pr,s}\bar{N}_{Pr}n_s^2}{\mu_s\bar{\mu}H_s}\left[\frac{1}{n_s}\frac{\partial\psi}{\partial\eta} + \left(\frac{\kappa}{1 + n_s\eta\kappa} + \frac{j\cos\theta}{r + n_s\eta\cos\theta}\right)\psi\right] \tag{C11c}$$

$$a_4 = -\frac{N_{Pr,s}n_s^2\rho_s u_s\bar{N}_{Pr}\bar{u}\bar{\rho}}{\epsilon^2\mu_s(1 + n_s\eta\kappa)\bar{\mu}} \tag{C11d}$$

where

$$\psi = \frac{\mu_s}{n_sN_{Pr,s}}\left[-\frac{\bar{\mu}}{\bar{N}_{Pr}}\sum_{i=1}^{N_s}h_i\frac{\partial C_i}{\partial\eta} + \frac{u_s^2\bar{\mu}\bar{u}}{\bar{N}_{Pr}}\left(N_{Pr,s}\bar{N}_{Pr} - 1\right)\frac{\partial\bar{u}}{\partial\eta}\right]$$

$$-\sum_{i=1}^{N_s}h_iJ_i - \frac{\mu_su_s^2\kappa\bar{\mu}\bar{u}^2}{1 + n_s\eta\kappa} \tag{C11e}$$

The preceding energy equation is for the thin shock-layer approximation. When equation (3) is used for the n-momentum equation, the following term must be added to (eq. (C11c))

$$-\frac{N_{Pr,s}v_sn_s^2\rho_s}{\epsilon^2\mu_sH_s}\frac{\bar{N}_{Pr}\bar{\rho}\bar{v}}{\bar{\mu}}\left[\frac{u_s\bar{u}}{1 + n_s\eta\kappa}\left(\bar{v}v_s' + v_s\frac{\partial\bar{v}}{\partial\xi} - \frac{n_s'\eta v_s}{n_s}\frac{\partial\bar{v}}{\partial\eta}\right) + \frac{v_s^2\bar{v}}{n_s}\frac{\partial\bar{v}}{\partial\eta}\right] \tag{C11f}$$

Species continuity, $W = C_i$:

$$a_1 = \frac{1}{PL_i}\frac{\partial PL_i}{\partial\eta} + n_s\left(\frac{\kappa}{1 + n_s\eta\kappa} + \frac{j\cos\theta}{r + n_s\eta\cos\theta}\right)$$

$$-\frac{\rho_sv_sn_s\bar{\rho}\bar{v}}{\epsilon^2PL_i} + \frac{n_s\rho_su_sn_s'\bar{\rho}\bar{u}\eta}{\epsilon^2PL_i(1 + n_s\eta\kappa)} \tag{C12a}$$

$$\alpha_2 = -\frac{n_s^2 \dot{w}_i^1}{\epsilon^2 PL_i} \qquad (C12b)$$

$$\alpha_3 = \frac{1}{PL_i}\left[\frac{\partial PM_i}{\partial \eta} + n_s PM_i \left(\frac{\kappa}{1 + n_s \eta\kappa} + \frac{j \cos\theta}{r + n_s \eta \cos\theta}\right) + \frac{\dot{w}_i^o n_s^2}{\epsilon^2}\right] \qquad (C12c)$$

$$\alpha_4 = -\frac{n_s^2 \rho_s u_s \bar{\rho}\bar{u}}{\epsilon^2 PL_i (1 + n_s \eta\kappa)} \qquad (C12d)$$

where

$$PL_i = \frac{\mu_s \bar{\mu} N_{Le,i}}{N_{Pr,s} \bar{N}_{Pr}} \qquad (C12e)$$

and

$$PM_i = \frac{\mu_s \bar{\mu}}{N_{Pr,s} \bar{N}_{Pr}} \sum_{\substack{k=1 \\ k\neq i}}^{N_s} \Delta b_{ik} \frac{\partial C_k}{\partial \eta} \qquad (C12f)$$

for multicomponent diffusion and

$$PL_i = PL = \frac{\mu_s \bar{\mu} \zeta}{N_{Pr,s} \bar{N}_{Pr}} \qquad (C12g)$$

and

$$PM_i = PM = 0 \qquad (C12h)$$

for binary diffusion.

Elemental continuity, $W = \tilde{C}_\ell$:

$$a_1 = \frac{1}{\tilde{PL}} \frac{\partial \tilde{PL}}{\partial \eta} + n_s \left(\frac{\kappa}{1 + n_s \eta \kappa} + \frac{j \cos \theta}{r + n_s \eta \cos \theta} \right)$$

$$- \frac{\rho_s v_s n_s \bar{\rho} \bar{v}}{\epsilon^2 \tilde{PL}} + \frac{n_s \rho_s u_s n'_s \bar{\rho} \bar{u} \eta}{\epsilon^2 \tilde{PL}(1 + n_s \eta \kappa)} \tag{C13a}$$

$$a_2 = 0 \tag{C13b}$$

$$a_3 = \frac{1}{\tilde{PL}} \left[\frac{\partial}{\partial \eta} \tilde{PM}_\ell + n_s \tilde{PM}_\ell \left(\frac{\kappa}{1 + n_s \eta \kappa} + \frac{j \cos \theta}{r + n_s \eta \cos \theta} \right) \right] \tag{C13c}$$

$$a_4 = - \frac{n_s^2 \rho_s u_s}{\epsilon^2 (1 + n_s \eta \kappa)} \frac{\bar{\rho} \bar{u}}{\tilde{PL}} \tag{C13d}$$

where

$$\tilde{PL} = \frac{\mu_s \bar{\mu} N_{Le,i}}{N_{Pr,s} \bar{N}_{Pr}} \tag{C13e}$$

and

$$\tilde{PM}_\ell = \sum_{i=1}^{N_s} \delta_{i\ell} \frac{M_\ell^*}{M_i^*} \sum_{\substack{k=1 \\ k \neq i}}^{N_s} \Delta b_{ik} \frac{\partial C_k}{\partial \eta} \tag{C13f}$$

for multicomponent diffusion and

$$\tilde{PL} = \frac{\mu_s \bar{\mu} \zeta}{N_{Pr,s} \bar{N}_{Pr}} \tag{C13g}$$

$$\tilde{PM}_\ell = \tilde{PM} = 0 \tag{C13h}$$

for binary diffusion.

The remaining equations are written as follows:

Global continuity:

$$\frac{\partial}{\partial \xi}\left[n_s(r+n_s\eta\cos\theta)^j\rho_s u_s\bar{\rho}\bar{u}\right]+\frac{\partial}{\partial\eta}\left\{(r+n_s\eta\cos\theta)^j\left[(1+n_s\eta\kappa)\rho_s v_s\bar{\rho}\bar{v}\right.\right.$$

$$\left.\left.-\;n_s'\eta\rho_s u_s\bar{\rho}\bar{u}\right]\right\}=0 \tag{C14}$$

n-momentum:

$$\frac{\bar{\rho}\bar{u}}{1+n_s\eta\kappa}\left(\frac{v_s'}{v_s}\bar{v}+\frac{\partial\bar{v}}{\partial\xi}-\frac{n_s'\eta}{n_s}\frac{\partial v}{\partial\eta}\right)+\frac{v_s}{u_s}\frac{\bar{\rho}\bar{v}}{n_s}\frac{\partial\bar{v}}{\partial\eta}$$

$$-\frac{u_s}{v_s}\frac{\kappa}{1+n_s\eta\kappa}\bar{\rho}\bar{u}^2+\frac{p_s}{\rho_s u_s n_s v_s}\frac{\partial\bar{p}}{\partial\eta}=0 \tag{C15a}$$

which becomes

$$\frac{\partial\bar{p}}{\partial\eta}=\frac{n_s\rho_s u_s^2\kappa}{p_s(1+n_s\eta\kappa)}\bar{\rho}\bar{u}^2 \tag{C15b}$$

if the thin-shock layer approximation is made, and

State:

$$\bar{p}=\bar{\rho}\bar{T}\frac{M^*}{M_s^*} \tag{C16}$$

The terms $\dot{w}_1$ and $\dot{w}_2$ which appear in the temperature form of the energy equation and the terms w_i^0 and w_i^1 which appear in the species continuity equations are quantities that involve the rate of production terms, $\dot{w}_i$. As discussed in references 1, 7, and 11, the way the production terms are written is very important in achieving convergence of the iteration procedure. Consequently, for the energy equation, the production terms are written as (see ref. 7)

$$\left(\frac{\dot{w}_i}{\rho}\right)_{k+1} = \left(\frac{\dot{w}_i}{\rho}\right)_k + \left(\frac{\partial}{\partial T} \frac{\dot{w}_i}{\rho}\right)_k \left(T_{k+1} - T_k\right) \tag{C17}$$

where k denotes the iteration for which the solution is known and k + 1 the iteration for which a solution is required. The term $\sum_{i=1}^{N_s} h_i \dot{w}_i$ which appears in equation (4) is written as follows:

$$\sum_{i=1}^{N_s} h_i \dot{w}_i = \dot{w}_{s1} \bar{\dot{w}}_1 + T_s w_{s2} \overline{T\dot{w}}_2 \tag{C18}$$

and appears in equations (C10b) and (C10c). As for the species continuity equations, the production term is written as

$$\frac{\dot{w}_i}{\rho} = \dot{w}_i^o - C_i \dot{w}_i^1 \tag{C19}$$

and appears in equations (C12b) and (C12c). Hence, equations (C17) and (C19) express the production terms in terms of temperature for the energy equation and in terms of species mass fraction for the species equations. Blottner in reference 1 comments on the necessity of using expressions like equations (C17) and (C19).

For frozen, equilibrium, and nonequilibrium chemistry, equations (C8) to (C16), along with the appropriate boundary conditions and relations for the thermodynamic and transport properties, are the governing relations used to describe the viscous shock layer.

Boundary Conditions

Conditions at the body surface.- The surface boundary conditions in terms of transformed variables are

$$\bar{u} = 0 \tag{C20}$$

$$\bar{v} = \frac{\dot{m}}{\bar{\rho}\rho_s v_s} \tag{C21}$$

where

$$\dot{m} = (\rho v)_- \tag{C22}$$

$$\bar{T} = \text{Constant} \tag{C23}$$

$$\bar{H} = \frac{\left(\sum_{i=1}^{N_s} h_i C_i\right)_w}{\left(\sum_{i=1}^{N_s} h_i C_i\right)_s} \tag{C24}$$

$$(C_i - C_{i-})\,\dot{m} = -\epsilon^2 J_i \tag{C25}$$

$$(\tilde{C}_\ell - \tilde{C}_{\ell-})\,\dot{m} = -\epsilon^2 \tilde{J}_\ell \tag{C26}$$

The surface species boundary conditions (eq. (C25)) are written as

$$\frac{\partial C_i}{\partial \eta} + \beta_1 C_i + \beta_{2,i} = 0 \tag{C27}$$

where the coefficients β_1 and $\beta_{2,i}$ are defined as

$$\beta_1 = -\frac{\rho_s v_s \dot{m} n_s N_{Pr,s} \bar{N}_{Pr}}{\epsilon^2 N_{Le,i}\, \mu_s \bar{\mu}} \tag{C28}$$

$$\beta_{2,i} = -\beta_1 C_{i-} + \frac{1}{N_{Le,i}} \sum_{\substack{k=1\\k\neq i}}^{N_s} \Delta b_{ik} \frac{\partial C_k}{\partial \eta} \tag{C29}$$

for multicomponent diffusion and

$$\beta_1 = -\frac{\rho_s v_s \dot{m} n_s N_{Pr,s} \bar{N}_{Pr}}{\epsilon^2 \mu_s \bar{\mu} \zeta} \tag{C30}$$

$$\beta_{2,i} = -\beta_1 C_{i-} \tag{C31}$$

for binary diffusion.

The elemental boundary conditions (eq. (B26)) are written as

$$\frac{\partial \tilde{C}_\ell}{\partial \eta} + \tilde{\beta}_1 \tilde{C}_\ell + \tilde{\beta}_{2,\ell} = 0 \tag{C32}$$

where the coefficients $\tilde{\beta}_1$ and $\tilde{\beta}_{2,\ell}$ are defined as

$$\tilde{\beta}_1 = -\frac{\rho_s v_s \dot{m} n_s N_{Pr,s} \bar{N}_{Pr}}{\epsilon^2 \mu_s \bar{\mu} L} \tag{C33}$$

$$\tilde{\beta}_{2,\ell} = -\tilde{\beta}_1 \tilde{C}_{\ell -} + n_s^2 L \sum_{i=1}^{N_s} \frac{\delta_{i\ell} M_\ell^*}{M_i^*} \sum_{k=1}^{N_s} \Delta b_{ik} \frac{\partial C_k}{\partial \eta} \tag{C34}$$

for multicomponent diffusion and

$$\tilde{\beta}_1 = -\frac{\rho_s v_s \dot{m} n_s}{\epsilon^2 \mu_s \bar{\mu} \zeta} N_{Pr,s} \bar{N}_{Pr} \tag{C35}$$

$$\tilde{\beta}_{2,\ell} = -\tilde{\beta}_1 \tilde{C}_{\ell-} \tag{C36}$$

for binary diffusion. When the diffusion is binary and the injectant has the same composition as the free stream, the elemental concentrations are constant and equal to the free-stream value. For this case, the elemental equations are superfluous and the surface conditions become

$$\tilde{C}_{\ell,w} = \tilde{C}_{\ell,\infty} \tag{C37}$$

However, when the diffusion is multicomponent, the elemental distribution along the normal to the surface is not constant and the elemental conservation equations must be used to calculate the elemental distribution.

Conditions at the shock.- The shock conditions are determined by solving equations (35) to (42). The transformed shock conditions become

$$\bar{u} = \bar{T} = \bar{H} = \bar{v} = \bar{\rho} = \bar{p} = 1 \tag{C38}$$

at $\eta = 1$. Note that the elemental species mass fractions are not normalized with their respective shock values.

Stagnation Streamline Equations

When downstream numerical solutions are required, it is necessary to have an accurate solution for the flow along the stagnation streamline. A truncated series, which has the same form as that used by Kao in reference 35, is used to develop the stagnation streamline equations. The flow variables are expanded about the axis of symmetry with respect to the nondimensional distance ξ along the body as follows:

$$p(\xi,\eta) = p_1(\eta) + p_2(\eta)\,\xi^2 + \cdots \tag{C39a}$$

$$u(\xi,\eta) = u_1(\eta)\xi + \cdots \tag{C39b}$$

$$v(\xi,\eta) = v_1(\eta) + \cdots \tag{C39c}$$

$$\rho(\xi,\eta) = \rho_1(\eta) + \cdots \tag{C39d}$$

$$T(\xi,\eta) = T_1(\eta) + \cdots \qquad \text{(C39e)}$$

$$h(\xi,\eta) = h_1(\eta) + \cdots \qquad \text{(C39f)}$$

$$\mu(\xi,\eta) = \mu_1(\eta) + \cdots \qquad \text{(C39g)}$$

$$K(\xi,\eta) = K_1(\eta) + \cdots \qquad \text{(C39h)}$$

$$C_p(\xi,\eta) = C_{p,1}(\eta) + \cdots \qquad \text{(C39i)}$$

$$\tilde{C}_\ell(\xi,\eta) = \tilde{C}_{\ell,1}(\eta) + \cdots \qquad \text{(C39j)}$$

$$C_i(\xi,\eta) = C_{i,1}(\eta) + \cdots \qquad \text{(C39k)}$$

The shock standoff distance is written as

$$n_s = n_{1s} + n_{2s}\xi^2 + \cdots \qquad \text{(C40)}$$

Furthermore, ξ is small and the curvature κ is approximately one in the stagnation region. Consequently, the geometric relations (see fig. 1), including terms of order ξ, can be written as

$$\beta \approx \xi \qquad \text{(C41)}$$

and

$$\alpha \approx \frac{\Pi}{2} + \xi\left(\frac{2n_{2s}}{1 + n_{1s}} - 1\right) \qquad \text{(C42)}$$

Therefore,

$$\sin(\alpha + \beta) \approx 1 \qquad \text{(C43)}$$

and

$$\cos(\alpha + \beta) \approx \frac{2n_{2s}\xi}{1 + n_{1s}} \tag{C44}$$

The shock relations (eqs. (35) to (42)) in terms of expanded variables become

$$v_s = v_{1s} + \cdot\cdot\cdot \approx -\frac{1}{\rho_{1s}} \tag{C45}$$

$$u_s = u_{1s}\xi + \cdot\cdot\cdot \approx \xi\left[1 - \frac{2n_{2s}}{1 + n_{1s}}\left(1 - \frac{1}{\rho_{1s}}\right)\right] \tag{C46}$$

$$p_s = p_{1s} + p_{2s}\xi^2 + \cdot\cdot\cdot \approx \frac{1}{\gamma M_\infty^2} + \left(1 - \frac{1}{\rho_{1s}}\right)$$

$$- \xi^2\left[\left(1 - \frac{1}{\rho_{1s}}\right)\left(1 - \frac{2n_{2s}}{1 + n_{1s}}\right)^2\right] \tag{C47}$$

and

$$h_s = h_{1s} + \cdot\cdot\cdot \approx \frac{1}{M_\infty^2(\gamma_\infty - 1)} + \frac{1}{2}\left(1 - \frac{1}{\rho_{1s}}\right) \tag{C48}$$

Equations (40) to (42) are unchanged.

By examining these equations, it is seen that the equations for u_s and p_s contain n_{2s}. This term cannot be determined from the stagnation solutions since it is a function of the downstream flow. Consequently, a value must be assumed for n_{2s}. In this study, it was assumed to be zero to start the solution, but this assumption is then removed by iterating on the solution by using the previous shock standoff distances to define n_{2s}. The effect of the downstream shock shape on the stagnation-point solution is elliptic rather than parabolic.

Along the stagnation streamline, the second-order differential equations are written as

$$\frac{d^2w}{d\eta^2} + a_1 \frac{dw}{d} + a_2 w + a_3 = 0 \tag{C49}$$

The coefficients are defined as

s-momentum; W = $\bar{u}$:

$$a_1 = \frac{1}{\bar{\mu}_1} \frac{d\bar{\mu}_1}{d\eta} + (j+1) \frac{n_{1s}}{1 + n_{1s}\eta} - \frac{n_{1s}\rho_{1s}v_{1s}}{\epsilon^2 \mu_{1s}} \frac{\bar{\rho}_1 \bar{v}_1}{\bar{\mu}_1} \tag{C50a}$$

$$a_2 = -\frac{n_{1s}}{1 + n_{1s}\eta} \left[\frac{1}{\bar{\mu}_1} \frac{d\bar{\mu}_1}{d\eta} + \frac{n_{1s}}{1 + n_{1s}\eta} (j+1) + \frac{\rho_{1s} n_{1s} u_{1s}}{\epsilon^2 \mu_{1s}} \frac{\bar{\mu}_1 \bar{\rho}_1}{\bar{\mu}_1} \right.$$

$$\left. + \frac{n_{1s}\rho_{1s}v_{1s}}{\epsilon^2 \mu_{1s}} \frac{\bar{\rho}_1 \bar{v}_1}{\bar{\mu}_1} \right] \tag{C50b}$$

$$a_3 = \frac{-2p_{1s} n_{1s}^2}{\epsilon^2 \mu_{1s} (1 + n_{1s}\eta) u_{1s} \bar{\mu}} \left[\bar{p}_2 + \frac{p_{2s}\bar{p}_1}{p_{1s}} - \frac{n_{1s}\eta}{n_{1s}} \frac{d\bar{p}_1}{d\eta} \right] \tag{C50c}$$

Energy (temperature); W = $\bar{T}$:

$$a_1 = \frac{1}{K_1} \frac{d\bar{K}_1}{d\eta} + (j+1) \frac{n_{1s}}{1 + n_{1s}\eta} - \frac{n_{1s}}{K_{1s}\bar{K}_1} \sum_{i=1}^{N_s} J_{i,1} C_{p,i,1}$$

$$- \frac{n_{1s}\rho_{1s} C_{p,1s} v_s}{\epsilon^2 K_{1s}} \frac{\bar{\rho}_1 \bar{C}_{p,1} \bar{v}_1}{\bar{K}_1} \tag{C51a}$$

$$a_2 = -\frac{n_{1s}^2 \dot{w}_{s2} \bar{\dot{w}}_2}{\epsilon^2 K_{1s} \bar{K}_1} \tag{C51b}$$

$$a_3 = \frac{n_{1s} v_{1s} p_{1s} \bar{v}_1}{\epsilon^2 T_{1s} K_{1s} \bar{K}_1} \frac{d\bar{p}_1}{d\eta} - \frac{n_{1s}^2 \dot{w}_{s1}}{\epsilon^2 T_{1s} K_{1s} \bar{K}_1} \bar{\dot{w}}_1 \tag{C51c}$$

Energy (enthalpy); $W = \bar{H}$:

$$a_1 = \frac{1}{\bar{\mu}_1} \frac{d\bar{\mu}_1}{d\eta} - \frac{1}{N_{Pr,1}} \frac{d\bar{N}_{Pr,1}}{d\eta} + \frac{(j+1)n_{1s}}{1+n_{1s}\eta} - \frac{n_{1s} \rho_{1s} N_{Pr,1s} v_{1s}}{\epsilon^2 \mu_{1s}} \frac{\bar{\rho}_1 \bar{N}_{Pr,1} \bar{v}_1}{\bar{\mu}_1} \tag{C52a}$$

$$a_2 = 0 \tag{C52b}$$

$$a_3 = \frac{N_{Pr,1s} n_{1s}^2}{\mu_{1s} H_{1s}} \frac{\bar{N}_{Pr,1}}{\bar{\mu}_1} \left[\frac{1}{n_{1s}} \frac{d\psi}{d\eta} + \frac{(j+1)\psi}{1+\eta n_{1s}} \right] \tag{C52c}$$

Species continuity; $W = C_i$:

$$a_1 = \frac{1}{PL_i} \frac{dPL_i}{d\eta} + (j+1) \frac{n_{1s}}{1+\eta n_{1s}} - \frac{\rho_{1s} v_{1s} n_{1s} \bar{\rho}_1 \bar{v}_1}{\epsilon^2 PL_i} \tag{C53a}$$

$$a_2 = -\frac{n_{1s}^2 \dot{w}_i^1}{\epsilon^2 PL_i} \tag{C53b}$$

$$a_3 = \frac{1}{PL_i} \left[\frac{dPM_i}{d\eta} + (j+1) \frac{PM_i n_{1s}}{1+\eta n_{1s}} + \frac{\dot{w}_i^o n_{1s}^2}{\epsilon^2} \right] \tag{C53c}$$

Elemental continuity; $W = \widetilde{C}_\ell$:

$$\alpha_1 = \frac{1}{\widetilde{PL}} \frac{d\widetilde{PL}}{d\eta} + (j + 1) \frac{n_{1s}}{1 + \eta\, n_{1s}} - \frac{n_{1s}\, \rho_{1s} v_{1s}\, \bar{\rho}_1 \bar{v}_1}{\epsilon^2 \widetilde{PL}} \tag{C54a}$$

$$\alpha_2 = 0 \tag{C54b}$$

$$\alpha_3 = \frac{1}{\widetilde{PL}} \left[\frac{d\widetilde{PM}_\ell}{d\eta} + (j + 1) \frac{n_{1s}\, \widetilde{PM}_\ell}{1 + \eta\, n_{1s}} \right] \tag{C54c}$$

The remaining equations are written as follows:

Global continuity:

$$\frac{d}{d\eta} \left[(1 + n_{1s}\, \eta)^{j+1}\, \rho_{1s} v_{1s}\, \bar{\rho}_1 \bar{v}_1 \right]$$

$$= -(j + 1) n_{1s} (1 + n_{1s} \eta)^j\, \rho_{1s} u_{1s}\, \bar{\rho}_1 \bar{u}_1 \tag{C55}$$

n-momentum:

$$\frac{d\bar{p}_1}{d\eta} = - \frac{v_{1s}^2\, \rho_{1s}}{\bar{p}_{1s}}\, \bar{\rho}_1 \bar{v}_1 \frac{d\bar{v}_1}{d\eta} \tag{C56a}$$

When the thin shock-layer approximation is made, the n-momentum equation becomes

$$\frac{d\bar{p}_1}{d\eta} = 0 \tag{C56b}$$

The $\bar{p}_2$ term that appears in equation (C50c) can be expressed as

$$\frac{d\bar{p}_2}{d\eta} = \frac{\rho_{1s} u_{1s}^2 n_{1s}}{p_{1s}} \frac{\bar{\rho}_1 \bar{u}_1^2}{1 + \eta n_{1s}} + \frac{2 \rho_{1s} u_{1s} n_{2s} v_{1s}}{p_{1s}} \frac{\bar{\rho}_1 \bar{u}_1 \eta}{1 + \eta n_{1s}} \frac{d\bar{v}_1}{d\eta}$$

$$+ \frac{p_{2s} \rho_{1s} v_{1s}^2}{p_{1s}^2} \bar{\rho}_1 \bar{v}_1 \frac{d\bar{v}_1}{d\eta} \qquad \text{(C56c)}$$

and for the thin-shock-layer approximation as

$$\frac{d\bar{p}_2}{d\eta} = \frac{\rho_{1s} u_{1,s}^2 n_{1s}}{p_{1s}} \frac{\bar{\rho}_1 \bar{u}_1^2}{1 + \eta n_{1s}} \qquad \text{(C56d)}$$

These equations along with the equation of state constitute the nonlinear ordinary differential equations that are solved along the stagnation streamline.

REFERENCES

1. Blottner, F. G.: Finite Difference Methods of Solution of the Boundary-Layer Equations. AIAA J., vol. 8, no. 2, Feb. 1970, pp. 193-205.
2. Blottner, F. G.: Nonequilibrium Laminar Boundary-Layer Flow of Ionized Air. AIAA J., vol. 2, no. 11, Nov. 1964, pp. 1921-1927.
3. Moore, Jeffrey Annin: Chemical Non-Equilibrium in Viscous Flows. Ph. D. Diss., State Univ. of New York at Buffalo, 1967.
4. Nachtsheim, Philip R.: Multicomponent Diffusion in Chemically Reacting Laminar Boundary Layers. 1967 Heat Transfer and Fluid Mechanics Institute, Stanford Univ. Press, June 1967, pp. 58-87.
5. Davy, William C.; Craig, Roger A.; and Lyle, Gilbert C.: An Evaluation of Approximations Used in the Analysis of Chemically Reacting, Stagnation-Point Boundary Layers With Wall Injection. Proceedings of the 1970 Heat Transfer and Fluid Mechanics Institute, Turgut Sarphaya, ed., Stanford Univ. Press, 1970, pp. 222-237.
6. Davis, R. T.: Numerical Solution of the Hypersonic Viscous Shock-Layer Equations. AIAA J., vol. 8, no. 5, May 1970, pp. 843-851.
7. Davis, R. T.: Hypersonic Flow of a Chemically Reacting Binary Mixture Past a Blunt Body. AIAA Paper No. 70-805, June-July 1970.
8. Whitehead, Robert Earl: Numerical Solutions to the Viscous Shock-Layer Blunt-Body Problem With Inert Gas Injection. Ph. D. Thesis, Virginia Polytechnic Institute and State University, 1971.
9. Dellinger, Thomas C.: Nonequilibrium Air Ionization in Hypersonic Fully Viscous Shock Layers. AIAA Paper No. 70-806, June-July 1970.
10. Moss, James Norvel: Solutions for Reacting and Nonreacting Viscous Shock Layers With Multicomponent Diffusion and Mass Injection. Ph. D. Thesis, Virginia Polytechnic Institute and State University, 1972.
11. Blottner, F. G.: Viscous Shock Layer at the Stagnation Point With Nonequilibrium Air Chemistry. AIAA J., vol. 7, no. 12, Dec. 1969, pp. 2281-2288.
12. Adams, J. C.; Lewis, C. H.; Brahinsky, H. S.; and Marchand, E. O.: Effects of Chemical Nonequilibrium, Mass Transfer, and Viscous Interaction on Spherically Blunted Cones at Hypersonic Conditions. AIAA Paper No. 69-168, Jan. 1969.
13. Adams, John C., Jr.: Shock Slip Analysis of Merged Layer Stagnation Point Air Ionization. AIAA J., vol. 8, no. 5, May 1970, pp. 971-973.

14. Lee, Richard H. C.; and Zierten, Thomas A.: Merged Layer Ionization in the Stagnation Region of a Blunt Body. Proceedings of the 1967 Heat Transfer and Fluid Mechanics Institute, Paul A. Libby, Daniel B. Olfe, and Charles W. Van Atta, eds., Stanford Univ. Press, c.1967, pp. 452-468.

15. Edelman, R.; and Hoffman, J.: Viscous Hypersonic Flow in the Vicinity of the Stagnation Point of Axisymmetric Blunt Bodies – Calculations and Results for Equilibrium Air. Tech. Rep. No. 498 (Contract SD-149), Gen. Appl. Sci. Lab., Inc., May 10, 1965. (Available from DDC as AD 463 703.)

16. Goldberg, Leon; and Scala; Sinclaire: Mass Transfer in the Hypersonic Low Reynolds Number Viscous Layer. R62SD07 (Contract AF04-(647)-617), Gen. Elec. Co., Jan. 15, 1962.

17. Chen, S. Y.; Baron, J.; and Mobley, R.: Stagnation Region Gas Injection in Low Reynolds Number Hypersonic Flow. 1967 Heat Transfer and Fluid Mechanics Institute, Stanford Univ. Press, June 1967, pp. 34-57.

18. Cheng, H. K.: The Blunt-Body Problem in Hypersonic Flow at Low Reynolds Numbers. Rep. AF-1285-A10 (Contract Nonr 2653(00)), Cornell Aeronaut. Lab., Inc., June 1963.

19. Davis, R. T.; and Flügge-Lotz, I.: Second-Order Boundary-Layer Effects in Hypersonic Flow Past Axisymmetric Blunt Bodies. J. Fluid Mech., vol. 20, pt. 4, Dec. 1964, pp. 593-623.

20. Bird, R. Byron; Stewart, Warren E.; and Lightfoot, Edwin N.: Transport Phenomena. John Wiley & Sons, Inc., c.1960.

21. Williams, Forman A.: Combustion Theory. Addison-Wesley Pub. Co., Inc., c.1965.

22. Zeldovich, Y. B.: On the Theory of Combustion of Initially Unmixed Gases. NACA TM 1296, 1951.

23. Stroud, C. W.; and Brinkley, Kay L.: Chemical Equilibrium of Ablation Materials Including Condensed Species. NASA TN D-5391, 1969.

24. Vincenti, Walter G.; and Kruger, Charles H., Jr.: Introduction to Physical Gas Dynamics. John Wiley & Sons, Inc., c.1965.

25. Bortner, M. H.: Suggested Standard Chemical Kinetics for Flow Field Calculations – A Consensus Opinion. AMRAC Proceedings, vol. XIV, Pt. 1, Doc. No. 4613-135-X (Contract SD-91), Inst. Sci. Technol., Univ. of Michigan, Apr. 18-19, 1966, pp. 569-581. (Available from DDC as AD 372 900.)

26. Conte, S. D.: Elementary Numerical Analysis. McGraw-Hill Book Co., Inc., c.1965.

27. Anon.: U.S. Standard Atmosphere, 1962. NASA, U.S. Air Force, and U.S. Weather Bur., Dec. 1962.

28. Anderson, E. C.; and Lewis, C. H.: Laminar or Turbulent Boundary-Layer Flows of Perfect Gases or Reacting Gas Mixtures in Chemical Equilibrium. NASA CR-1893, 1971.

29. Kaiser, J. E.; and Flügge-Lotz, I.: Viscous, Hypersonic Flow Around a Blunt Body. AFOSR 68-0988, U.S. Air Force, Jan. 1968. (Available from DDC as AD 669 578.)

30. Probstein, Ronald F.: Shock Wave and Flow Field Development in Hypersonic Re-Entry. ARS J., vol. 31, no. 2, Feb. 1961, pp. 185-194.

31. Hansen, C. Frederick: Approximations for the Thermodynamic and Transport Properties of High Temperature Air. NASA TR R-50, 1959. (Supersedes NACA TN 4150.)

32. Esch, D. D.; Siripong, A.; and Pike, R. W.: Thermodynamic Properties in Polynomial Form for Carbon, Hydrogen, Nitrogen, and Oxygen Systems From 300 to 15000°K. NASA-FFL-TR-70-3, Reacting Fluids Lab., Dept. Chem. Eng., Louisiana State Univ., Nov. 15, 1970. (Available as NASA CR-111989.)

33. Hirschfelder, Joseph O.; Curtiss, Charles F.; and Bird, R. Byron: Molecular Theory of Gases and Liquids. John Wiley & Sons, Inc., c.1954.

34. Svehla, Roger A.: Estimated Viscosities and Thermal Conductivities of Gases at High Temperatures. NASA TR R-132, 1962.

35. Kao, Hsiao C.: Hypersonic Viscous Flow Near the Stagnation Streamline of a Blunt Body: I.- A Test of Local Similarity. AIAA J., vol. 2, no. 11, Nov. 1964, pp. 1892-1897.

TABLE I.- THIRD BODY EFFICIENCIES RELATIVE TO ARGON

Catalytic bodies	$Z_{(j-N_s),i}$	Efficiencies relative to argon of –				
		O	O_2	N	N_2	NO
		i = 1	i = 2	i = 3	i = 4	i = 5
M_1	1,i	25	9	1	2	1
M_2	2,i	1	1	0	2.5	1
M_3	3,i	20	1	20	20	20

TABLE II.- REACTION RATE COEFFICIENTS

Reaction, r	$C0_r$, $\frac{1}{s}\left(\frac{\text{mole}}{\text{cm}^3}\right)^{-\alpha_r}$	$C1_r$, K	$C2_r$	$D0_r$, $\frac{1}{s}\left(\frac{\text{mole}}{\text{cm}^3}\right)^{-\beta_r}$	$D1_r$, K	$D2_r$
1	3.61×10^{18}	59.4	-1.0	3.01×10^{15}	0	-0.5
2	1.92×10^{17}	113.1	-.5	1.09×10^{16}	0	-.5
3	4.15×10^{22}	113.1	-1.5	2.32×10^{21}	0	-1.5
4	3.97×10^{20}	75.6	-1.5	1.01×10^{20}	0	-1.5
5	3.18×10^{9}	19.7	1.0	9.63×10^{11}	3.6	.5
6	6.75×10^{13}	37.5	0	1.50×10^{13}	0	0

TABLE III.- ANALYSES FOR WHICH COMPARISONS ARE MADE

Investigator(s)	Analysis	Air chemistry model	Diffusion	Region of application
Whitehead, reference 8	Viscous shock layer	Frozen and equilibrium	Binary	Stagnation and downstream
Edelman and Hoffman, reference 15	Viscous shock layer	Equilibrium	Binary	Stagnation
Goldberg and Scala, reference 16	Viscous shock layer	Equilibrium	Binary	Stagnation
Anderson and Lewis, reference 28	Boundary layer	Equilibrium	Binary	Stagnation
Blottner, as given in reference 28	Boundary layer	Nonequilibrium	Multicomponent	Stagnation and downstream
Smith, as given in reference 28	Boundary layer	Nonequilibrium	Binary	Stagnation and downstream
Blottner, reference 11	Viscous shock layer	Nonequilibrium	Binary	Stagnation

TABLE IV.- FREE-STREAM CONDITIONS

Altitude, km	Velocity, km/s	Temperature, K	Pressure, atm	Density, g/m^3	Mach number	Free-stream Reynolds number (a)
85.34	7.92	180.65	3.82×10^{-6}	7.46×10^{-6}	29.40	1.482×10^{3}
76.20	6.10	195.4	2.01×10^{-5}	3.62×10^{-5}	21.75	5.170×10^{3}
60.96	6.10	253.88	1.95×10^{-4}	2.70×10^{-4}	19.08	3.116×10^{4}
45.72	6.86	266.67	1.28×10^{-3}	1.70×10^{-3}	20.98	2.217×10^{5}
30.48	6.10	266.98	1.09×10^{-2}	1.70×10^{-2}	20.18	2.149×10^{6}

[a] Based on a 0.3048-meter nose radius.

TABLE V.- FROZEN AIR STAGNATION SHOCK AND WALL VALUES

$$\left[\begin{array}{l}\text{Altitude, 60.960 km;}\\ U_\infty^* = 6.096\text{ km/s;}\\ a^* = 2.54\text{ cm;}\\ N_{Re,\infty} = 2.597 \times 10^3;\\ N_{Re,s} = 1.914 \times 10^2\end{array}\right]$$

Properties	Value at shock	Value at wall for –	
		$n_s = 9.079 \times 10^{-2}$; $q^* = 4.865$ MW/m^2	$n_s = 9.215 \times 10^{-2}$; $q^* = 4.796$ MW/m^2
Temperature, K	1.331×10^4	1.000×10^3	1.500×10^3
Pressure, atm	8.822×10^{-2}	9.439×10^{-2}	9.439×10^{-2}
Density, kg/m^3	2.331×10^{-3}	3.317×10^{-2}	2.211×10^{-2}
Viscosity, N-s/m^2	2.197×10^{-4}	4.077×10^{-5}	5.294×10^{-5}
Velocity, km/s	-7.096×10^{-1}	0.0	0.0
Enthalpy, MJ/kg	1.857×10^1	7.630×10^{-1}	1.355×10^0
Molecular weight, g/g-mole . .	2.888×10^1	2.888×10^1	2.888×10^1
Prandtl number	7.018×10^{-1}	6.938×10^{-1}	6.961×10^{-1}
Mass fractions:			
O_2	2.400×10^{-1}	2.400×10^{-1}	2.400×10^{-1}
N_2	7.600×10^{-1}	7.600×10^{-1}	7.600×10^{-1}

TABLE VI.- EQUILIBRIUM AIR STAGNATION SHOCK AND WALL VALUES

(a) Altitude, 60.960 km;
$U_\infty^* = 6.096$ km/s;
$a^* = 2.54$ cm;
$N_{Re,\infty} = 2.597 \times 10^3$;
$N_{Re,s} = 3.376 \times 10^2$

Properties	Value at shock	Value at wall for –			
		Binary		Multicomponent	
		$n_s = 5.681 \times 10^{-2}$; $q^* = 5.028$ MW/m^2; Constant Lewis number = 1.0	$n_s = 5.619 \times 10^{-2}$; $q^* = 5.042$ MW/m^2	$n_s = 5.636 \times 10^{-2}$; $q^* = 5.170$ MW/m^2	$n_s = 5.710 \times 10^{-2}$; $q^* = 5.085$ MW/m^2
Temperature, K	5.783×10^3	1.000×10^3	1.500×10^3	1.000×10^3	1.500×10^3
Pressure, atm	9.293×10^{-2}	9.642×10^{-2}	9.655×10^{-2}	9.644×10^{-2}	9.644×10^{-2}
Density, kg/m^3	3.922×10^{-3}	3.368×10^{-2}	2.272×10^{-2}	3.383×10^{-2}	2.257×10^{-2}
Viscosity, N-s/m^2	1.247×10^{-4}	4.076×10^{-5}	5.285×10^{-5}	4.102×10^{-5}	5.323×10^{-5}
Velocity, km/s	-4.218×10^{-1}	0.0	0.0	0.0	0.0
Enthalpy, MJ/kg	1.857×10^1	7.518×10^{-1}	1.352×10^0	7.509×10^{-1}	1.346×10^0
Molecular weight, g/g-mole . .	1.997×10^1	2.888×10^1	2.888×10^1	2.900×10^1	2.901×10^1
Lewis number	9.044×10^{-1}	1.000×10^0	1.298×10^0	-----------	-----------
Prandtl number	6.754×10^{-1}	6.932×10^{-1}	6.957×10^{-1}	6.922×10^{-1}	6.959×10^{-1}
Mass fractions:					
O	2.381×10^{-1}	1.275×10^{-10}	2.475×10^{-8}	1.260×10^{-10}	1.809×10^{-8}
O_2	5.035×10^{-5}	2.399×10^{-1}	2.392×10^{-1}	2.720×10^{-1}	2.759×10^{-1}
N	2.241×10^{-1}	3.962×10^{-22}	8.112×10^{-14}	3.980×10^{-22}	1.369×10^{-15}
N_2	5.343×10^{-1}	7.600×10^{-1}	7.594×10^{-1}	7.280×10^{-1}	7.227×10^{-1}
NO	3.360×10^{-3}	3.582×10^{-5}	1.344×10^{-3}	3.722×10^{-5}	1.404×10^{-3}

TABLE VI.- EQUILIBRIUM AIR STAGNATION SHOCK AND WALL VALUES – Continued

(b) Altitude, 85.344 km;
$U_\infty^* = 7.925$ km/s;
$a^* = 30.480$ cm;
$N_{Re,\infty} = 1.482 \times 10^3$;
$N_{Re,s} = 1.498 \times 10^2$;
$n_s = 3.801 \times 10^{-2}$;
$q^* = 7.861 \times 10^{-1}$ MW/m^2

Properties	Value at shock	Value at wall
Temperature, K	5.733×10^3	1.349×10^3
Pressure, atm	4.396×10^{-3}	4.528×10^{-3}
Density, kg/m^3	1.485×10^{-4}	1.186×10^{-3}
Viscosity, N-s/m^2	1.203×10^{-4}	4.940×10^{-5}
Velocity, km/s	-3.981×10^{-1}	0.0
Enthalpy, MJ/kg	3.163×10^1	1.176×10^0
Molecular weight, g/g-mole	1.580×10^1	2.888×10^1
Lewis number	1.400×10^0	1.400×10^0
Prandtl number	6.734×10^{-1}	6.957×10^{-1}
Mass fractions:		
O	2.398×10^{-1}	5.331×10^{-8}
O_2	2.098×10^{-6}	2.396×10^{-1}
N	5.927×10^{-1}	5.293×10^{-15}
N_2	1.671×10^{-1}	7.597×10^{-1}
NO	3.776×10^{-4}	6.008×10^{-4}

TABLE VI.- EQUILIBRIUM AIR STAGNATION SHOCK AND WALL VALUES – Continued

(c) Altitude, 45.720 km;
$U_\infty^* = 6.864$ km/s;
$a^* = 1.27$ cm;
$N_{Re,\infty} = 9.236 \times 10^3$;
$N_{Re,s} = 1.134 \times 10^3$;
$n_s = 5.601 \times 10^{-2}$;
$q^* = 2.695 \times 10^1$ MW/m^2

Properties	Value at shock	Value at wall
Temperature, K	6.783×10^3	1.476×10^3
Pressure, atm	7.729×10^{-1}	8.038×10^{-1}
Density, kg/m^3	2.592×10^{-2}	1.916×10^{-1}
Viscosity, N-s/m^2	1.369×10^{-4}	5.237×10^{-5}
Velocity, km/s	-4.715×10^{-1}	0.0
Enthalpy, MJ/kg	2.370×10^1	1.258×10^0
Molecular weight, g/g-mole	1.863×10^1	2.888×10^1
Lewis number	1.400×10^0	1.400×10^0
Prandtl number	6.627×10^{-1}	6.958×10^{-1}
Mass fractions:		
O	2.371×10^{-1}	3.638×10^{-7}
O_2	1.108×10^{-4}	2.397×10^{-1}
N	3.260×10^{-1}	3.983×10^{-15}
N_2	4.310×10^{-1}	7.593×10^{-1}
NO	5.712×10^{-3}	9.205×10^{-4}

TABLE VI.- EQUILIBRIUM AIR STAGNATION SHOCK AND WALL VALUES – Continued

(d) Altitude, 76.20 km;
$U_\infty^* = 6.096$ km/s;
$a^* = 5.532$ cm;
$N_{Re,\infty} = 9.383 \times 10^2$;
$N_{Re,s} = 1.000 \times 10^2$;
$n_s = 5.298 \times 10^{-2}$;
$q^* = 1.475 \times 10^0$ MW/m^2

Properties	Value at shock	Value at wall
Temperature, K	5.291×10^3	1.500×10^3
Pressure, atm	1.245×10^{-2}	1.290×10^{-2}
Density, kg/m^3	5.576×10^{-4}	2.305×10^{-3}
Viscosity, N-s/m^2	1.221×10^{-4}	6.434×10^{-5}
Velocity, km/s	-3.959×10^{-1}	0.0
Enthalpy, MJ/kg	1.863×10^1	1.938×10^0
Molecular weight, g/g-mole	2.885×10^1	1.970×10^1
Lewis number	1.000×10^1	1.000×10^1
Prandtl number	7.019×10^{-1}	6.815×10^{-1}
Mass fractions:		
O	2.393×10^{-1}	1.357×10^{-3}
O_2	9.240×10^{-6}	2.346×10^{-1}
N	2.423×10^{-1}	1.490×10^{-9}
N_2	5.171×10^{-1}	7.565×10^{-1}
NO	1.267×10^{-3}	7.535×10^{-3}

TABLE VI.- EQUILIBRIUM AIR STAGNATION SHOCK AND WALL VALUES – Concluded

(e) Altitude, 30.48 km;
$U_{\infty}^{*} = 6.096$ km/s;
$a^{*} = 2.54$ cm;
$N_{Re,\infty} = 1.791 \times 10^{5}$;
$N_{Re,s} = 1.794 \times 10^{4}$;
$n_{s} = 6.755 \times 10^{-2}$;
$q^{*} = 3.725 \times 10^{1}$ MW/m^2

Properties	Value at shock	Value at wall
Temperature, K	6.967×10^{3}	1.400×10^{3}
Pressure, atm	5.767×10^{0}	6.032×10^{0}
Density, kg/m^3	2.084×10^{-1}	1.516×10^{1}
Viscosity, N-s/m^2	1.475×10^{-4}	5.191×10^{-5}
Velocity, km/s	-4.959×10^{-1}	0.0
Enthalpy, MJ/kg	1.867×10^{1}	1.225×10^{0}
Molecular weight, g/g-mole	2.897×10^{1}	2.076×10^{1}
Lewis number [a]	------------	------------
Prandtl number	6.835×10^{-1}	6.992×10^{-1}
Mass fractions:		
O	2.325×10^{-1}	2.579×10^{-8}
O_2	3.571×10^{-4}	2.670×10^{-1}
N	1.761×10^{-1}	1.105×10^{-29}
N_2	5.777×10^{-1}	7.321×10^{-1}
NO	1.327×10^{-2}	9.093×10^{-4}

[a] Multicomponent diffusion.

TABLE VII.- NONEQUILIBRIUM AIR STAGNATION SHOCK AND WALL VALUES

[Altitude, 60.960 km;
$U_{\infty}^{*} = 6.096$ km/s;
$a^{*} = 2.54$ cm;
$N_{Re,\infty} = 2.597 \times 10^{3}$;
$N_{Re,s} = 1.914 \times 10^{2}$]

Properties	Values at shock	Wall conditions for –			
		Noncatalytic		Catalytic	
		Binary; $n_s = 8.567 \times 10^{-2}$; $q^{*} = 3.208$ MW/m^2	Multicomponent; $n_s = 8.576 \times 10^{-2}$; $q^{*} = 3.281$ MW/m^2	Binary; $n_s = 8.065 \times 10^{-2}$; $q^{*} = 5.141$ MW/m^2	Multicomponent; $n_s = 8.291 \times 10^{-2}$; $q^{*} = 4.864$ MW/m^2
Temperature, K	1.331×10^{4}	1.500×10^{3}	1.500×10^{3}	1.000×10^{3}	1.500×10^{3}
Pressure, atm	8.822×10^{-2}	9.457×10^{-2}	9.457×10^{-2}	9.466×10^{-2}	9.466×10^{-2}
Density, kg/m^3	2.331×10^{-3}	1.786×10^{-2}	1.811×10^{-2}	3.326×10^{-2}	2.217×10^{-2}
Viscosity, N-s/m^2	2.197×10^{-4}	5.246×10^{-5}	5.223×10^{-5}	4.077×10^{-5}	5.294×10^{-5}
Velocity, km/s	-7.096×10^{-1}	0.0	0.0	0.0	0.0
Enthalpy, MJ/kg	1.857×10^{1}	6.009×10^{0}	5.945×10^{0}	7.629×10^{-1}	1.359×10^{0}
Molecular weight, g/g-mole . . .	2.888×10^{1}	2.331×10^{1}	2.360×10^{1}	2.888×10^{1}	2.888×10^{1}
Lewis number	1.338×10^{0}	1.040×10^{0}	-----------	[a] 1.400×10^{0}	------------
Prandtl number	7.018×10^{-1}	6.877×10^{-1}	6.813×10^{-1}	6.938×10^{-1}	6.962×10^{-1}
Mass fractions:					
O	0.0	2.245×10^{-1}	2.052×10^{-1}	1.245×10^{-16}	2.495×10^{-8}
O_2	2.400×10^{-1}	4.875×10^{-3}	2.935×10^{-3}	2.399×10^{-1}	2.389×10^{-1}
N	0.0	2.865×10^{-2}	3.687×10^{-2}	3.453×10^{-31}	8.195×10^{-14}
N_2	7.600×10^{-1}	7.168×10^{-1}	7.298×10^{-1}	7.600×10^{-1}	7.597×10^{-1}
NO	0.0	3.278×10^{-2}	2.320×10^{-2}	3.582×10^{-5}	1.343×10^{-3}

[a] Lewis number was constant at 1.4.

TABLE VIII.- NONEQUILIBRIUM AIR STAGNATION WALL CONDITIONS FOR A NONCATALYTIC WALL AND MASS INJECTION OF EQUILIBRIUM AIR

[Altitude, 60.96 km;
$U_\infty^* = 6.096$ km/s;
$a^* = 2.54$ cm;
$N_{Re,\infty} = 2.597 \times 10^3$;
$N_{Re,s} = 1.914 \times 10^2$;
Multicomponent diffusion]

Properties[a]	Wall conditions for nondimensional mass-injection rate of –				
	0.0	0.1	0.2	0.3	0.4
Temperature, K	1.500×10^3	1.500×10^3	1.500×10^3	1.500×10^3	1.500×10^3
Pressure, atm	9.457×10^{-2}	9.457×10^{-2}	9.457×10^{-2}	9.457×10^{-2}	9.457×10^{-2}
Density, kg/cm^3	1.811×10^{-2}	1.974×10^{-2}	2.104×10^{-2}	2.180×10^{-2}	2.208×10^{-2}
Viscosity, $N\text{-}s/m^2$	5.218×10^{-5}	5.270×10^{-5}	5.289×10^{-5}	5.289×10^{-5}	5.289×10^{-5}
Velocity, km/s	0.0	8.382×10^{-3}	1.568×10^{-2}	2.271×10^{-2}	2.988×10^{-2}
Enthalpy, MJ/kg	5.945×10^0	3.735×10^0	2.403×10^0	1.671×10^0	1.418×10^0
Molecular weight, g/g-mole	2.360×10^1	2.573×10^1	2.742×10^1	2.843×10^1	2.879×10^1
Prandtl number	6.813×10^{-1}	6.876×10^{-1}	6.922×10^{-1}	6.950×10^{-1}	6.960×10^{-1}
Mass fractions:					
O	2.052×10^{-1}	1.284×10^{-1}	5.971×10^{-2}	1.839×10^{-2}	3.385×10^{-3}
O_2	2.935×10^{-3}	8.712×10^{-2}	1.737×10^{-1}	2.232×10^{-1}	2.352×10^{-1}
N	3.687×10^{-2}	5.854×10^{-3}	6.389×10^{-4}	3.818×10^{-5}	1.089×10^{-6}
N_2	7.298×10^{-1}	7.357×10^{-1}	7.394×10^{-1}	7.506×10^{-1}	7.583×10^{-1}
NO	2.320×10^{-2}	4.115×10^{-2}	2.622×10^{-2}	7.638×10^{-3}	3.098×10^{-3}

[a] See table VII for shock properties..

TABLE IX.- CONSTANTS FOR POLYNOMIAL APPROXIMATIONS OF THERMODYNAMIC PROPERTIES

[Equations (B1) to (B3)]

Species	Coefficients						
	a_1	a_2	a_3	a_4	a_5	a_6	a_7
1000 K to 6000 K							
O	2.670	-1.970×10^{-4}	7.193×10^{-8}	-8.901×10^{-12}	4.002×10^{-16}	2.915×10^{4}	4.504
O_2	3.316	1.151×10^{-3}	-3.726×10^{-7}	6.186×10^{-11}	-3.666×10^{-15}	-1.044×10^{3}	5.393
N	2.474	9.097×10^{-5}	-7.814×10^{-8}	2.218×10^{-11}	-1.489×10^{-15}	5.609×10^{4}	4.300
N_2	3.221	9.878×10^{-4}	-2.907×10^{-7}	3.938×10^{-11}	-2.000×10^{-15}	-1.043×10^{3}	4.326
NO	3.221	1.221×10^{-3}	-4.297×10^{-7}	6.559×10^{-11}	-3.451×10^{-15}	9.764×10^{3}	6.610
6000 K to 15 000 K							
O	2.548	-5.952×10^{-5}	2.701×10^{-8}	-2.798×10^{-12}	9.380×10^{-17}	2.915×10^{4}	5.049
O_2	3.721	4.254×10^{-4}	-2.835×10^{-8}	6.050×10^{-13}	-5.186×10^{-18}	-1.044×10^{3}	3.254
N	2.746	-3.909×10^{-4}	1.338×10^{-7}	-1.191×10^{-11}	3.365×10^{-14}	5.609×10^{4}	2.872
N_2	3.727	4.684×10^{-4}	-1.140×10^{-7}	1.154×10^{-11}	-3.293×10^{-16}	-1.043×10^{3}	1.294
NO	3.345	2.521×10^{-4}	-2.658×10^{-8}	2.162×10^{-12}	-6.381×10^{-17}	9.764×10^{3}	3.212

TABLE X.- MOLECULAR CONSTANTS

Species	ϵ/k, K	σ, Å	M, g/g-mole
O	106.7	3.050	16.00
O_2	106.7	3.467	32.00
N	71.4	3.298	14.01
N_2	71.4	3.798	28.02
NO	116.7	3.492	30.01

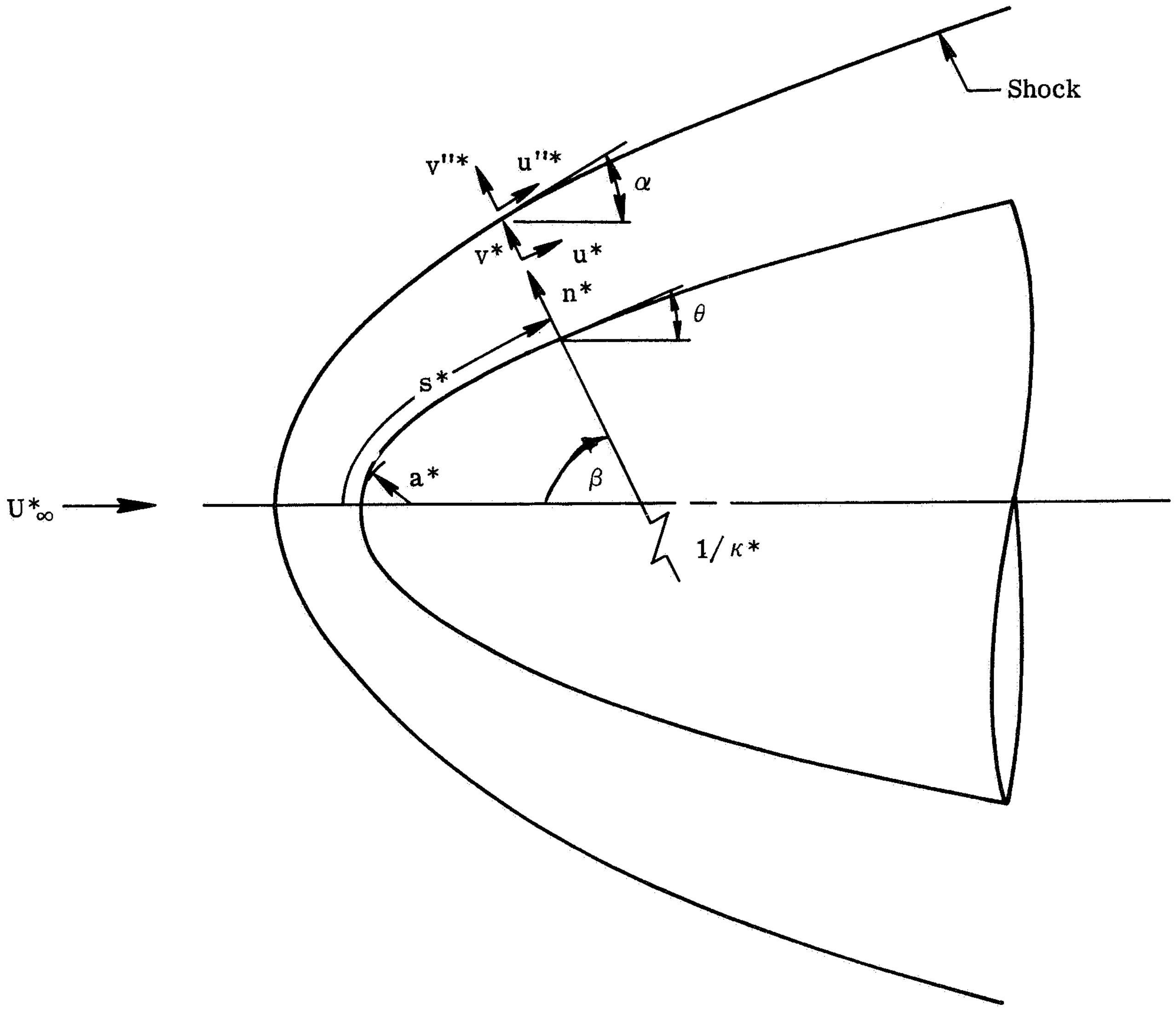

Figure 1.- Coordinate system.

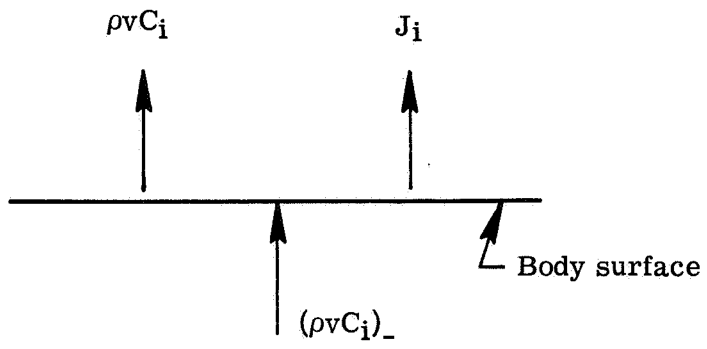

(a) Mass balance at gas-solid interface.

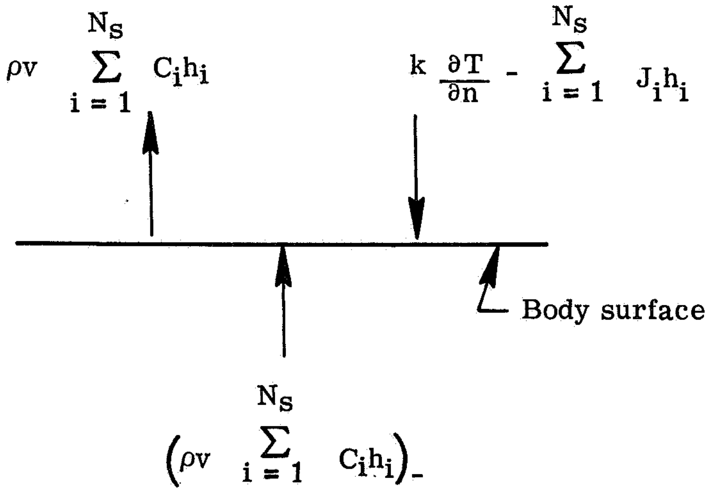

(b) Energy balance at gas-solid interface.

Figure 2.- Surface mass and energy balances.

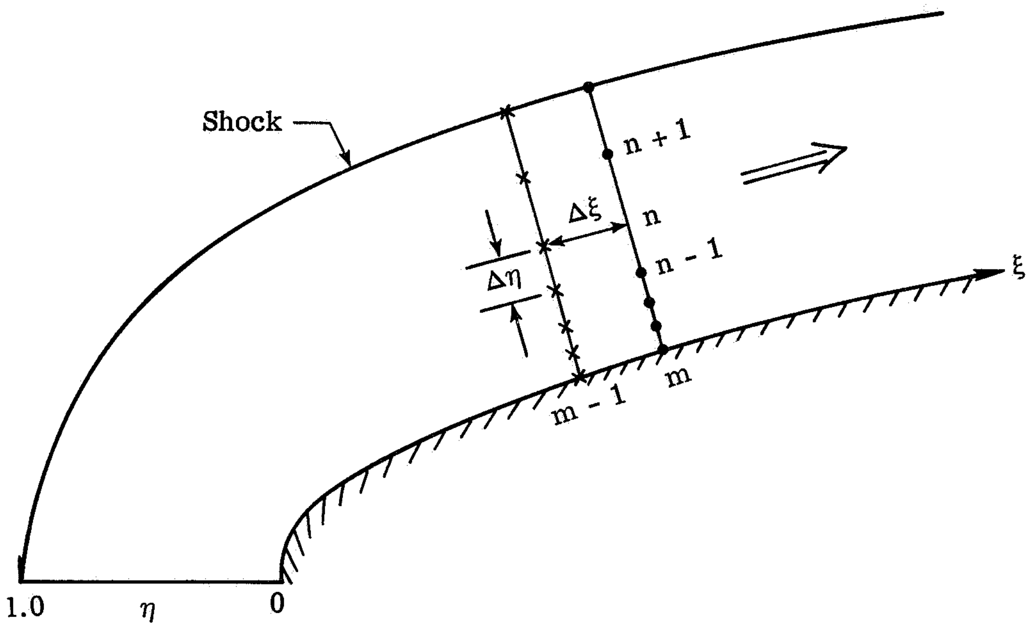

Figure 3.- Finite-difference representation of flow field.

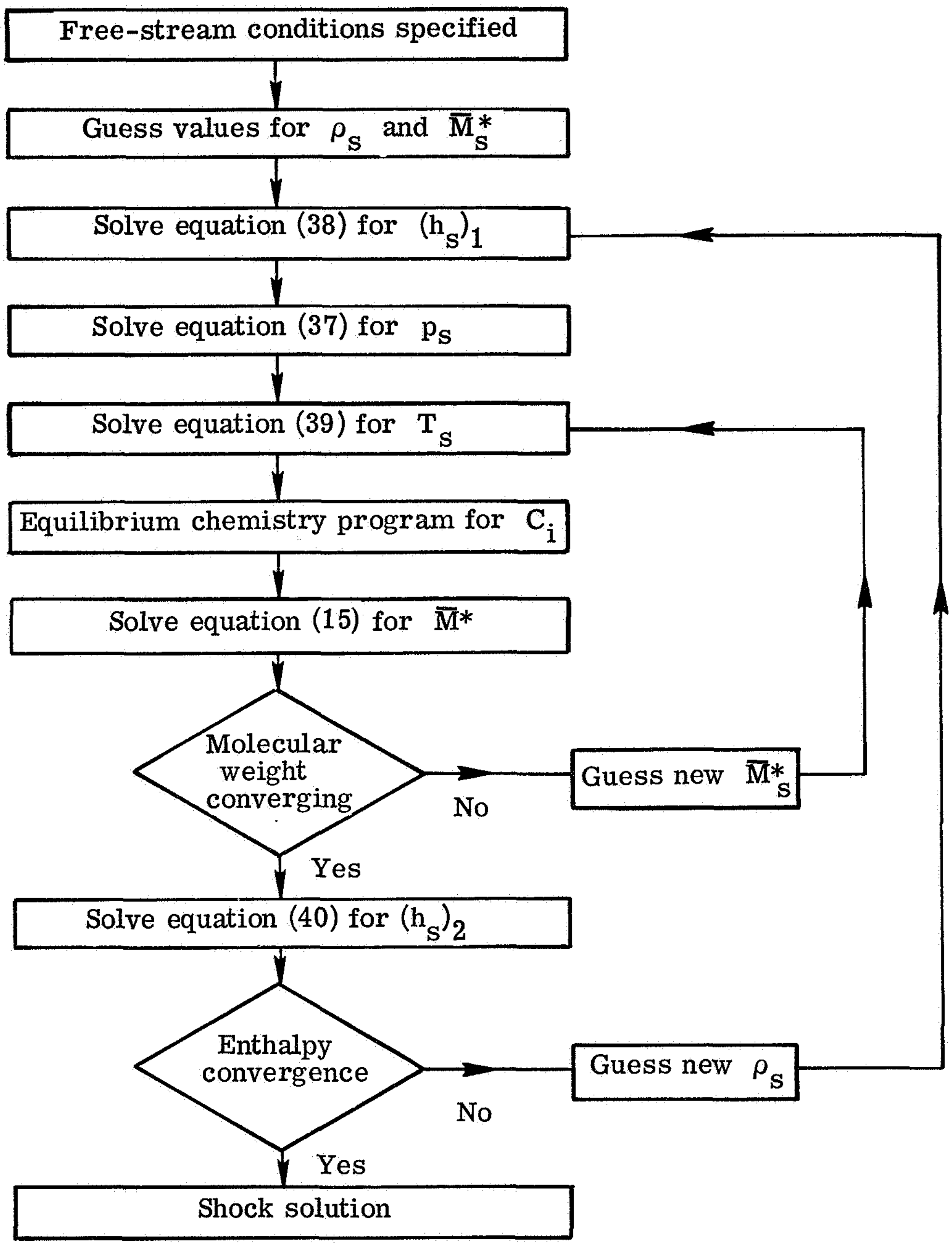

(a) Shock in chemical equilibrium.

Figure 4.- Flow chart for shock solution procedure.

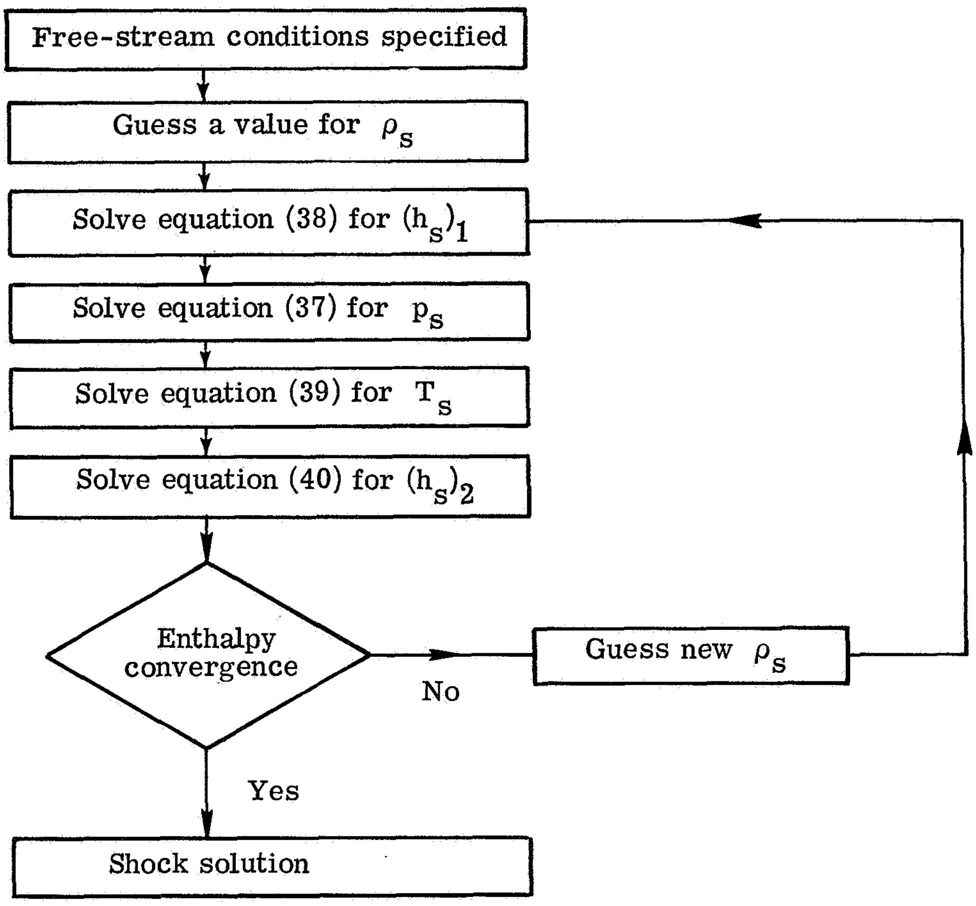

(b) Shock frozen at free-stream chemistry.

Figure 4.- Concluded.

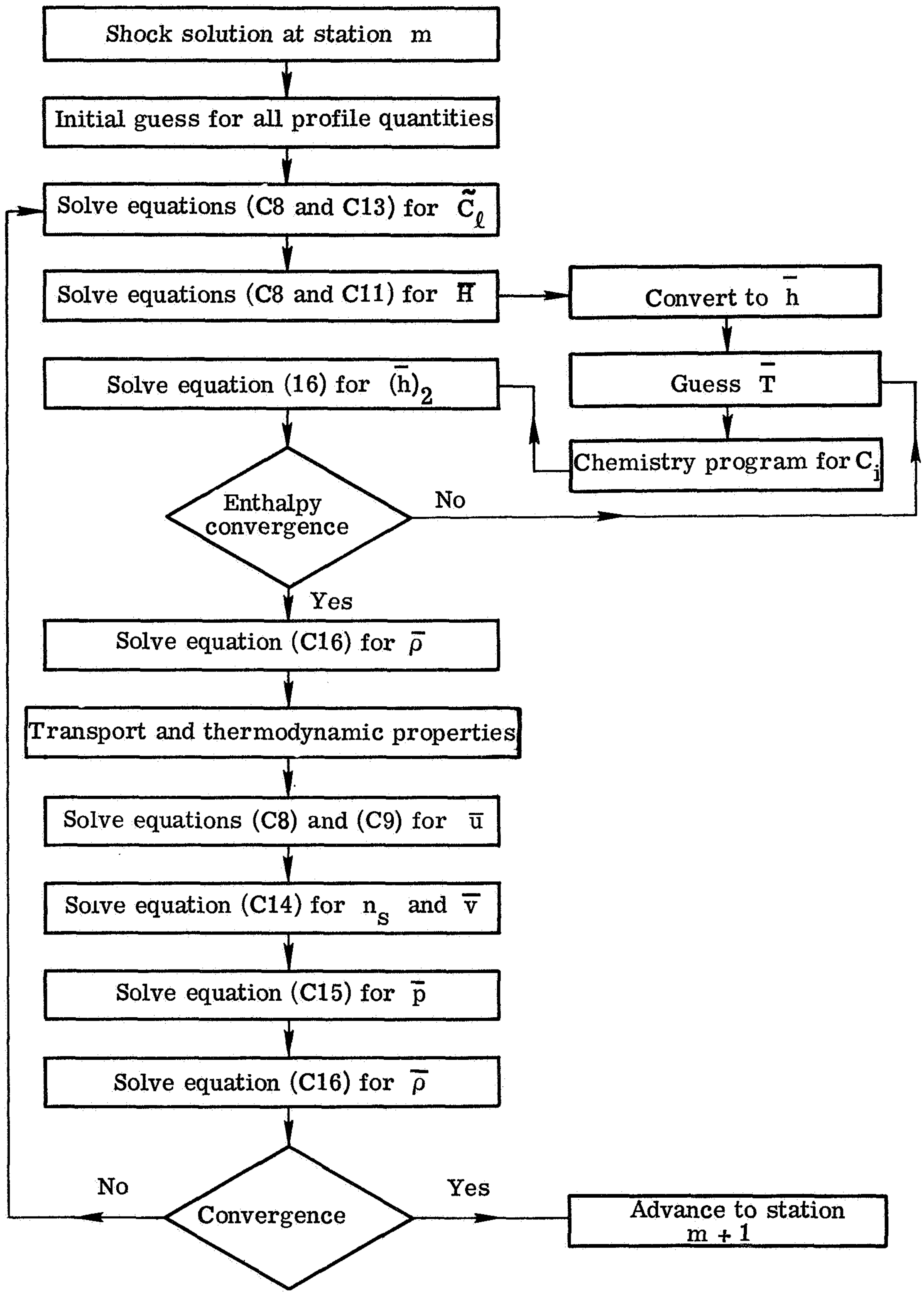

(a) Equilibrium chemistry.

Figure 5.- Flow chart for solution sequence of viscous-shock-layer equations.

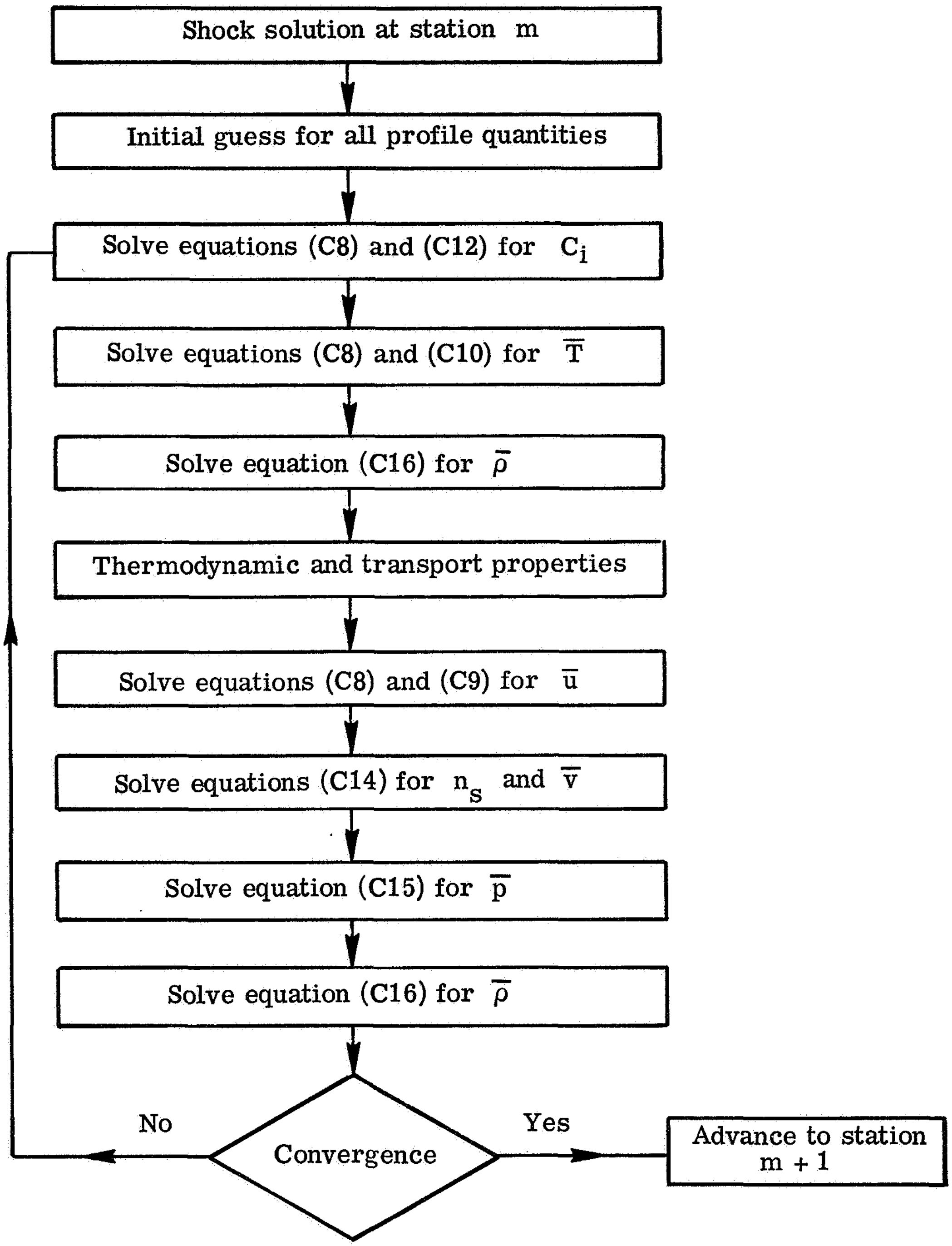

(b) Frozen and nonequilibrium chemistry.

Figure 5.- Concluded.

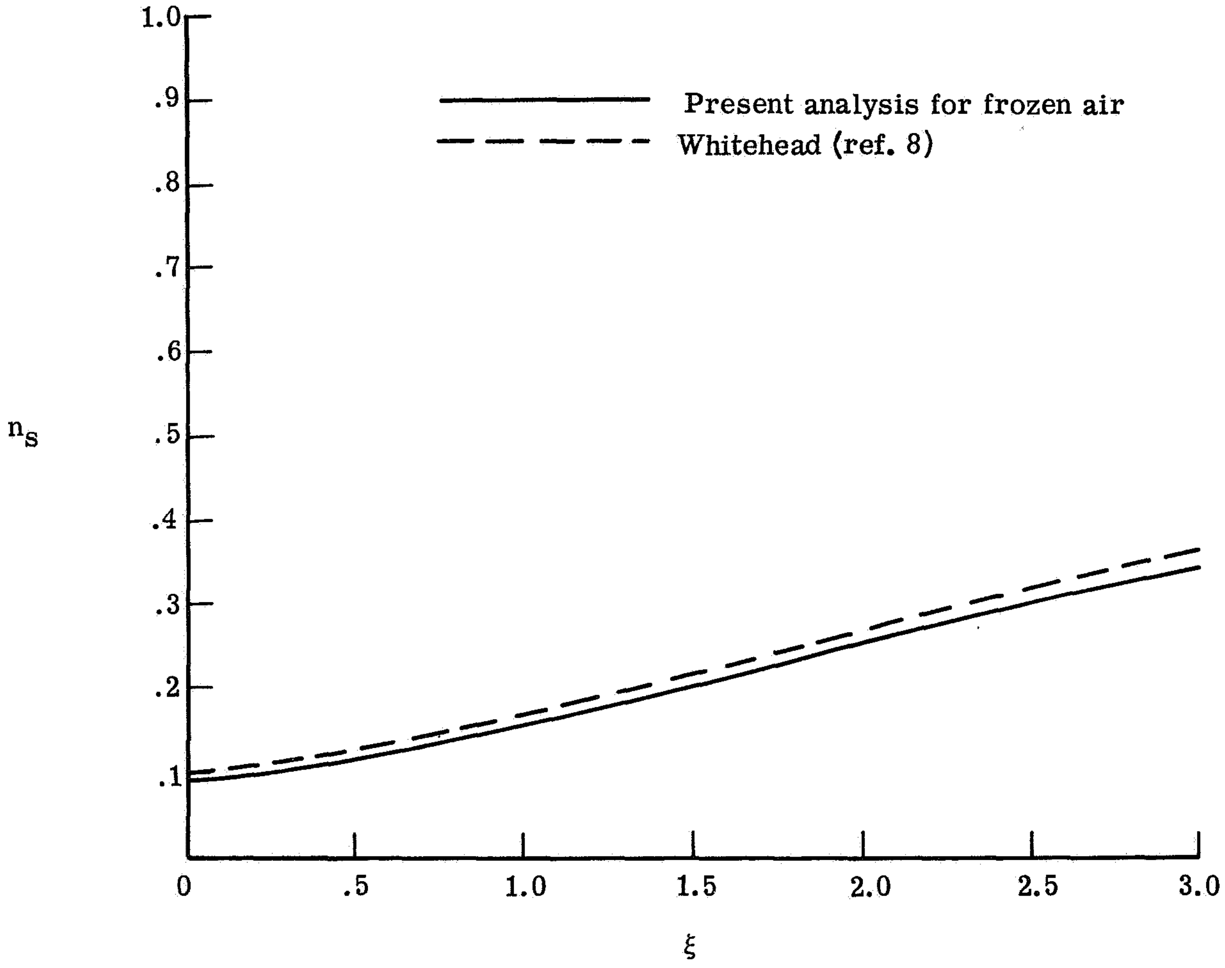

(a) Shock standoff variation with distance along body surface.

Figure 6.- Comparison of present calculations with results of Whitehead for frozen air at an altitude of 60.96 km. $U_\infty^* = 6.10$ km/s; $T_w^* = 1000$ K; $a^* = 2.54$ cm.

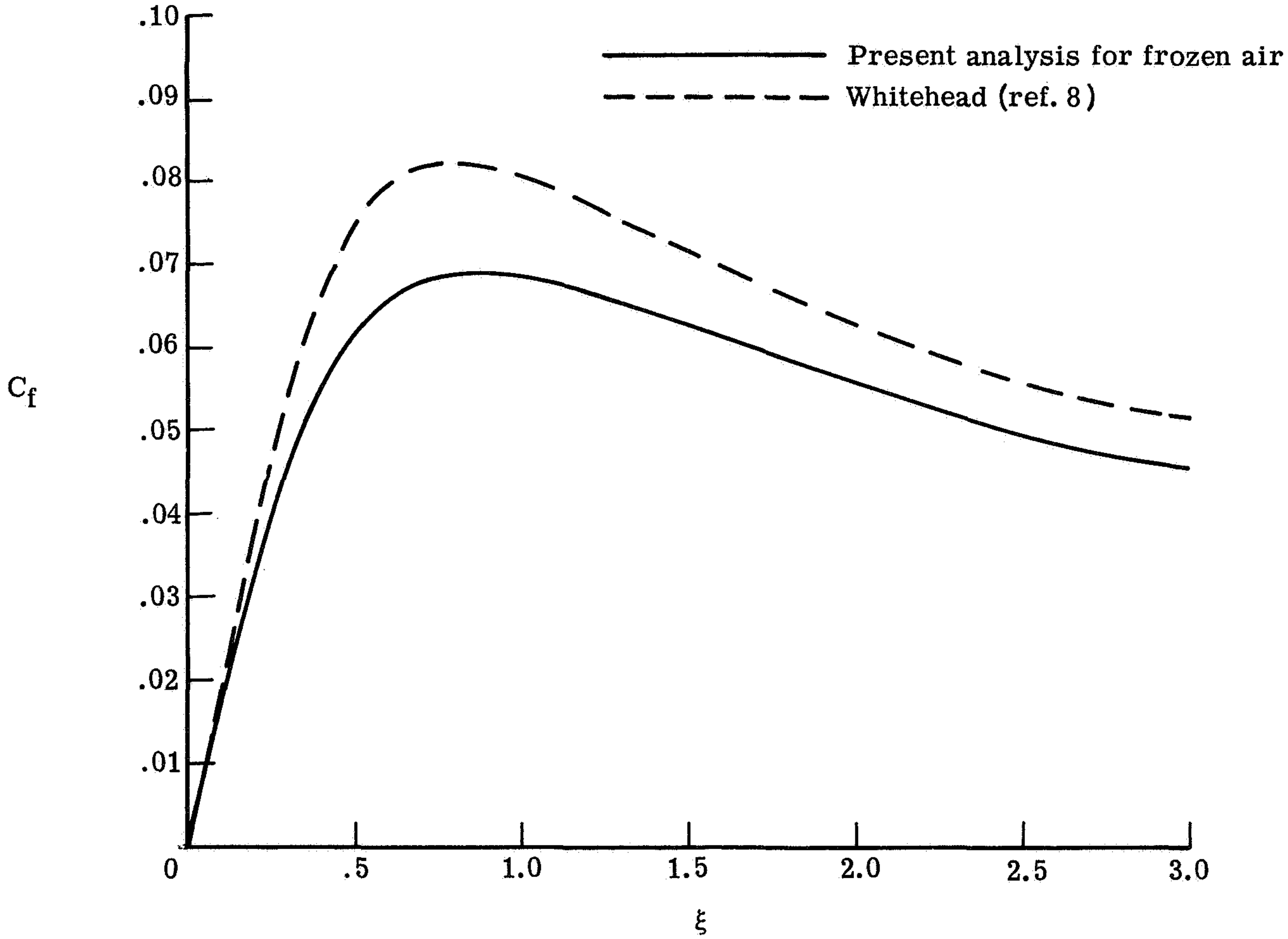

(b) Skin-friction variation with distance along body surface.

Figure 6.- Continued.

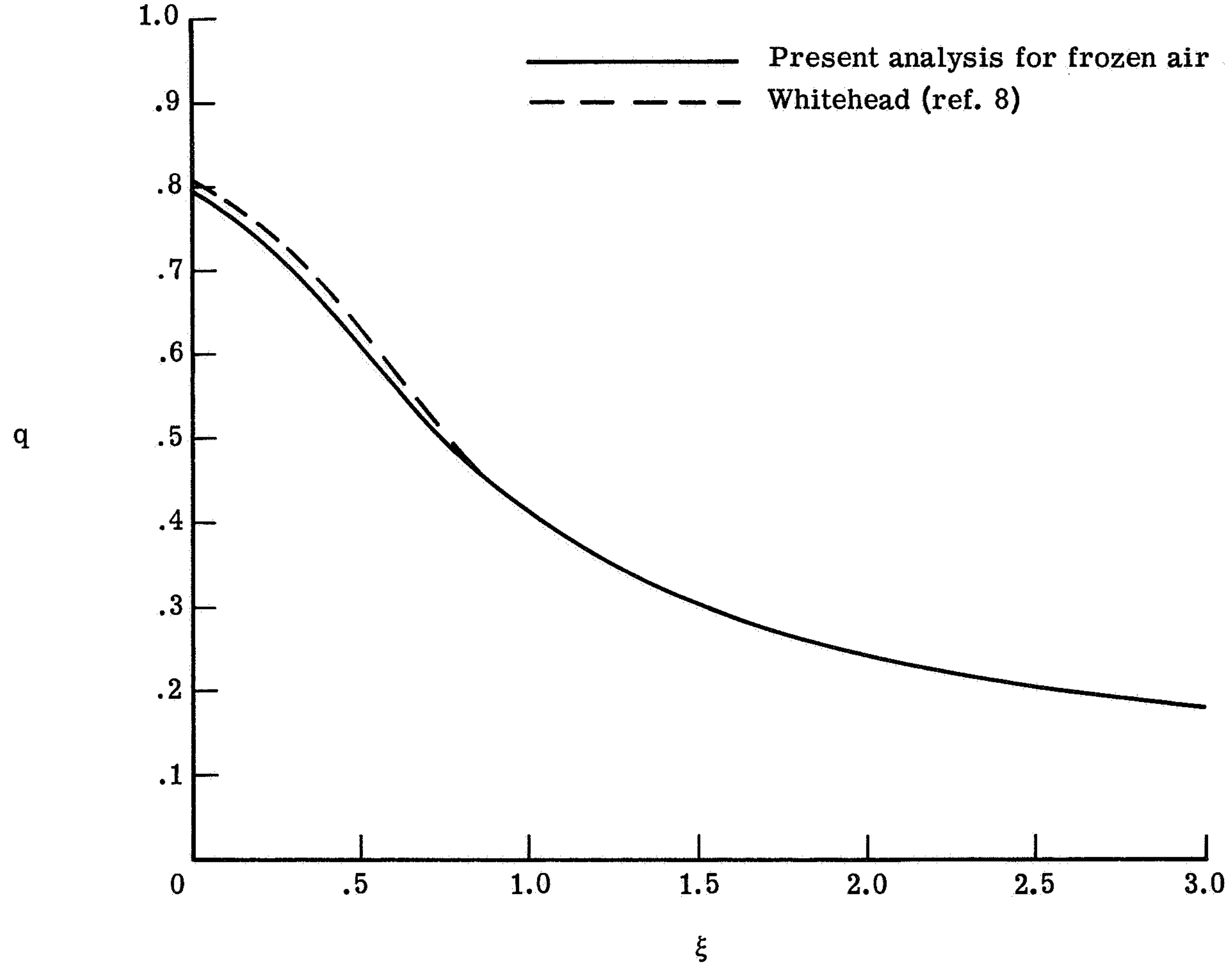

(c) Heat transfer variation with distance along body surface.

Figure 6.- Concluded.

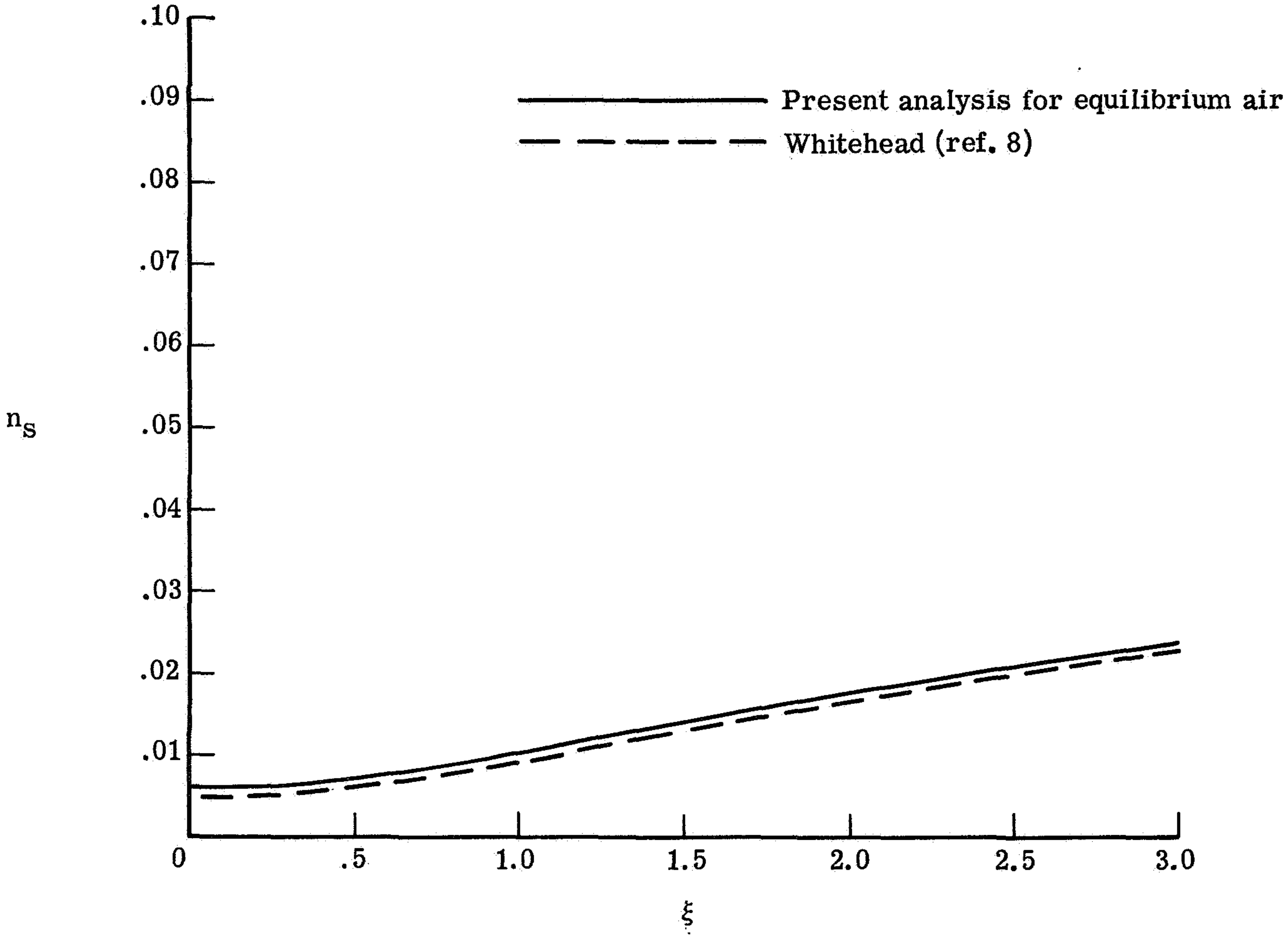

(a) Shock standoff variation with distance along body surface.

Figure 7.- Comparison of present calculations with results of Whitehead for equilibrium air at an altitude of 60.96 km. $U_\infty^* = 6.10$ km/s; $T_w^* = 1000$ K; $a^* = 2.54$ cm; binary diffusion; $L = 1.0$.

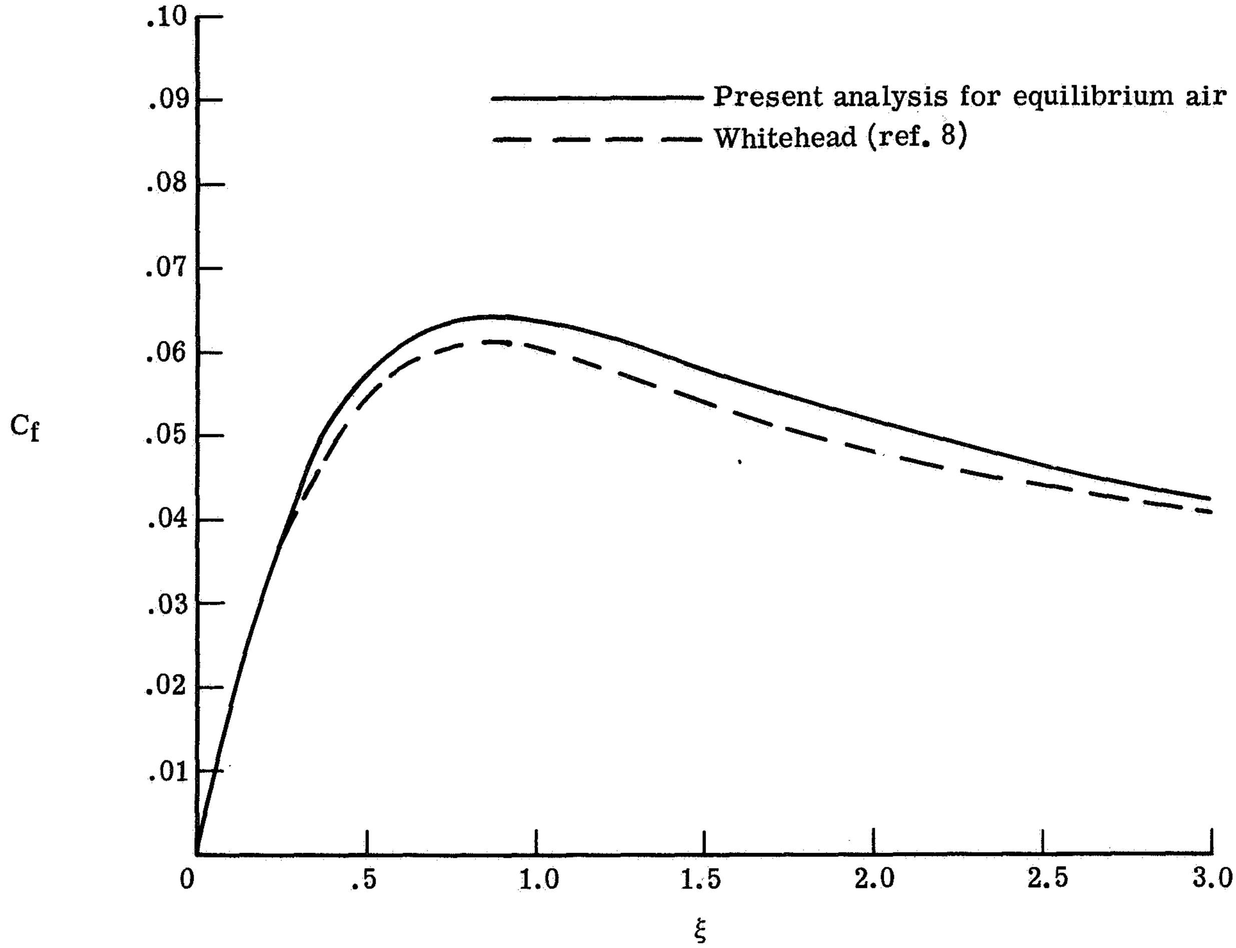

(b) Skin-friction variation with distance along body surface.

Figure 7.- Continued.

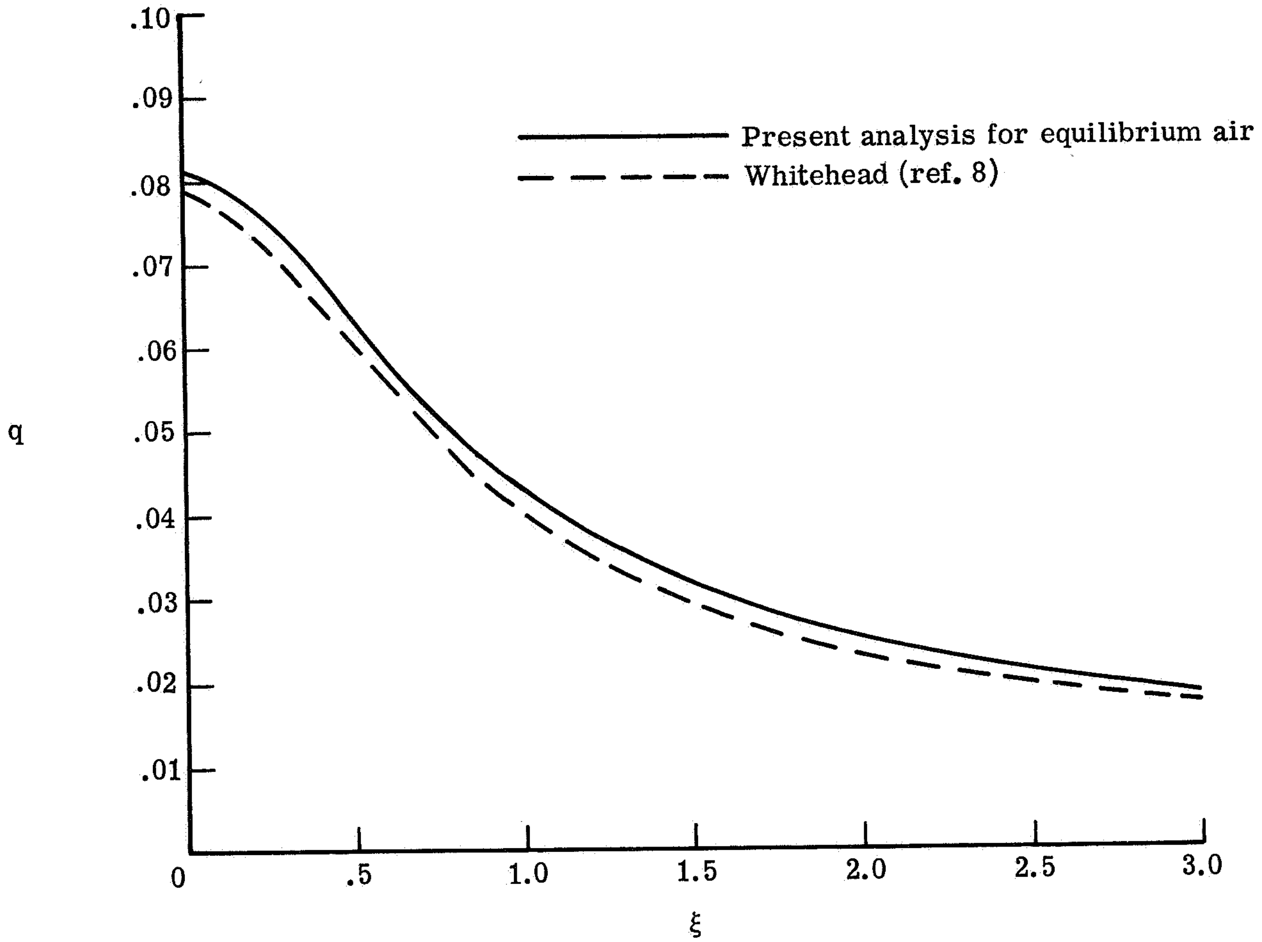

(c) Heat-transfer variation with distance along body surface.

Figure 7.- Concluded.

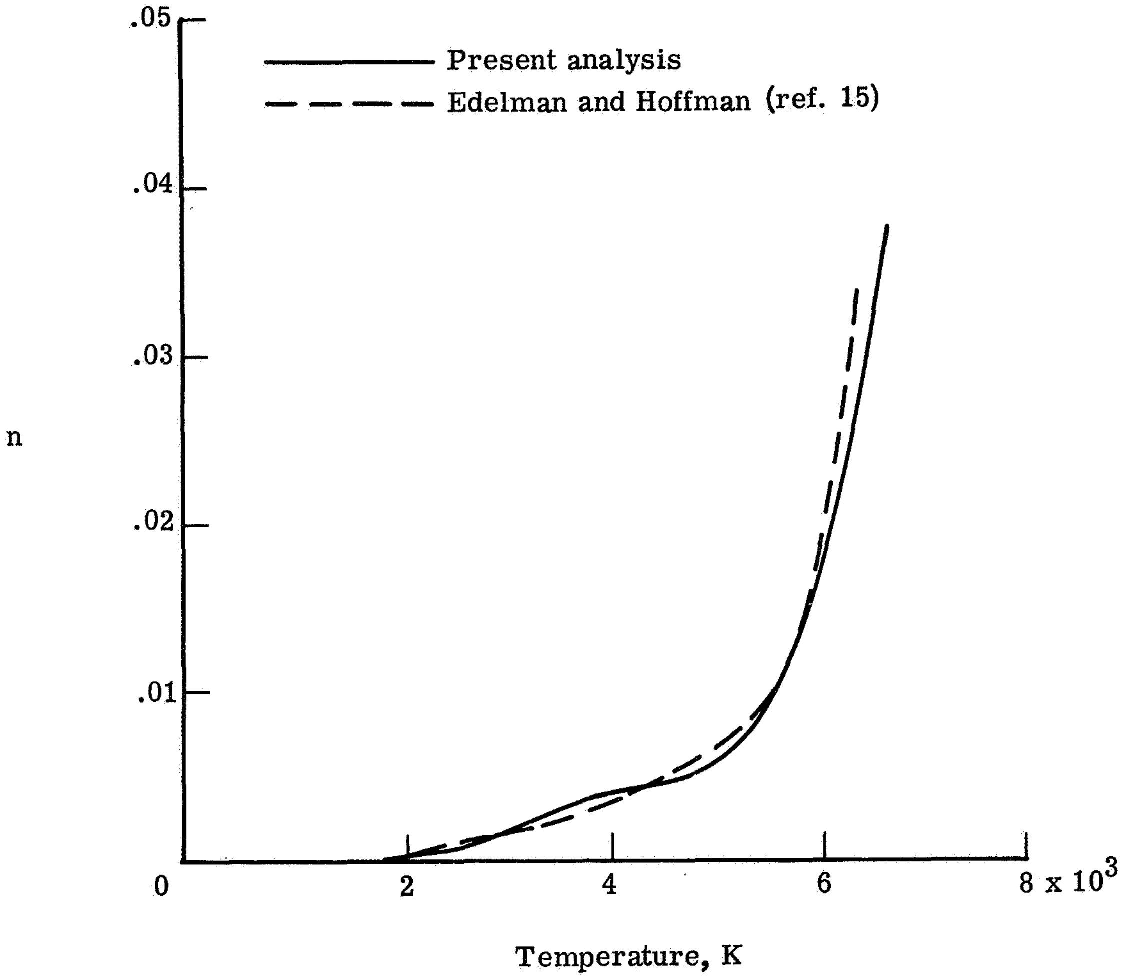

(a) Stagnation temperature profiles for an altitude of 85.34 km. $U_\infty^* = 7.92$ km/s; $a^* = 30.48$ cm; $T_w^* = 1350$ K; Lewis number = 1.4.

Figure 8.- Comparison of present calculations with stagnation results of Edelman and Hoffman for equilibrium air.

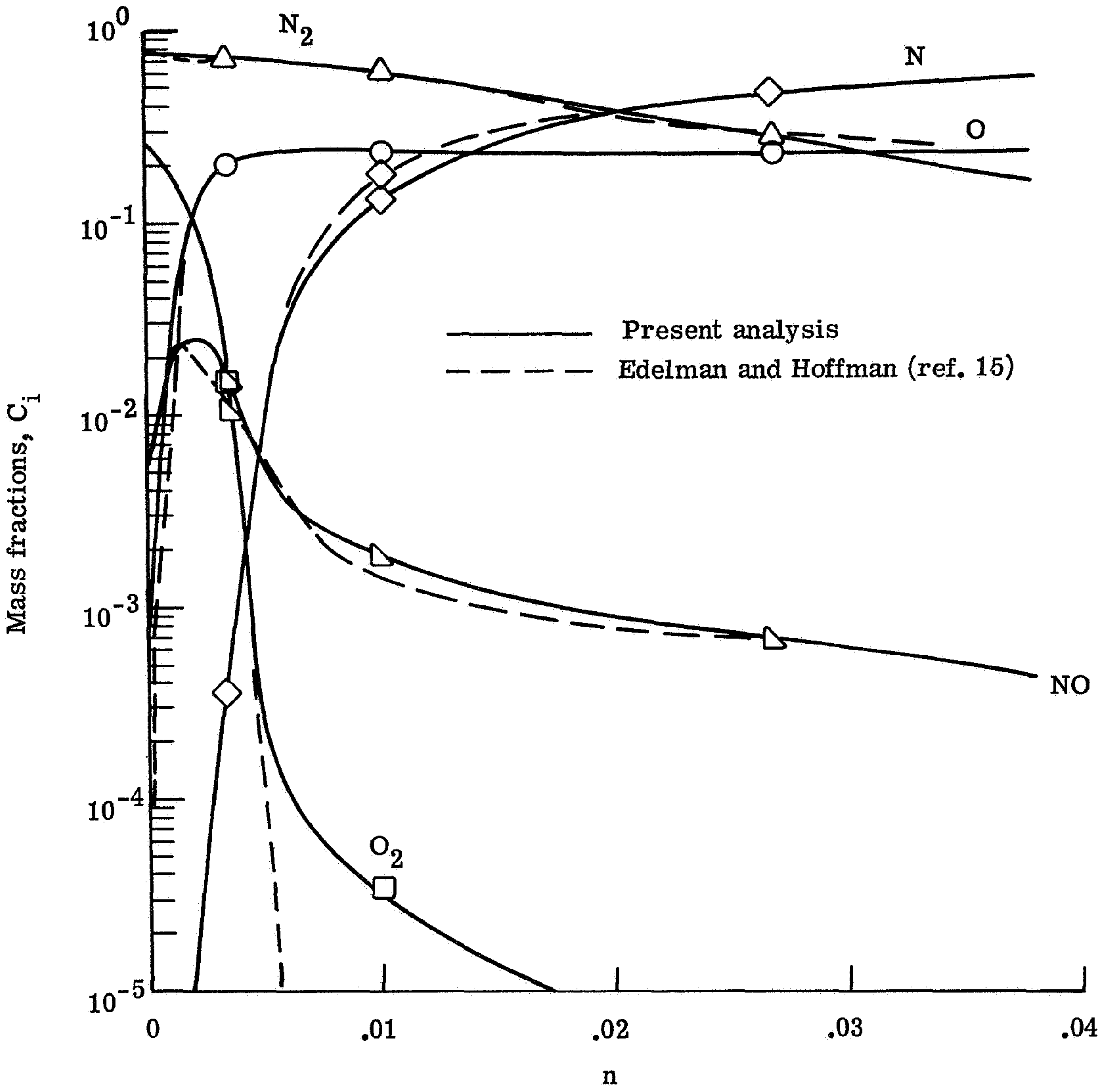

(b) Stagnation species profiles for an altitude of 85.34 km. $U_\infty^* = 7.92$ km/s; $a^* = 30.48$ cm; $T_W^* = 1350$ K; Lewis number = 1.4.

Figure 8.- Continued.

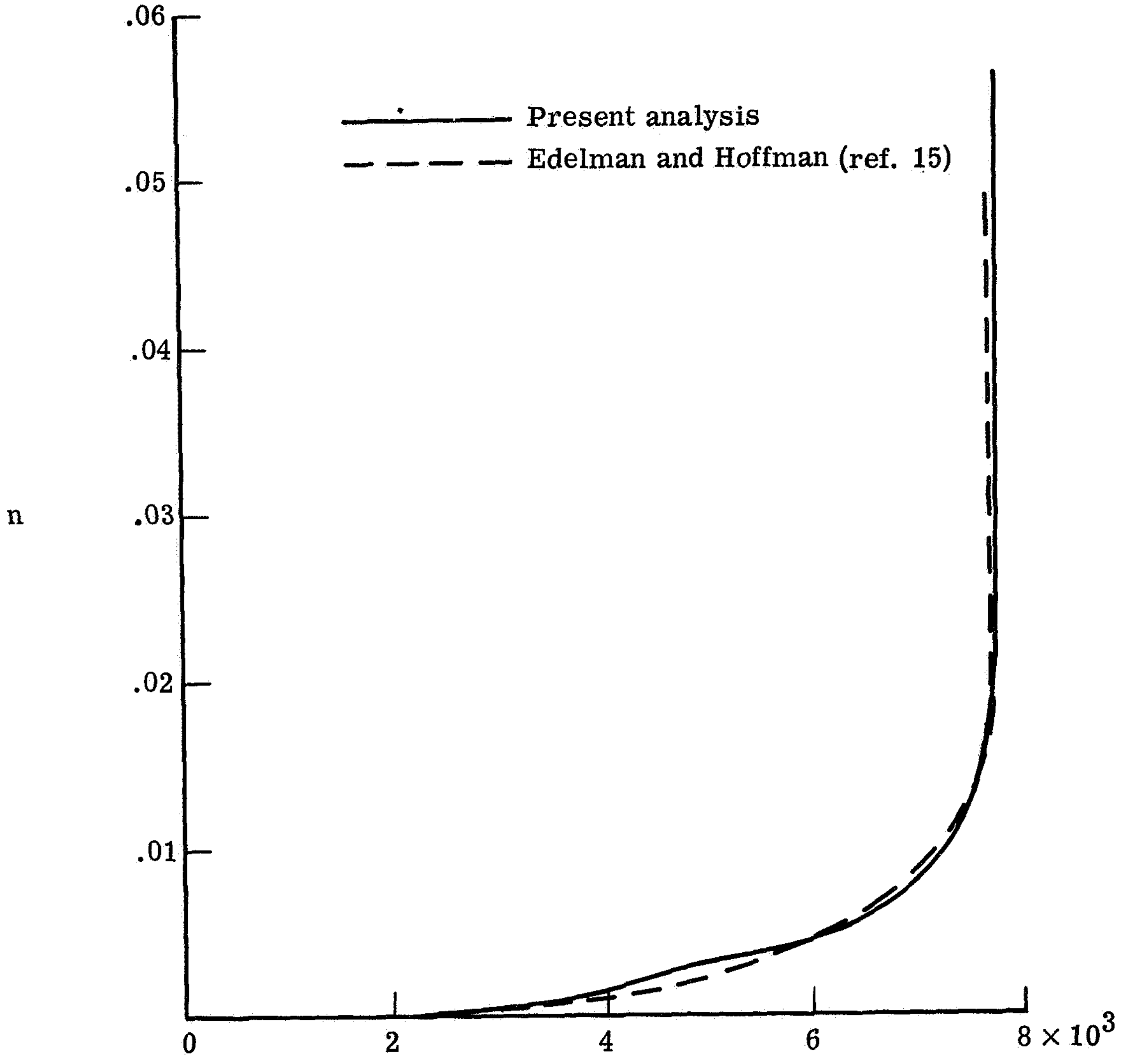

Temperature, K

(c) Stagnation temperature profiles for an altitude of 45.72 km. $U_\infty^* = 6.86$ km/s; $a^* = 1.27$ cm; $T_w^* = 1476$ K; Lewis number = 1.4.

Figure 8.- Continued.

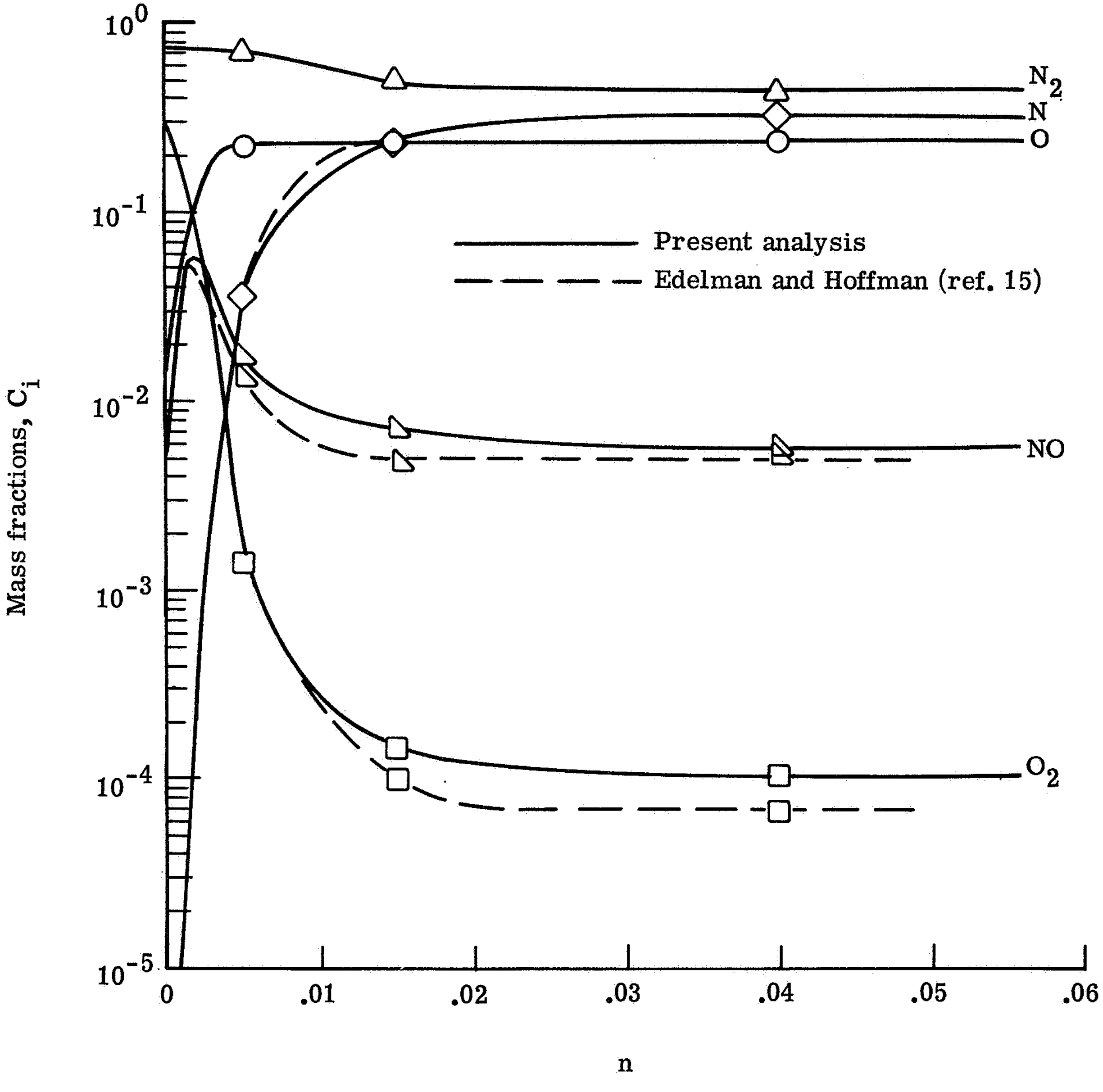

(d) Stagnation species profiles for an altitude of 45.72 km. $U_\infty^* = 6.86$ km/s; $a^* = 1.27$ cm; $T_w^* = 1476$ K; Lewis number = 1.4.

Figure 8.- Concluded.

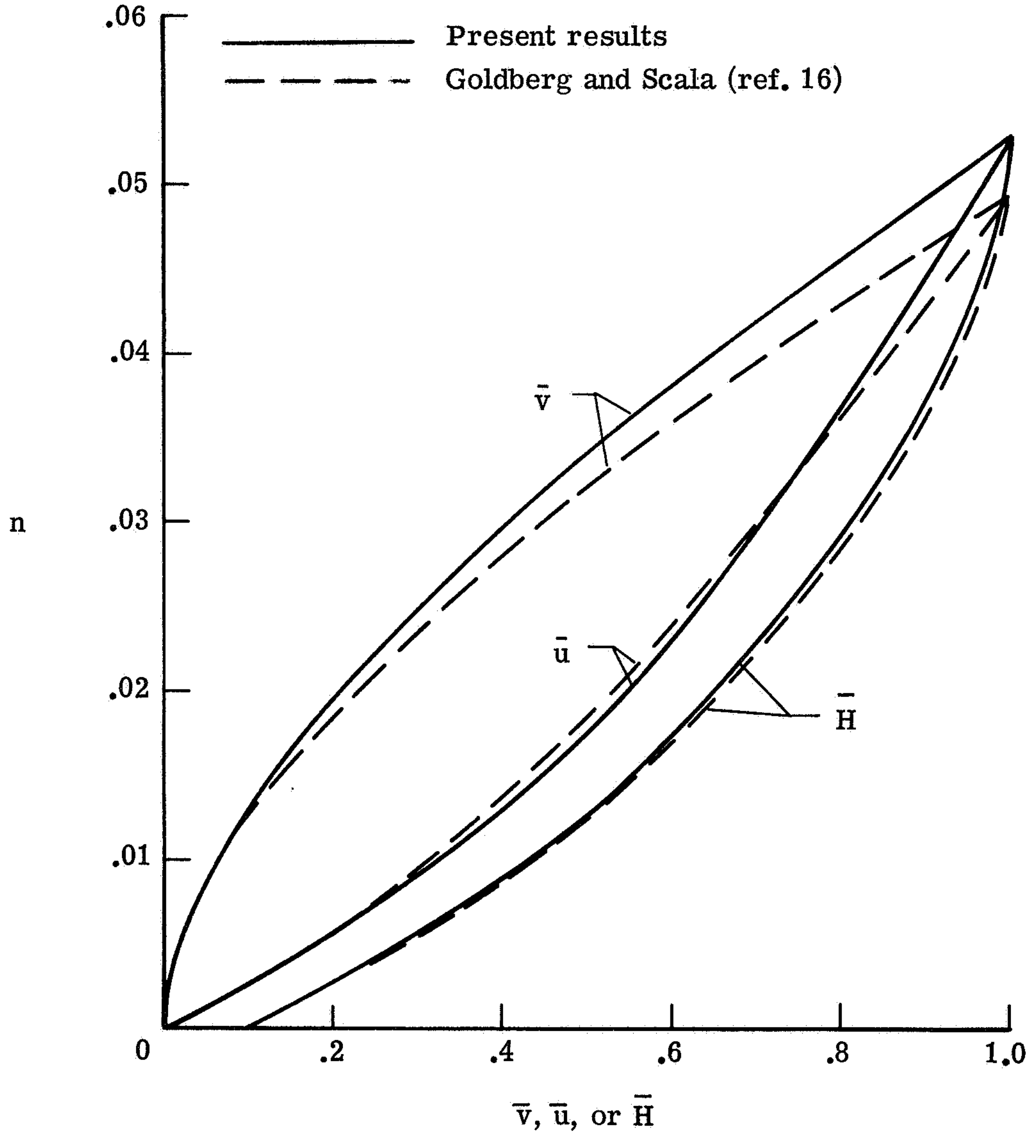

Figure 9.- Comparison of present results with stagnation results of Goldberg and Scala for equilibrium air at an altitude of 76.20 km. $U_\infty^* = 6.10$ km/s; $T_w^* = 1944$ K; Lewis number = 1.0; $N_{Re,s} = 100$.

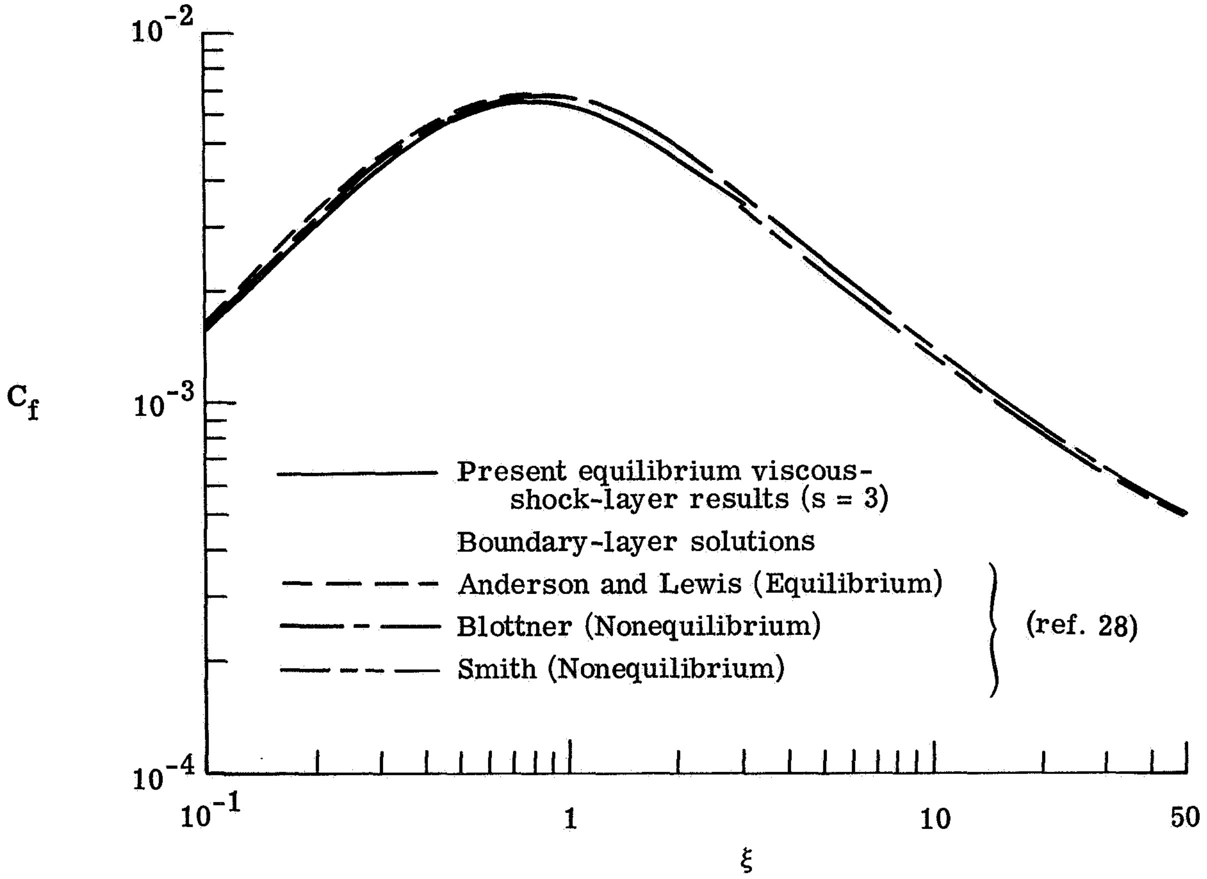

Figure 10.- Skin-friction distributions for a 10° half-angle hyperboloid at an altitude of 30.48 km. $U_\infty^* = 6.096$ km/s; $T_w^* = 1400$ K; $a^* = 2.54$ cm.

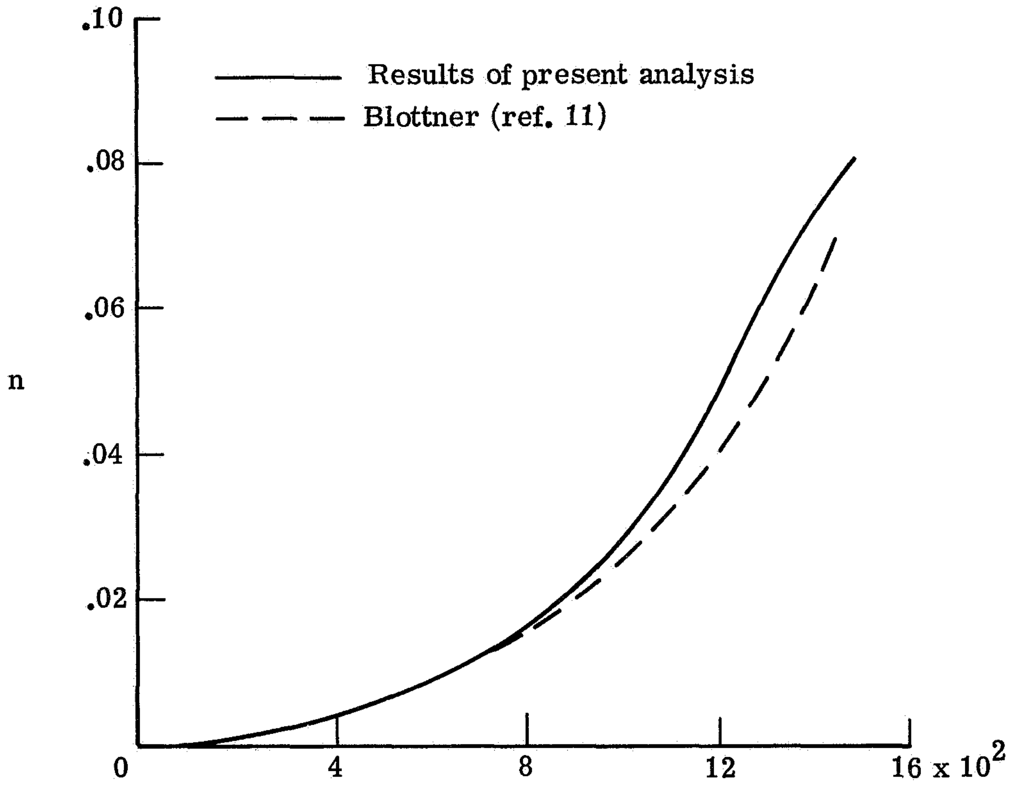

Temperature, K

(a) Stagnation temperature profiles.

Figure 11.- Comparison of present calculations with stagnation results of Blottner for nonequilibrium air at an altitude of 60.96 km. $U_\infty^* = 6.10$ km/s; $T_w^* = 1000$ K; $a^* = 2.54$ cm; Lewis number = 1.4; Catalytic wall.

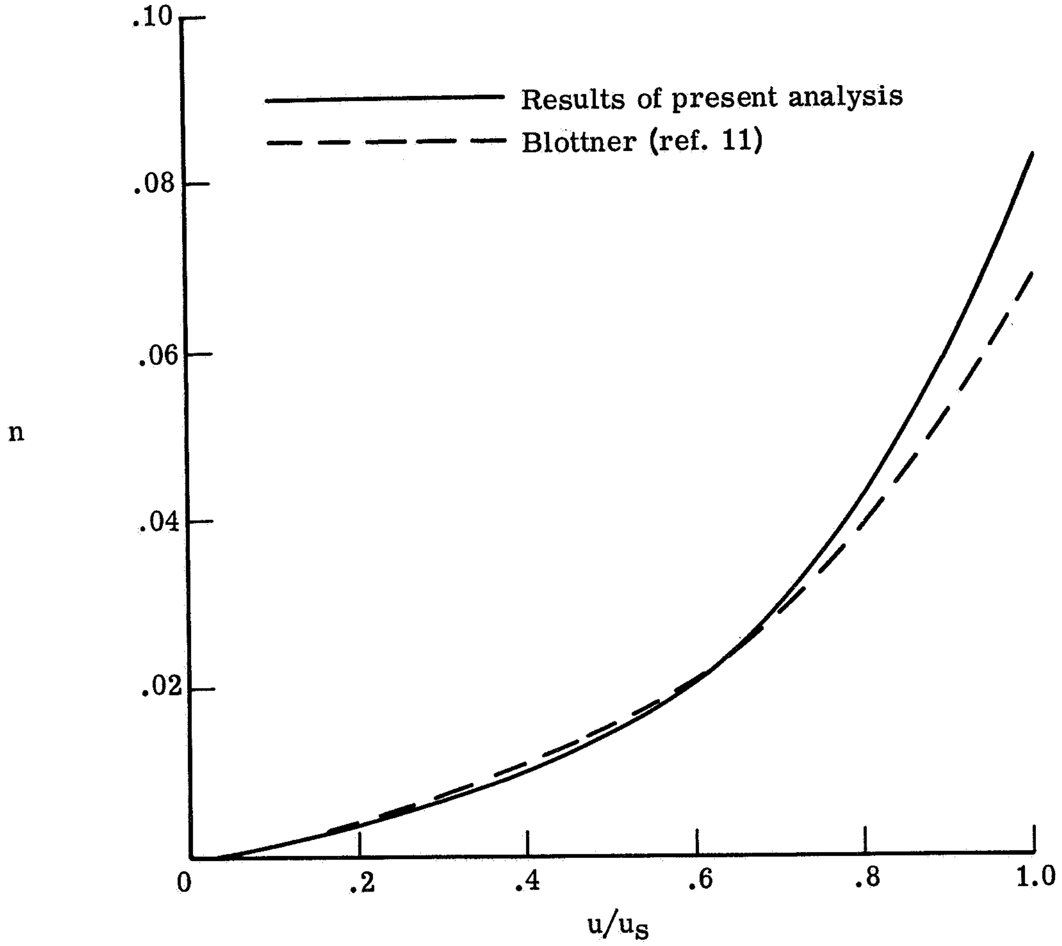

(b) Stagnation velocity ratio profiles.

Figure 11.- Continued.

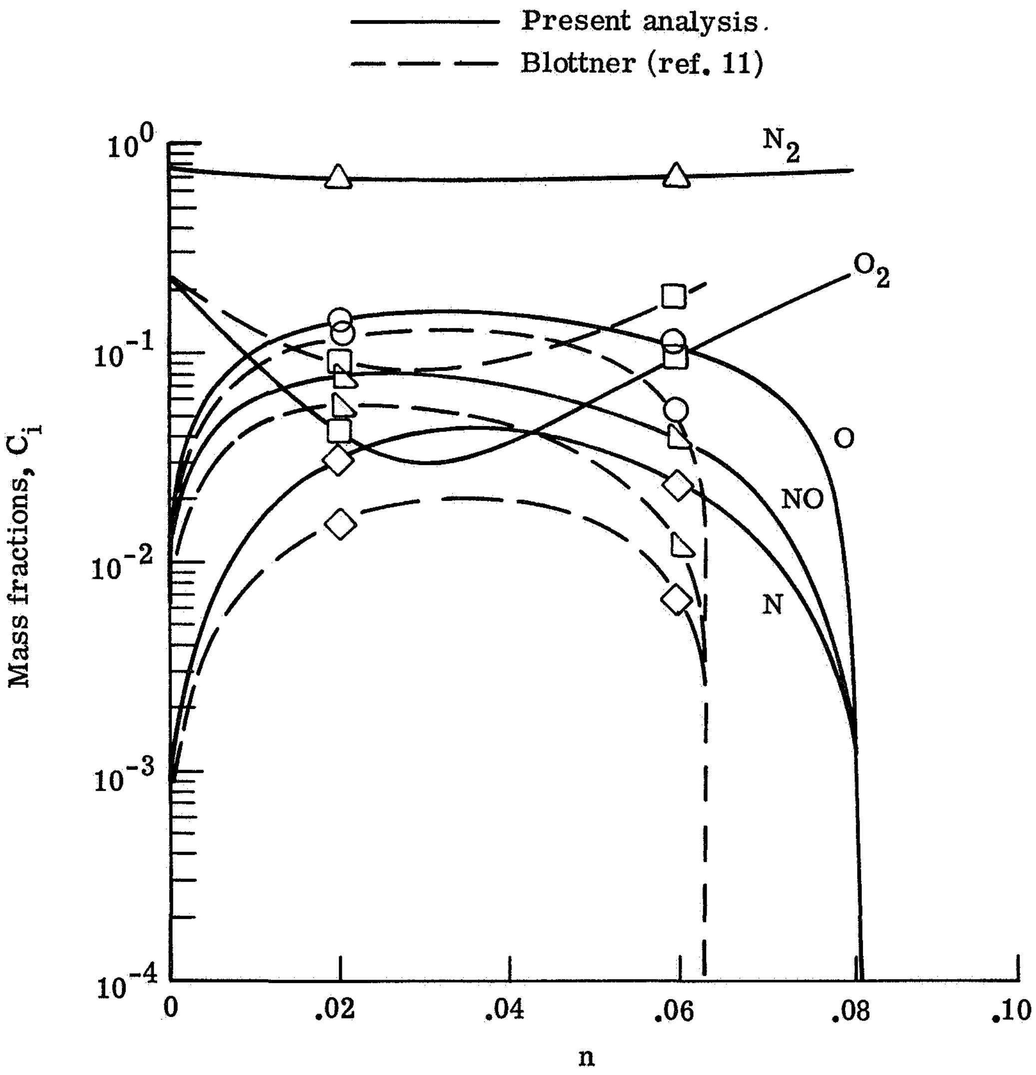

(c) Stagnation species profiles.

Figure 11.- Concluded.

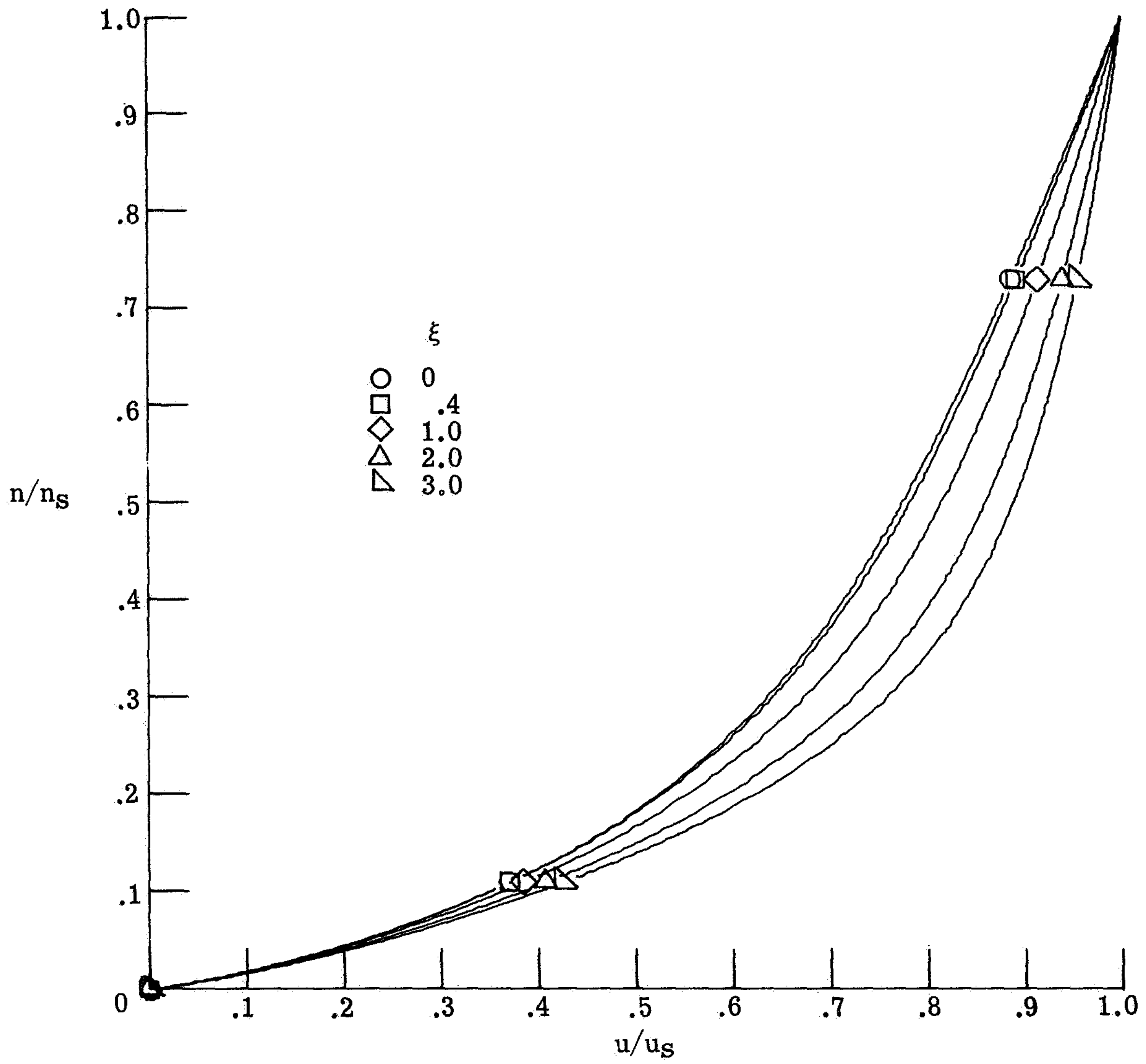

(a) Nonequilibrium chemistry.

Figure 12.- Velocity profiles for reacting and nonreacting air with multicomponent diffusion and no mass injection at an altitude of 60.96 km. $U_\infty^* = 6.10$ km/s; $T_w^* = 1500$ K; $a^* = 2.54$ cm; noncatalytic wall.

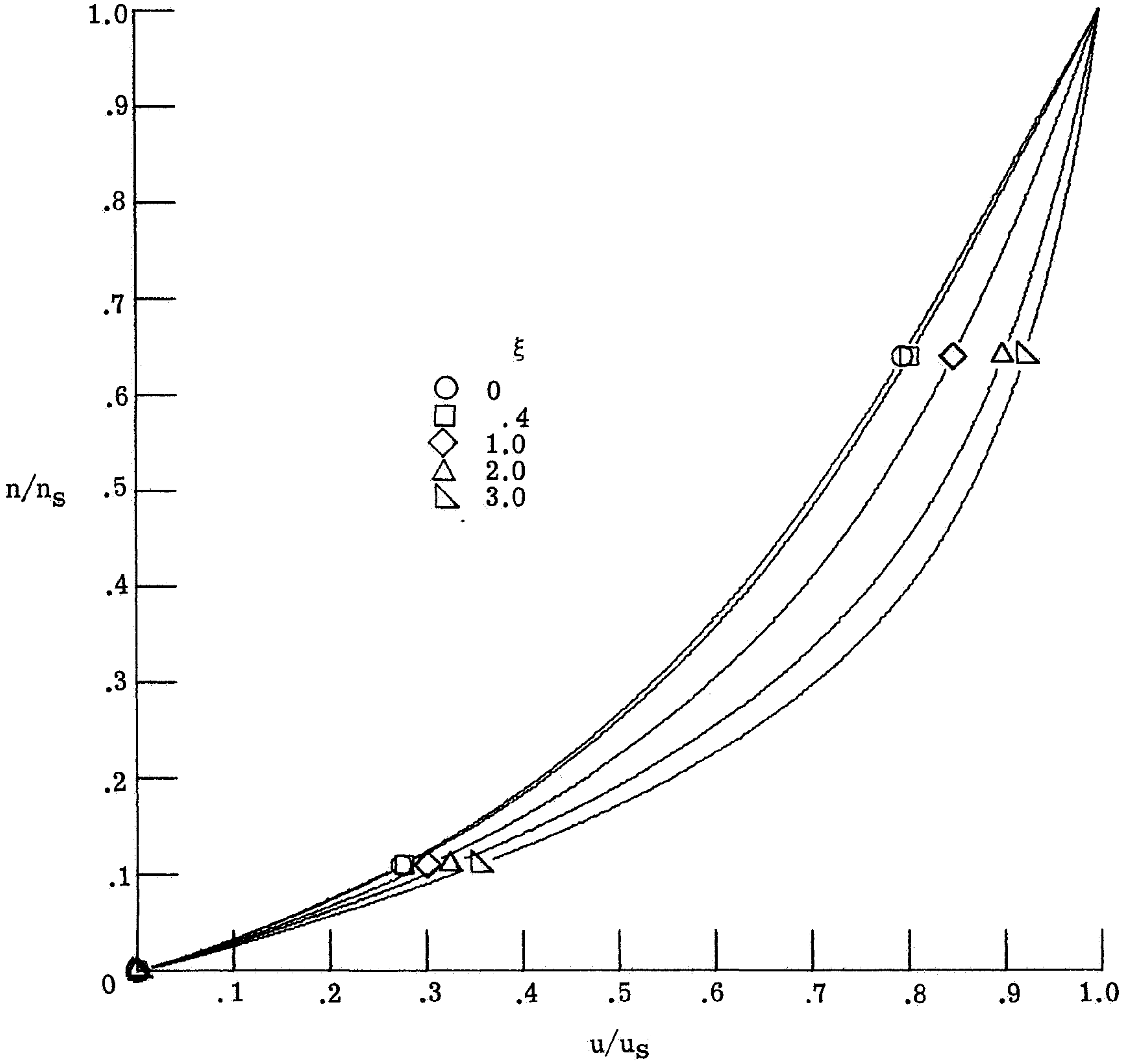

(b) Equilibrium chemistry.

Figure 12.- Continued.

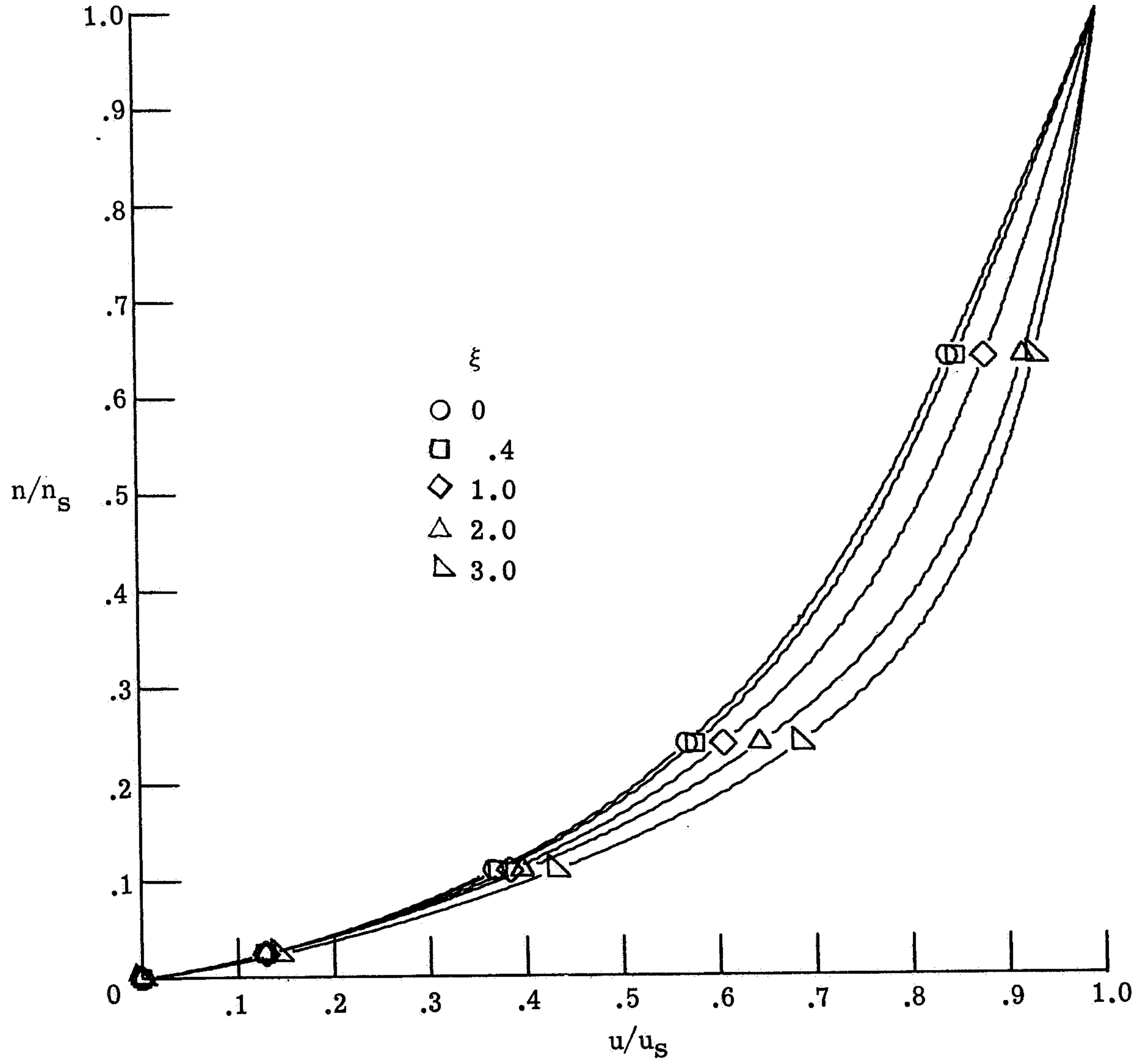

(c) Frozen chemistry.

Figure 12.- Concluded.

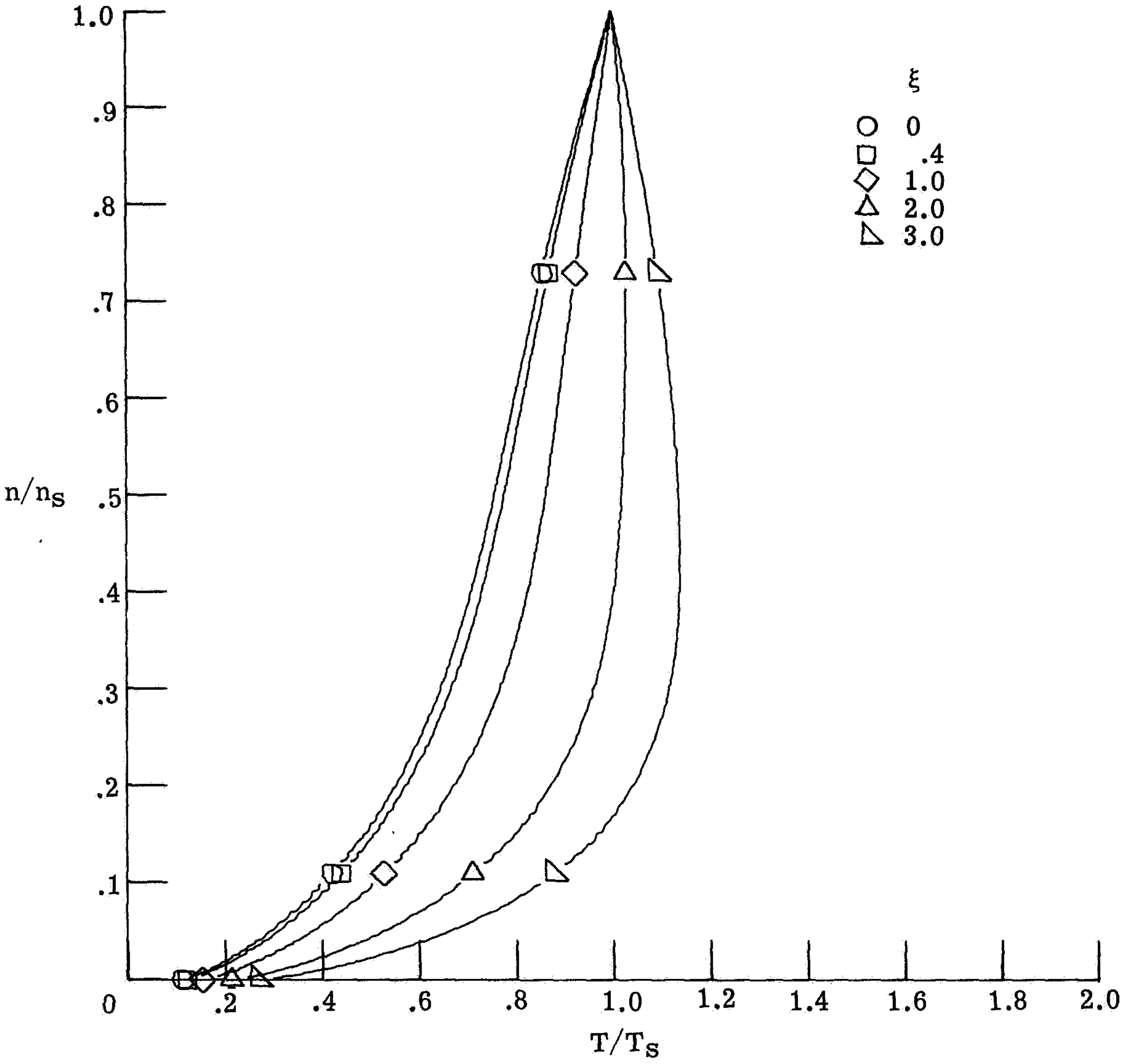

(a) Nonequilibrium chemistry.

Figure 13.- Temperature profiles for air with multicomponent diffusion and no mass injection at an altitude of 60.96 km. $U_\infty^* = 6.10$ km/s; $T_w^* = 1500$ K; $a^* = 2.54$ cm; noncatalytic wall.

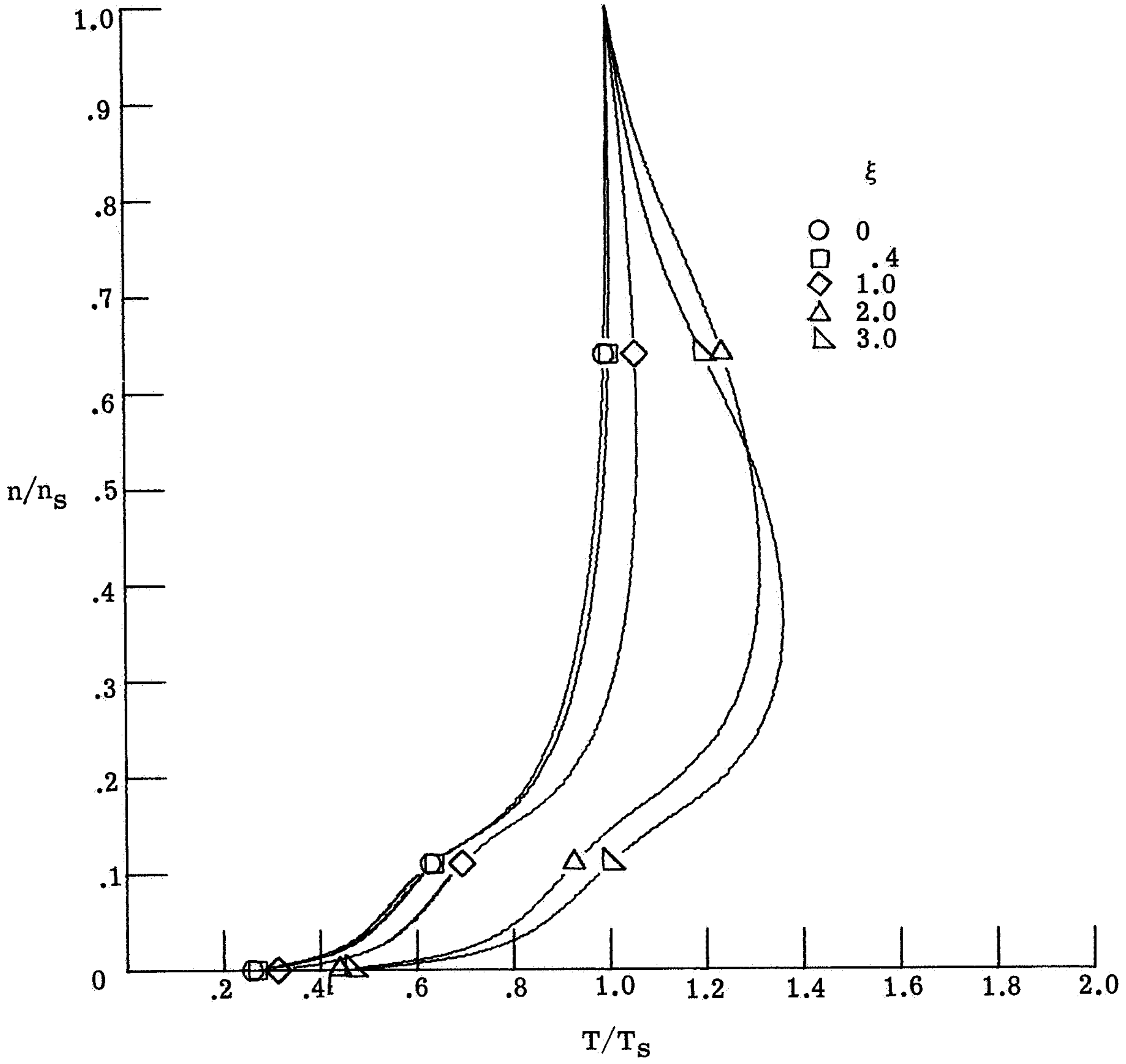

(b) Equilibrium chemistry.

Figure 13.- Continued.

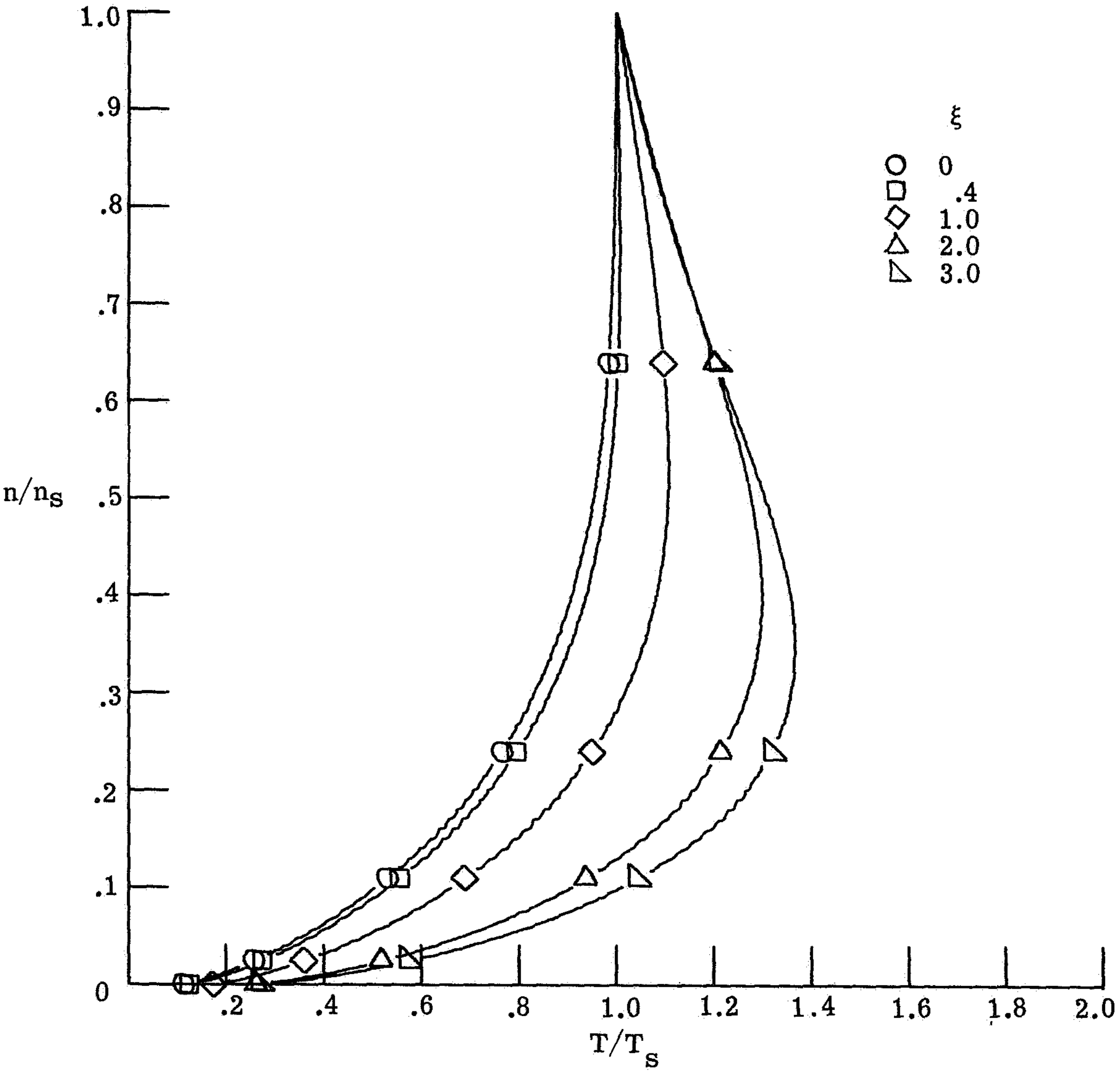

(c) Frozen chemistry.

Figure 13.- Concluded.

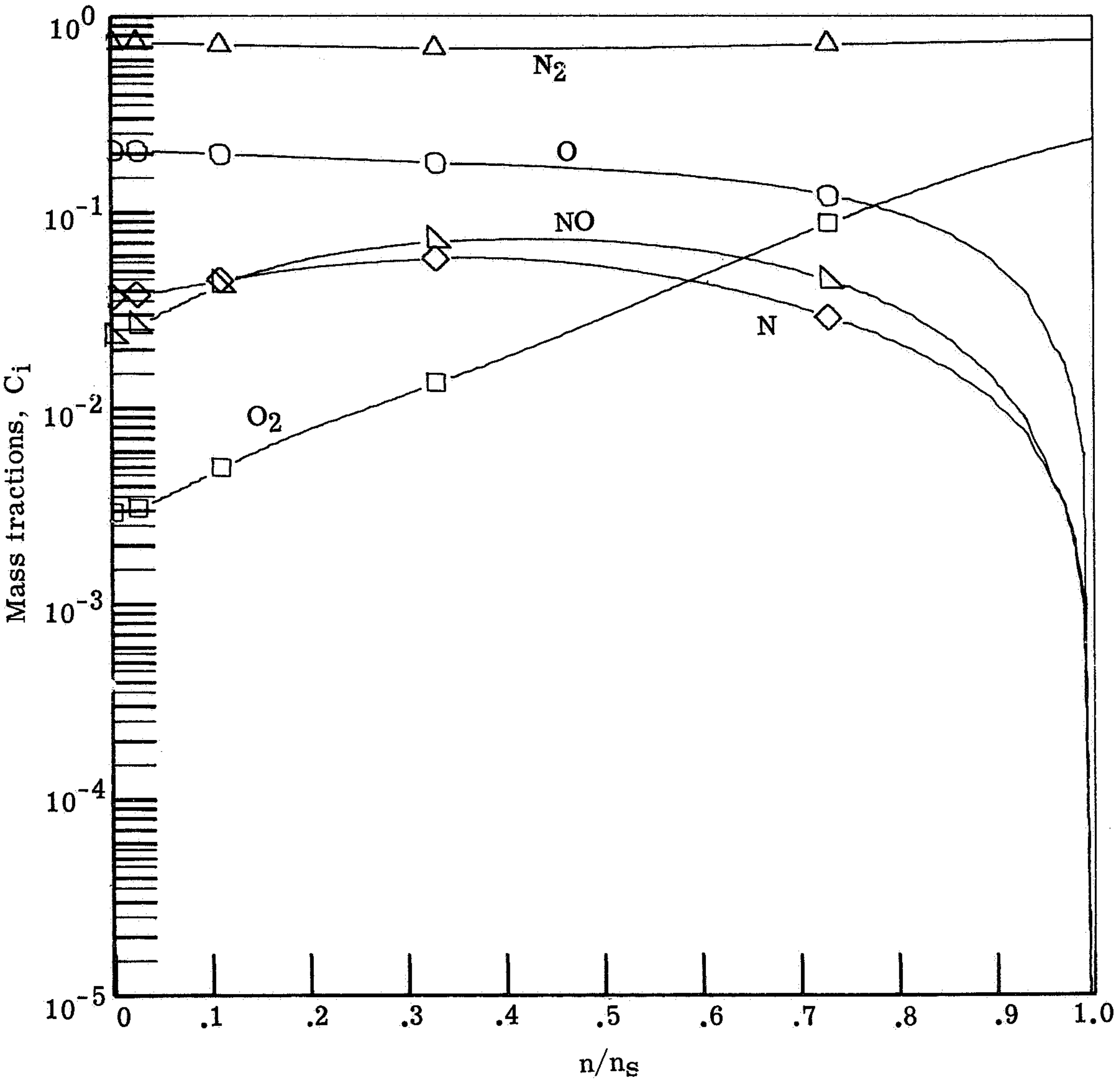

(a) $\xi = 0.0$.

Figure 14.- Species profiles for nonequilibrium air with multicomponent diffusion and no mass injection at an altitude of 60.96 km. $U_\infty^* = 6.10$ km/s; $T_w^* = 1500$ K; $a^* = 2.54$ cm; noncatalytic wall.

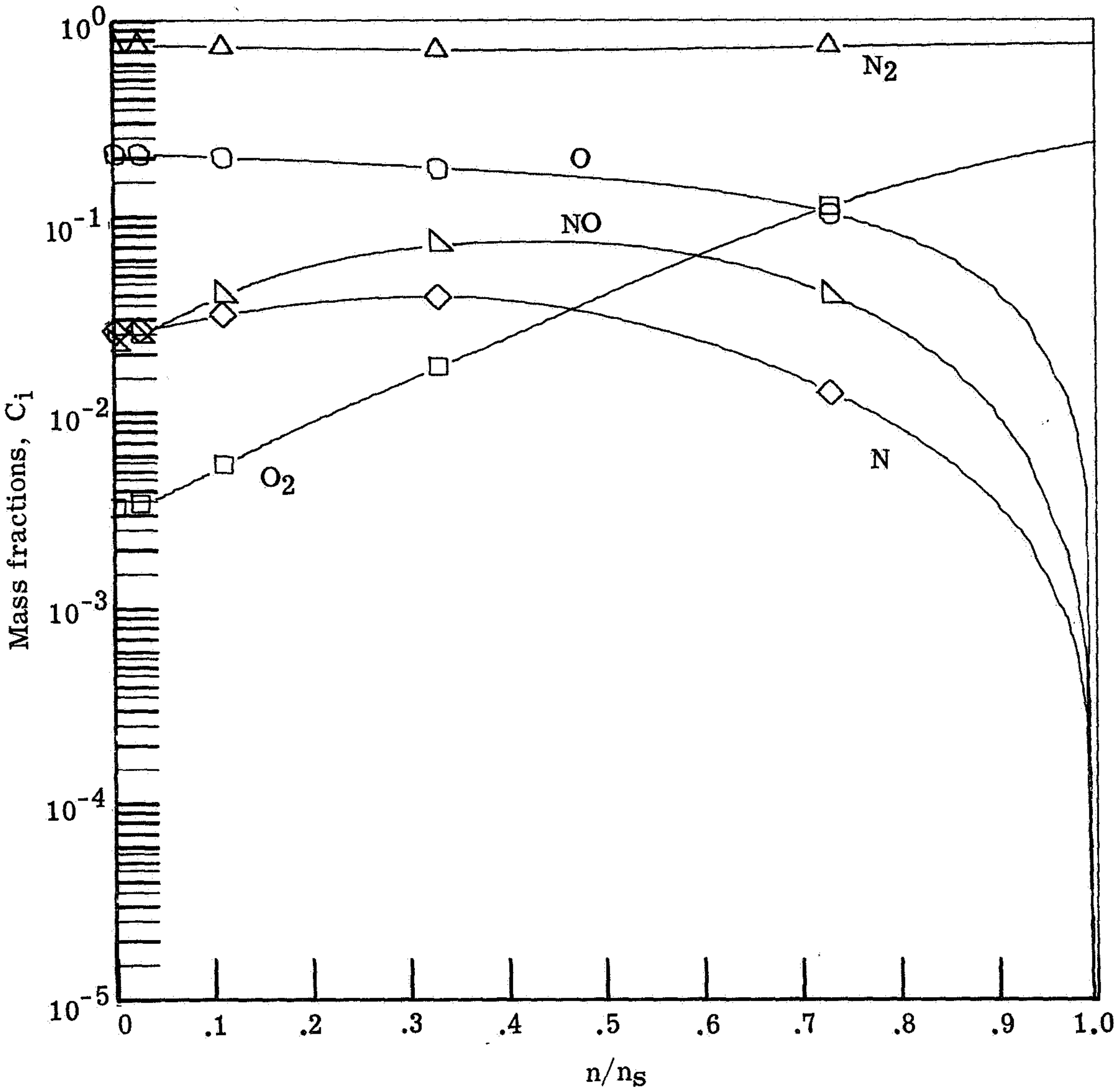

(b) $\xi = 1.0$.

Figure 14.- Continued.

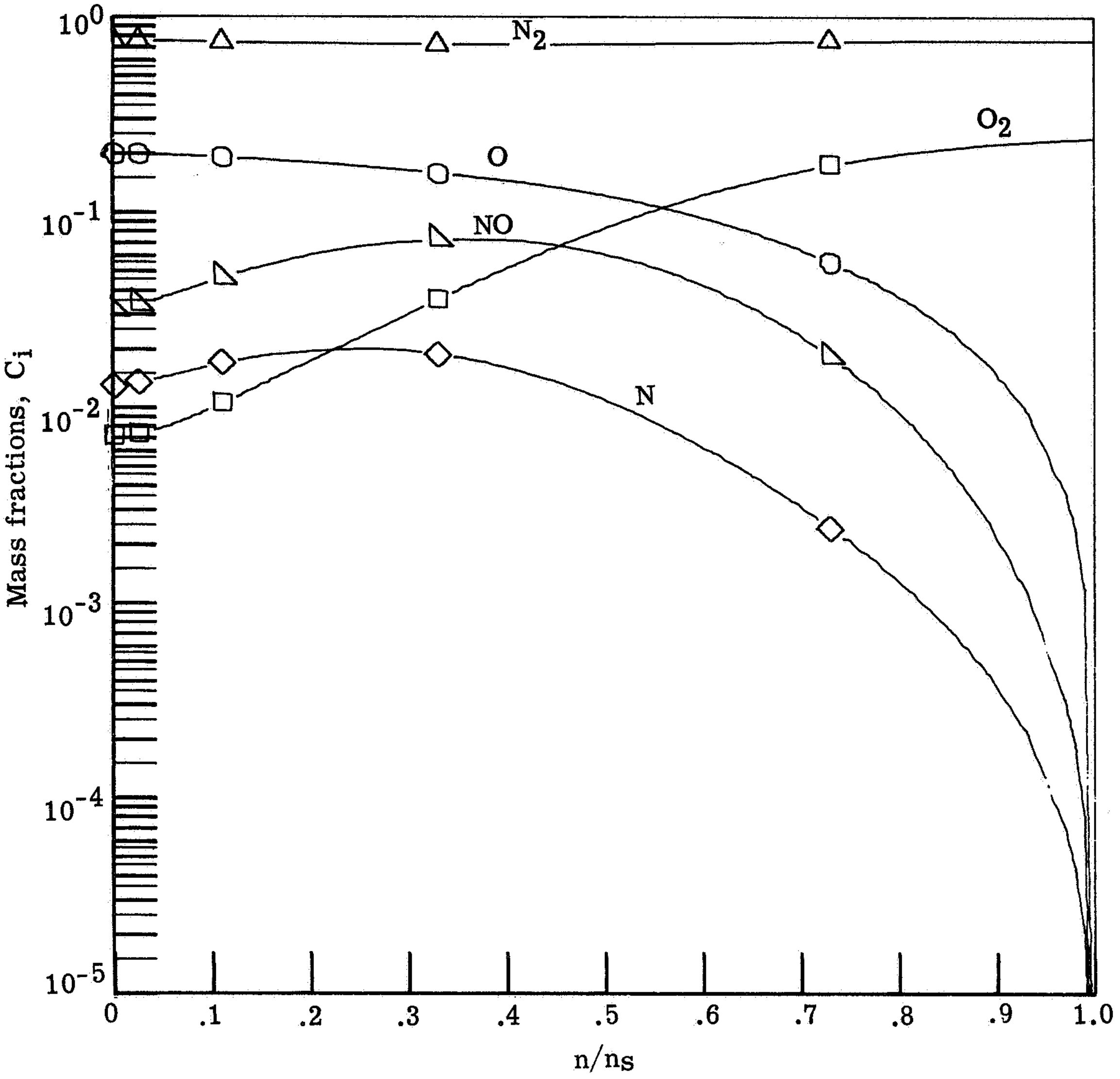

(c) $\xi = 2.0$.

Figure 14.- Continued.

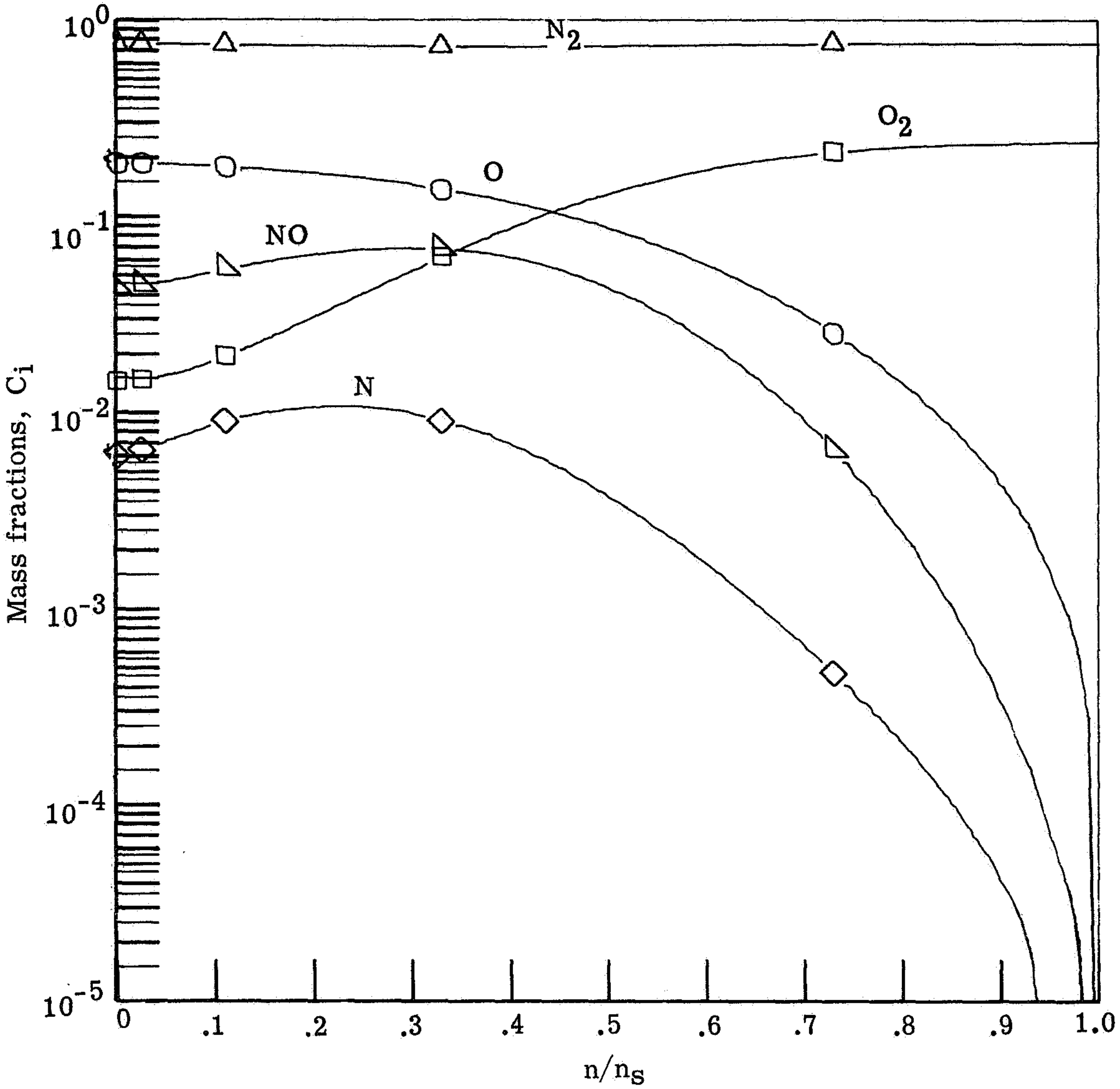

(d) $\xi = 3.0$.

Figure 14.- Concluded.

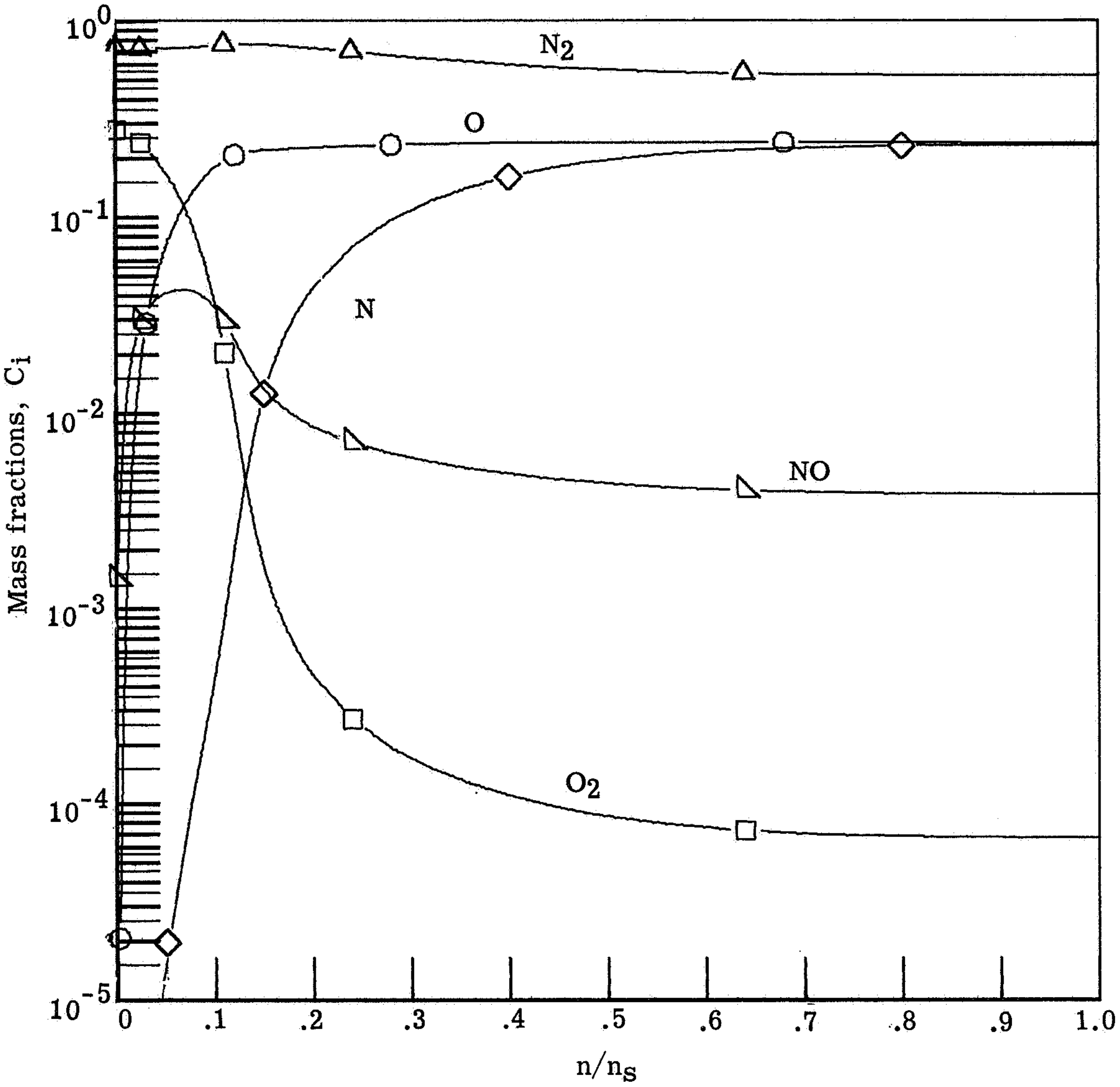

(a) $\xi = 0.0$.

Figure 15.- Species profiles for equilibrium air with multicomponent diffusion and no mass injection at an altitude of 60.96 km. $U_\infty^* = 6.10$ km/s; $T_w^* = 1500$ K; $a^* = 2.54$ cm.

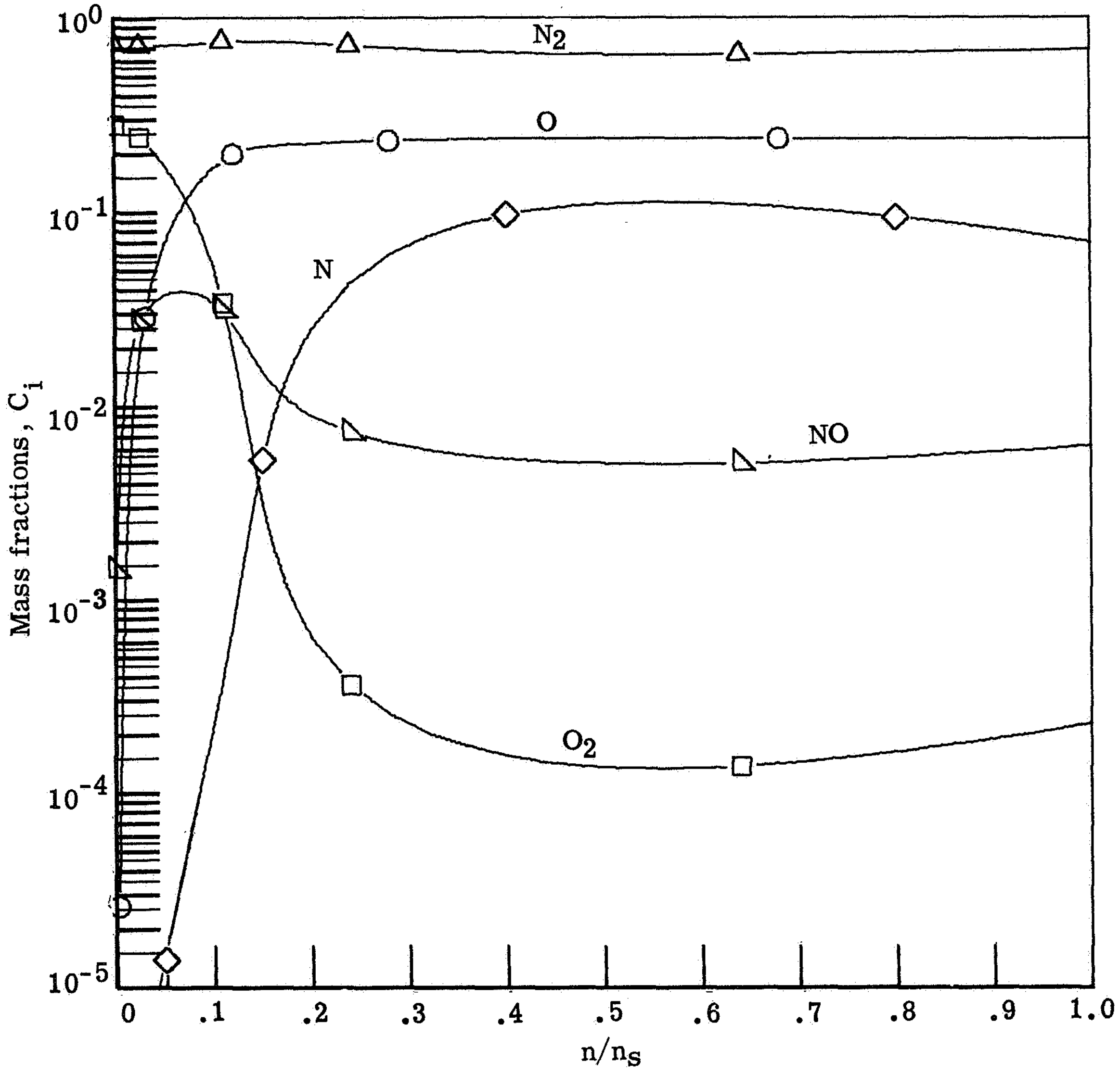

(b) $\xi = 1.0$.

Figure 15.- Continued.

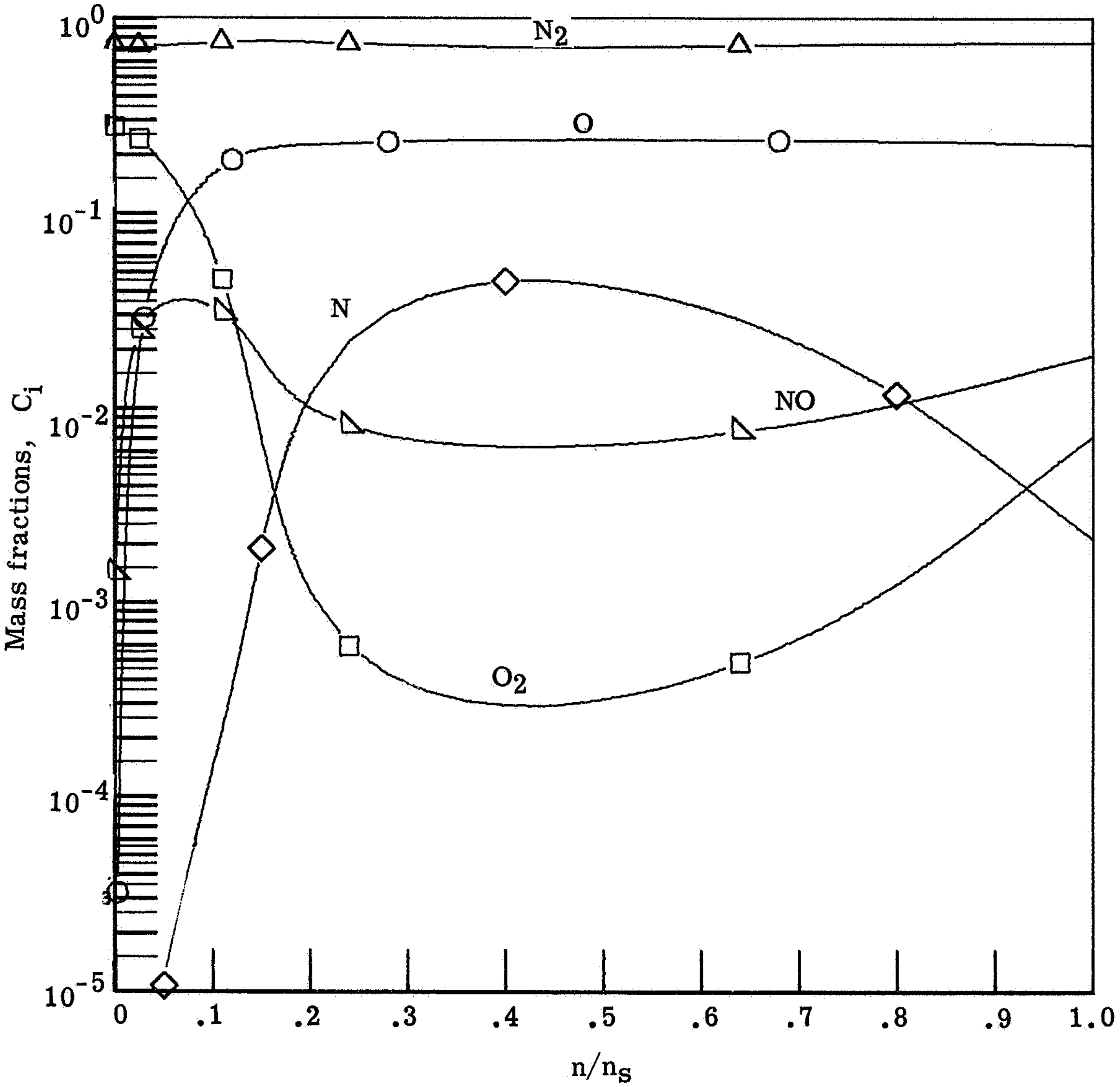

(c) $\xi = 2.0$.

Figure 15.- Continued.

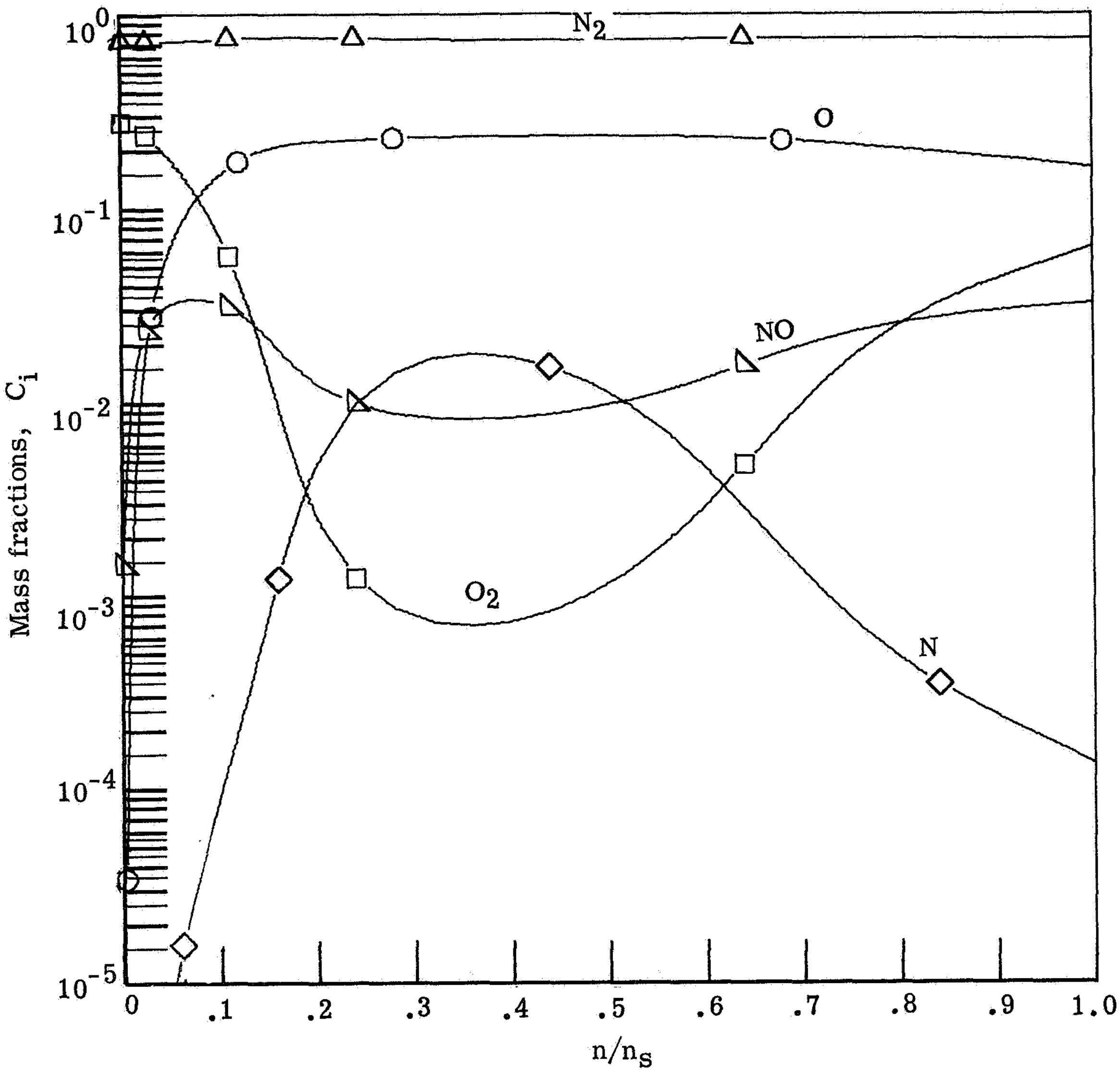

(d) $\xi = 3.0$.

Figure 15.- Concluded.

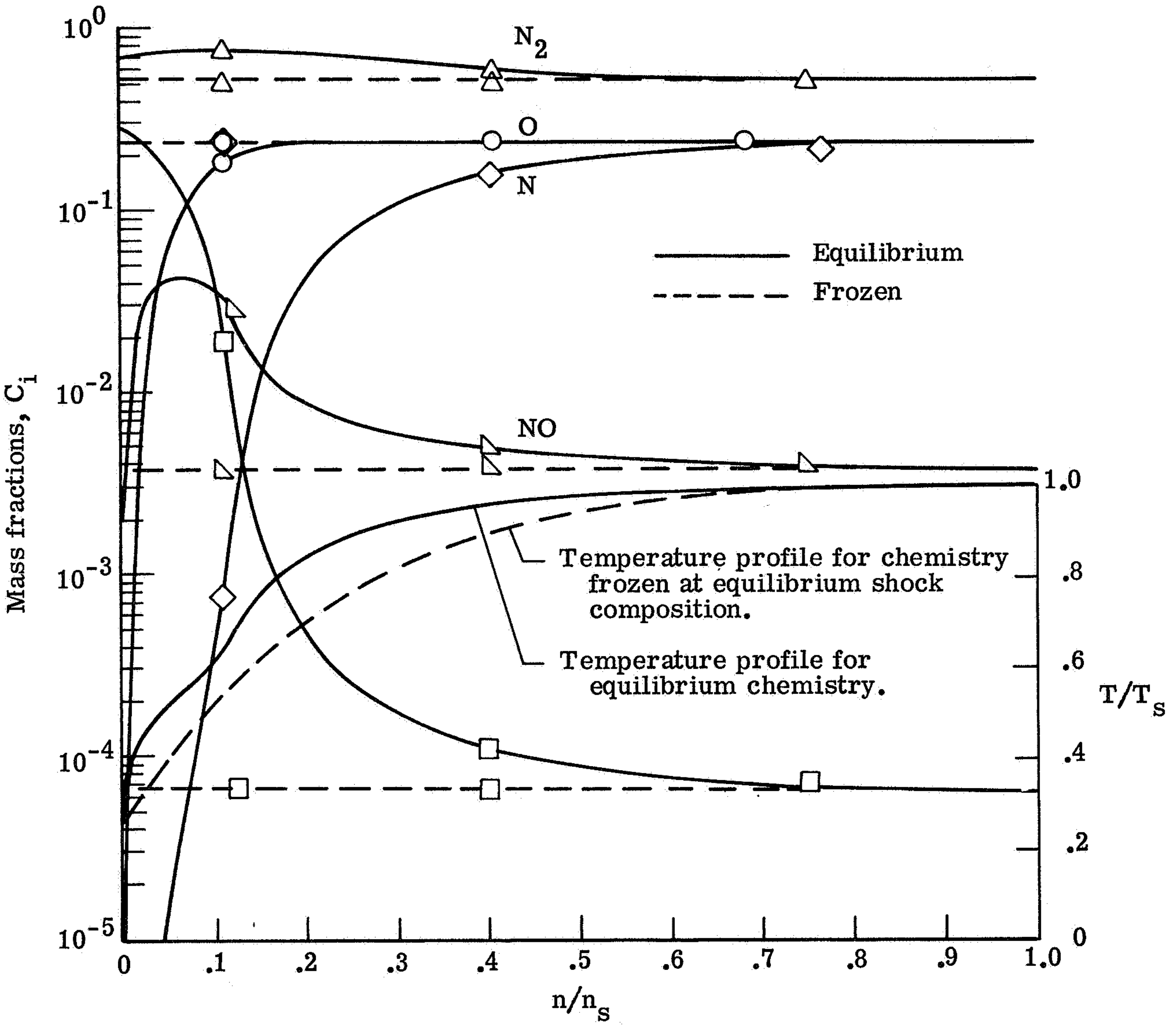

Figure 16.- Stagnation equilibrium and frozen air species and temperature profiles at an altitude of 60.96 km. $U_\infty^* = 6.10$ km/s; $T_W^* = 1500$ K; $a^* = 2.54$ cm.

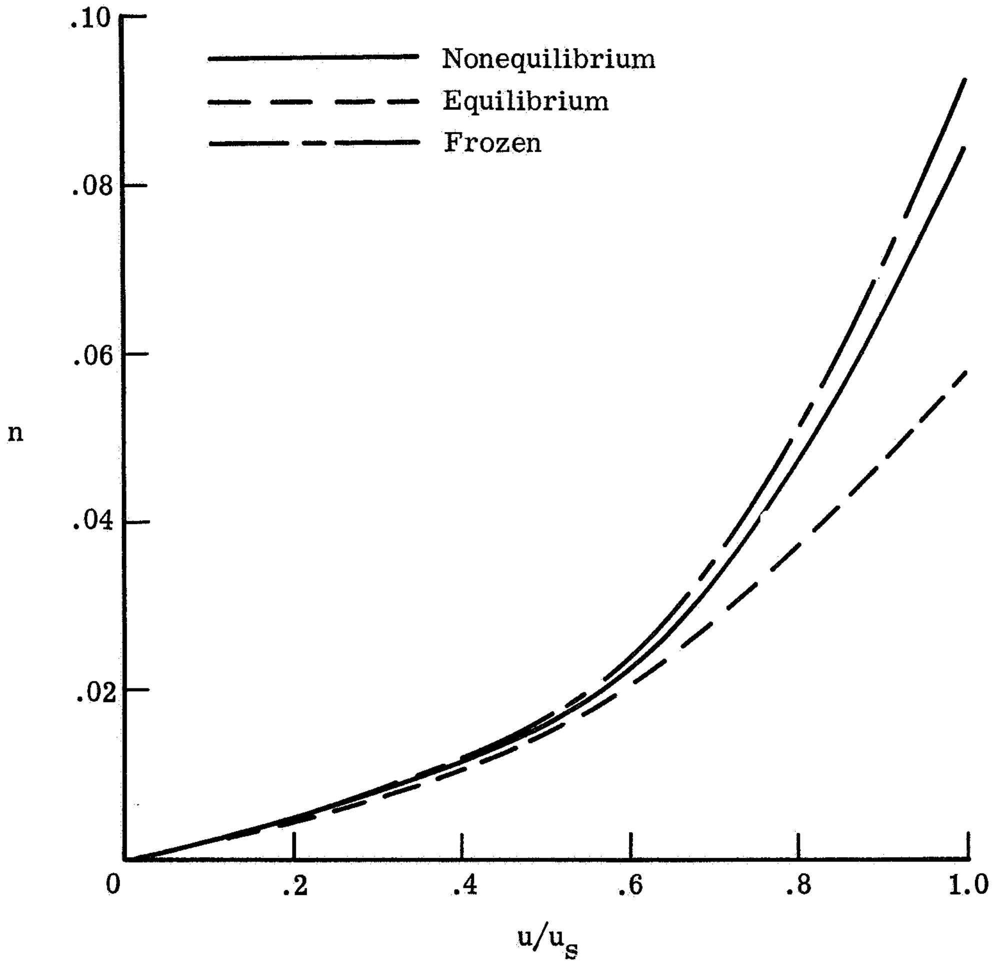

(a) $\xi = 0.0$.

Figure 17.- Effect of chemistry model on tangential velocity profiles with multicomponent diffusion and no mass injection at an altitude of 60.96 km. $U_\infty^* = 6.10$ km/s; $T_w^* = 1500$ K; $a^* = 2.54$ cm; noncatalytic wall.

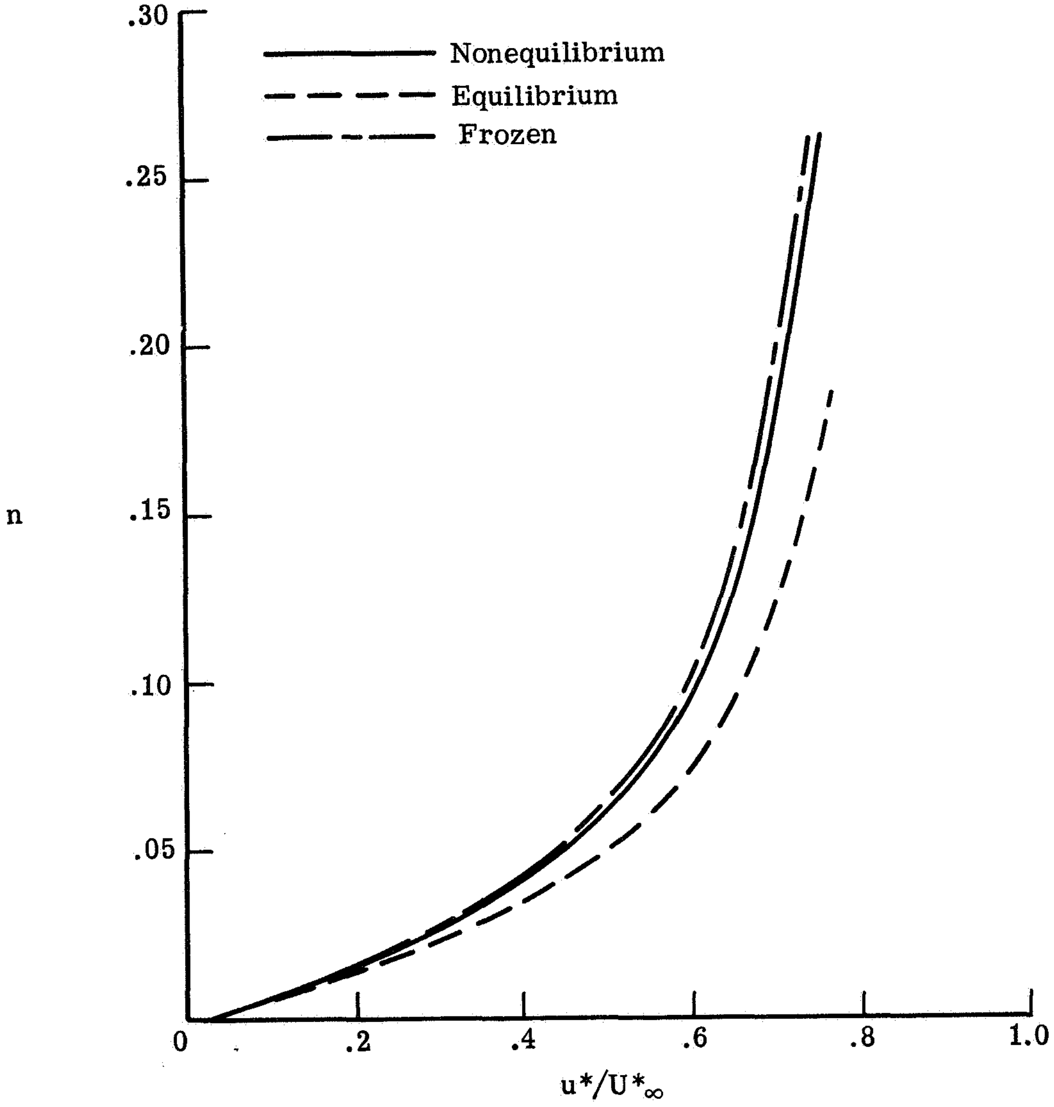

(b) $\xi = 2.0$.

Figure 17.- Concluded.

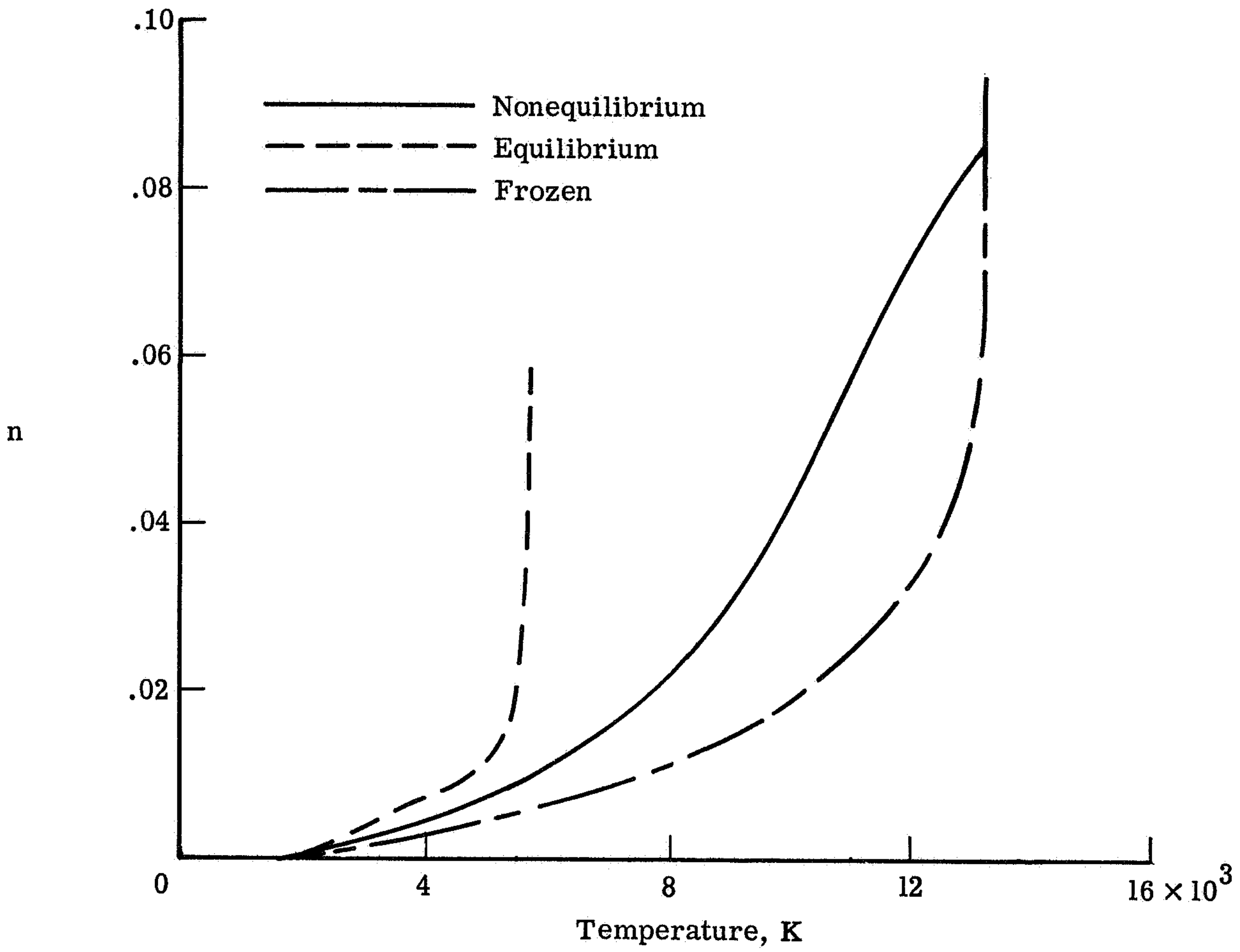

(a) $\xi = 0.0$.

Figure 18.- Effect of chemistry model on temperature profiles with multicomponent diffusion and no mass injection at an altitude of 60.96 km. $U_\infty^* = 6.10$ km/s; $T_w^* = 1500$ K; $a^* = 2.54$ cm; noncatalytic wall.

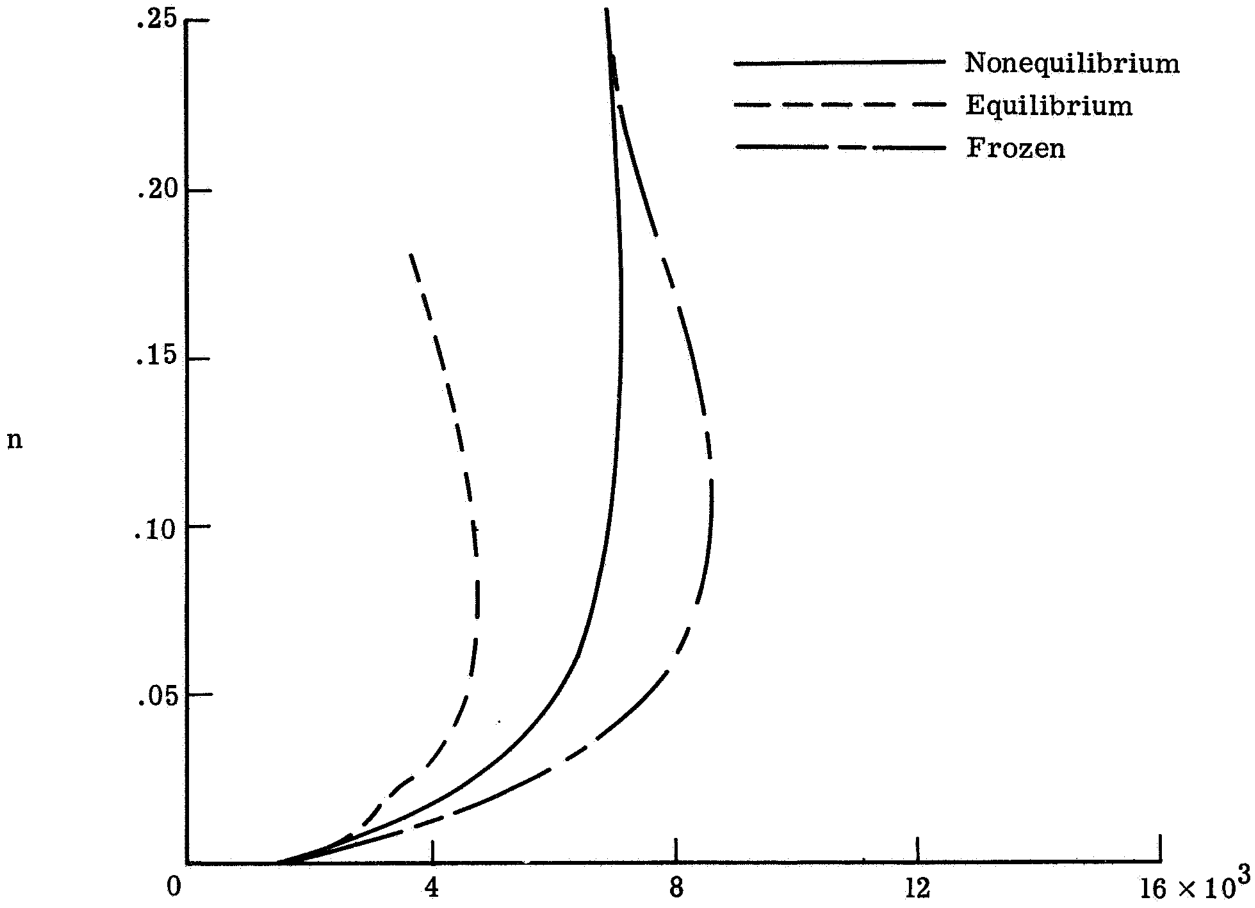

Temperature, K

(b) $\xi = 2.0$.

Figure 18.- Concluded.

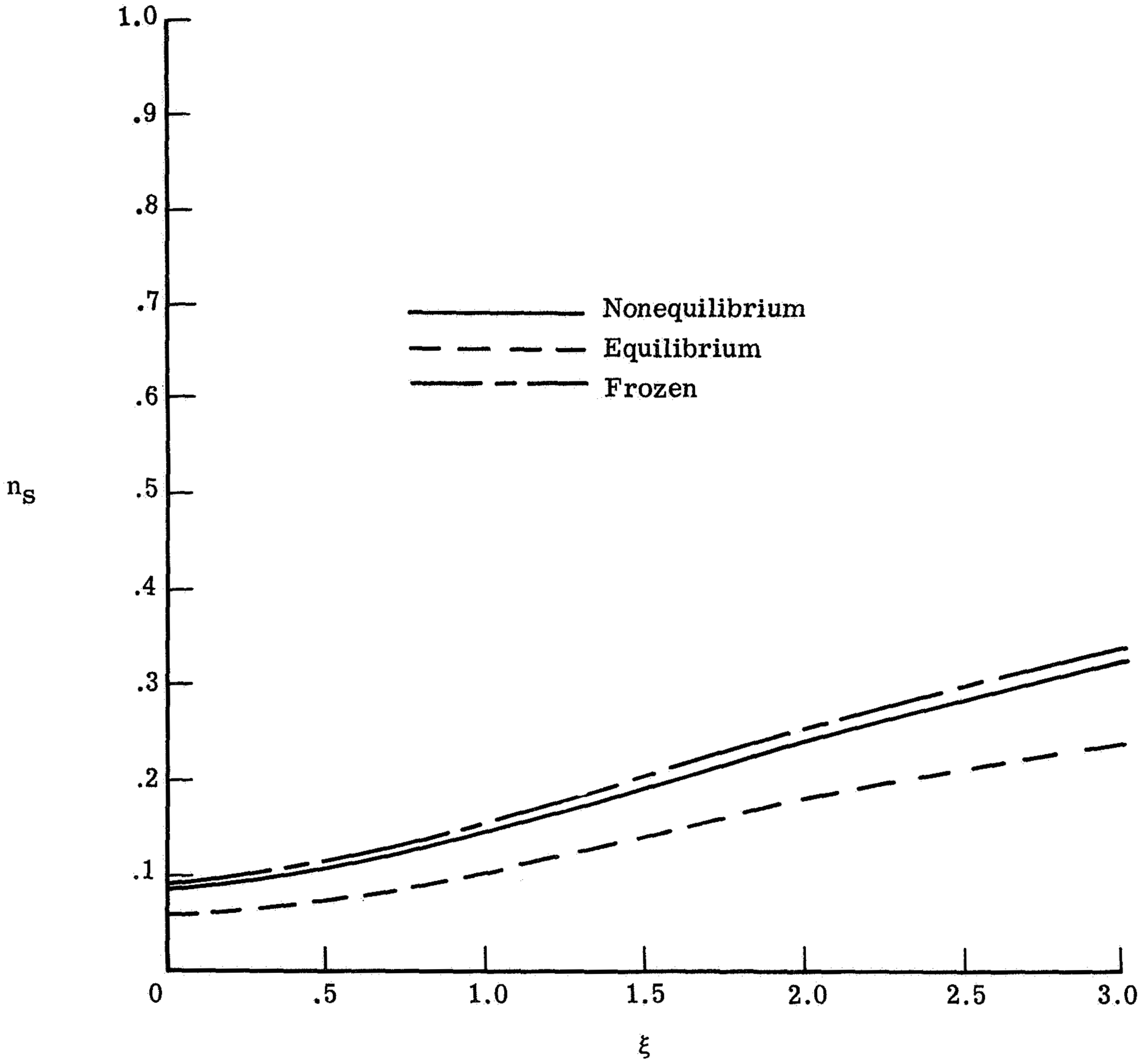

Figure 19.- Effect of chemistry model on shock standoff distance with multicomponent diffusion and no mass injection at an altitude of 60.96 km. $U_\infty^* = 6.10$ km/s; $T_w^* = 1500$ K; $a^* = 2.54$ cm; noncatalytic wall.

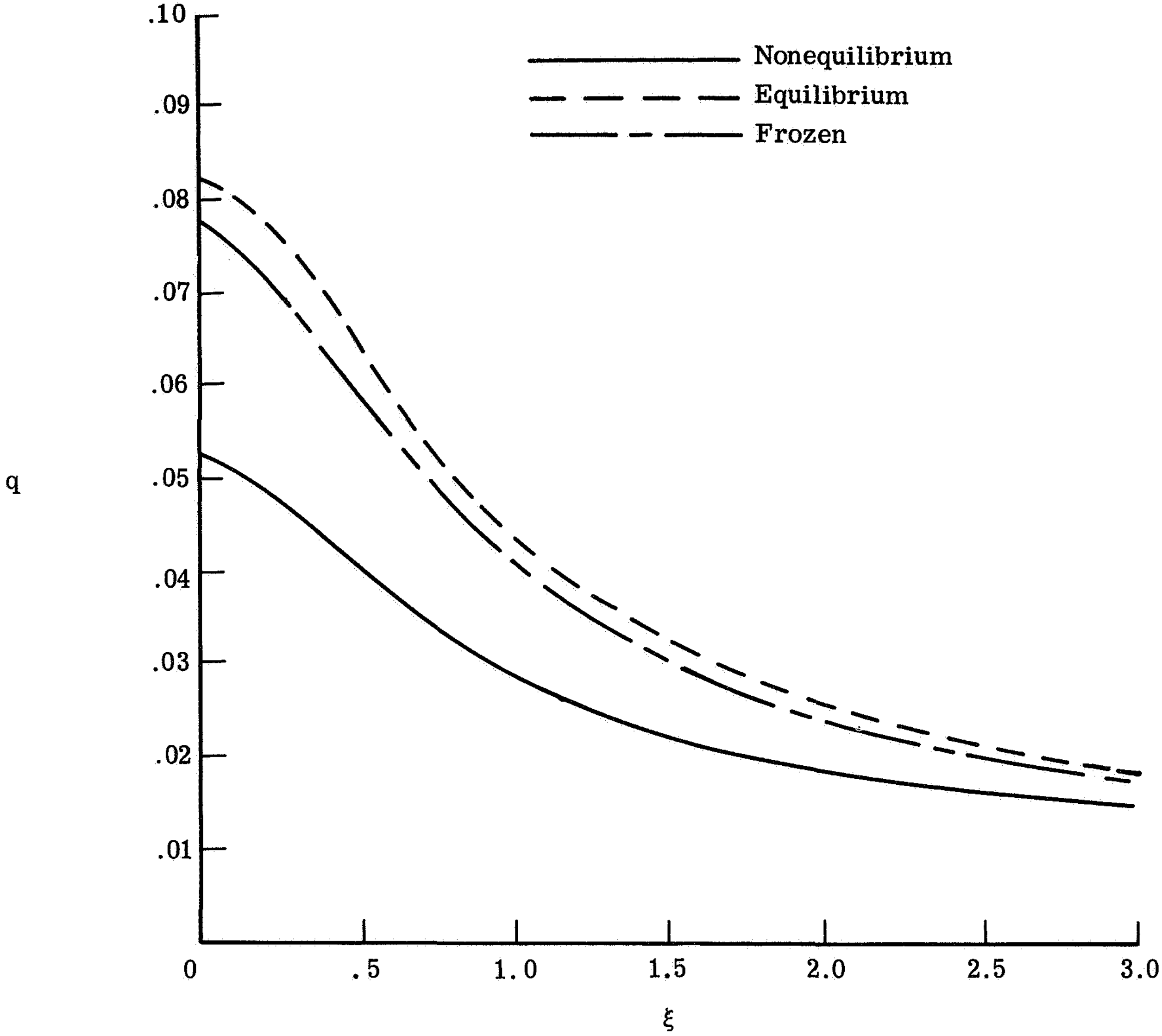

Figure 20.- Effect of chemistry model on nondimensional heat transfer with multicomponent diffusion and no mass injection at an altitude of 60.96 km. $U_\infty^* = 6.10$ km/s; $T_w^* = 1500$ K; $a^* = 2.54$ cm; noncatalytic wall.

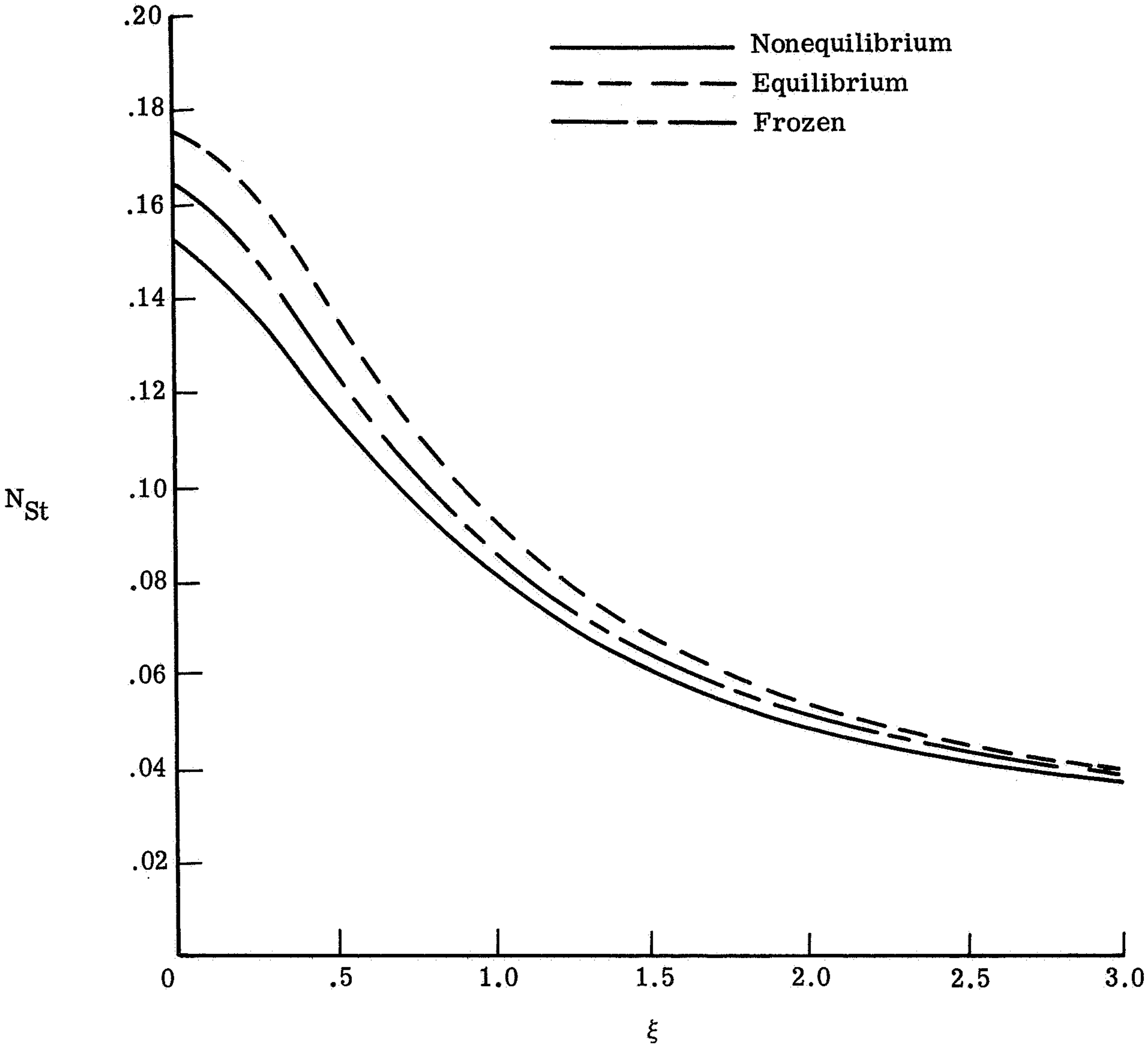

Figure 21.- Effect of chemistry model on Stanton number with multicomponent diffusion and no mass injection at an altitude of 60.96 km. $U_\infty^* = 6.10$ km/s; $T_w^* = 1500$ K; $a^* = 2.54$ cm; noncatalytic wall.

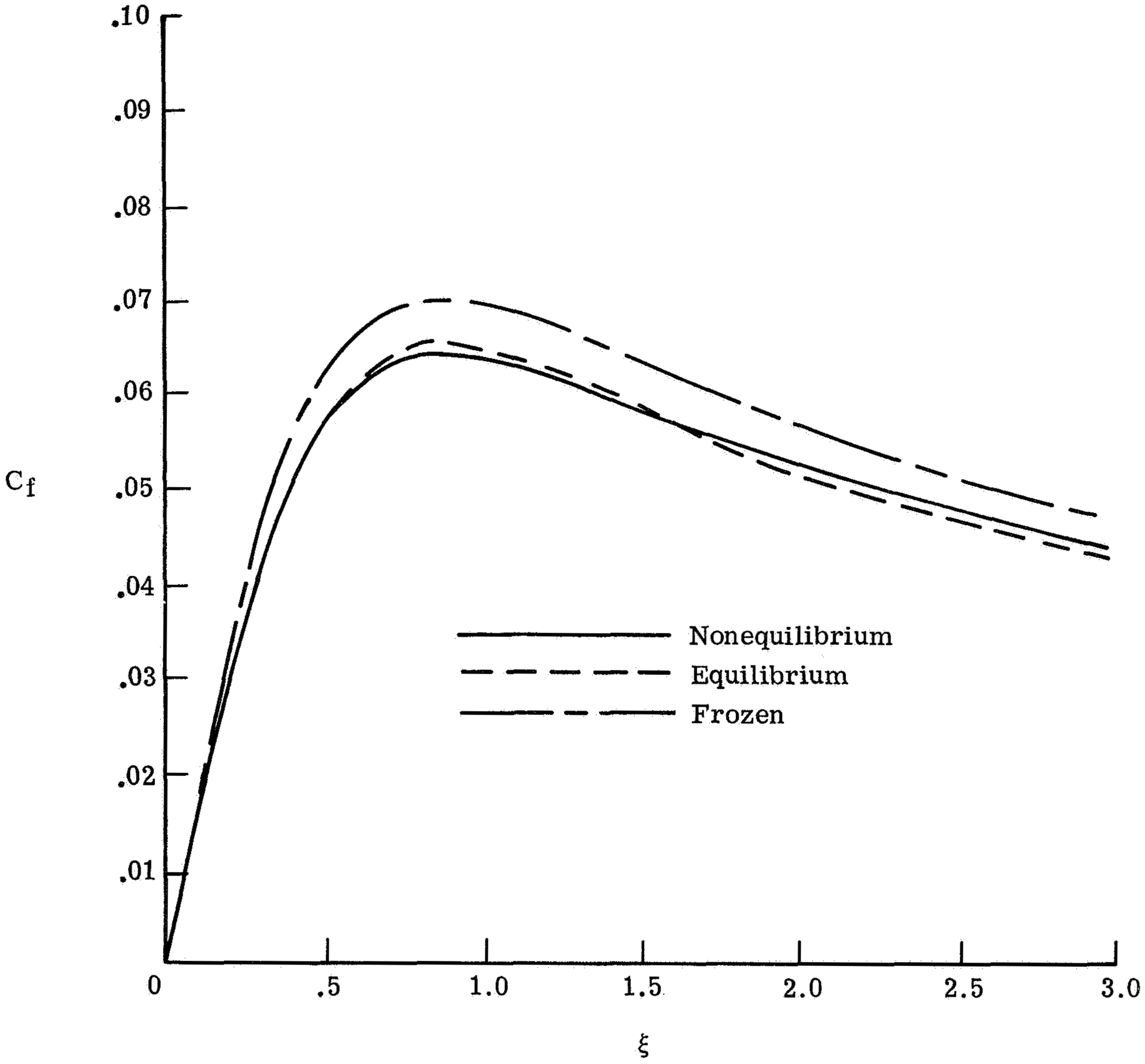

Figure 22.- Effect of chemistry model on skin-friction coefficient with multicomponent diffusion and no mass injection at an altitude of 60.96 km. $U_\infty^* = 6.10$ km/s; $T_w^* = 1500$ K; $a^* = 2.54$ cm; noncatalytic wall.

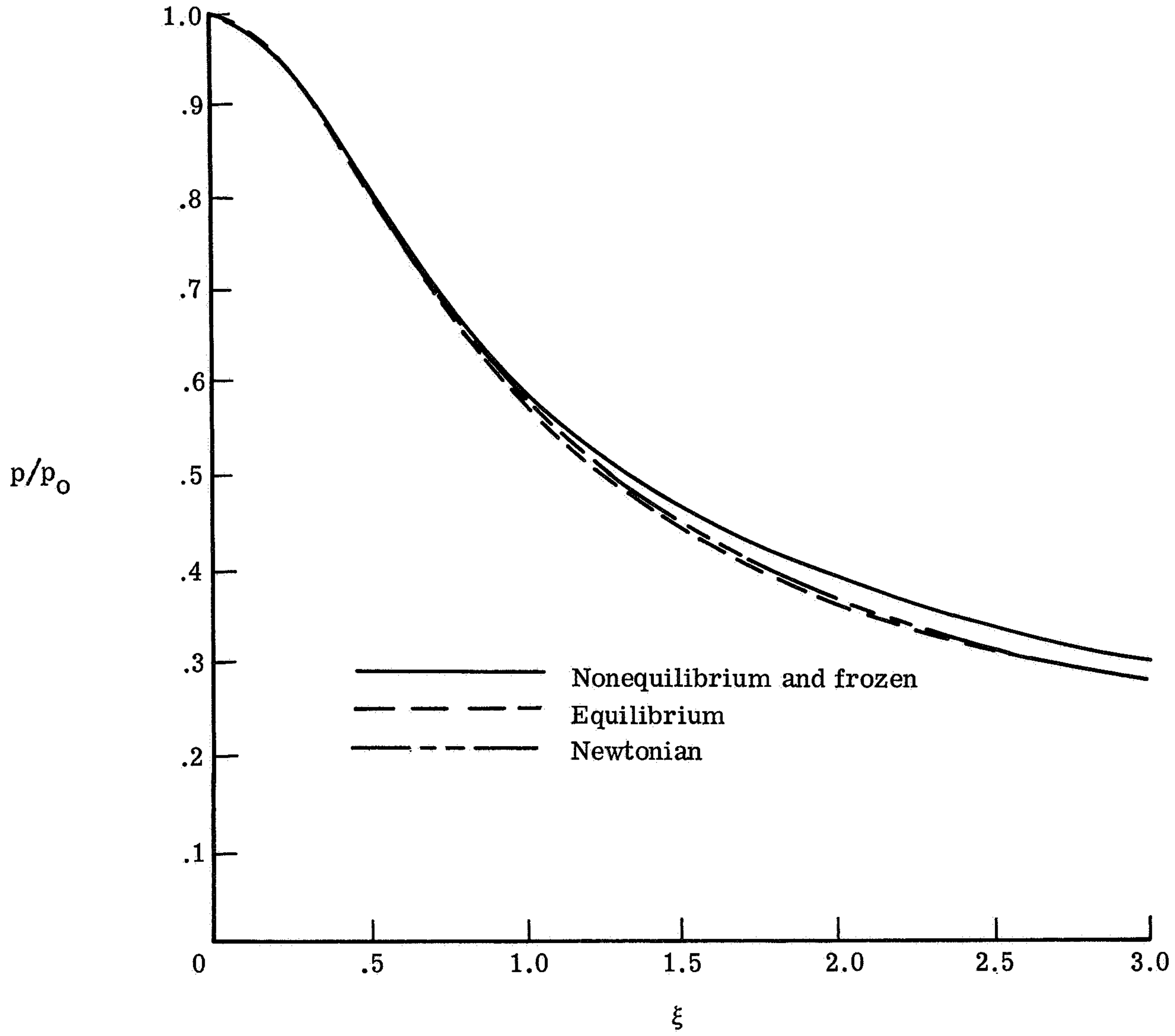

Figure 23.- Effect of chemistry model on wall pressure distribution with multicomponent diffusion and no mass injection at an altitude of 60.96 km. $U_\infty^* = 6.10$ km/s; $T_w^* = 1500$ K; $a^* = 2.54$ cm; noncatalytic wall.

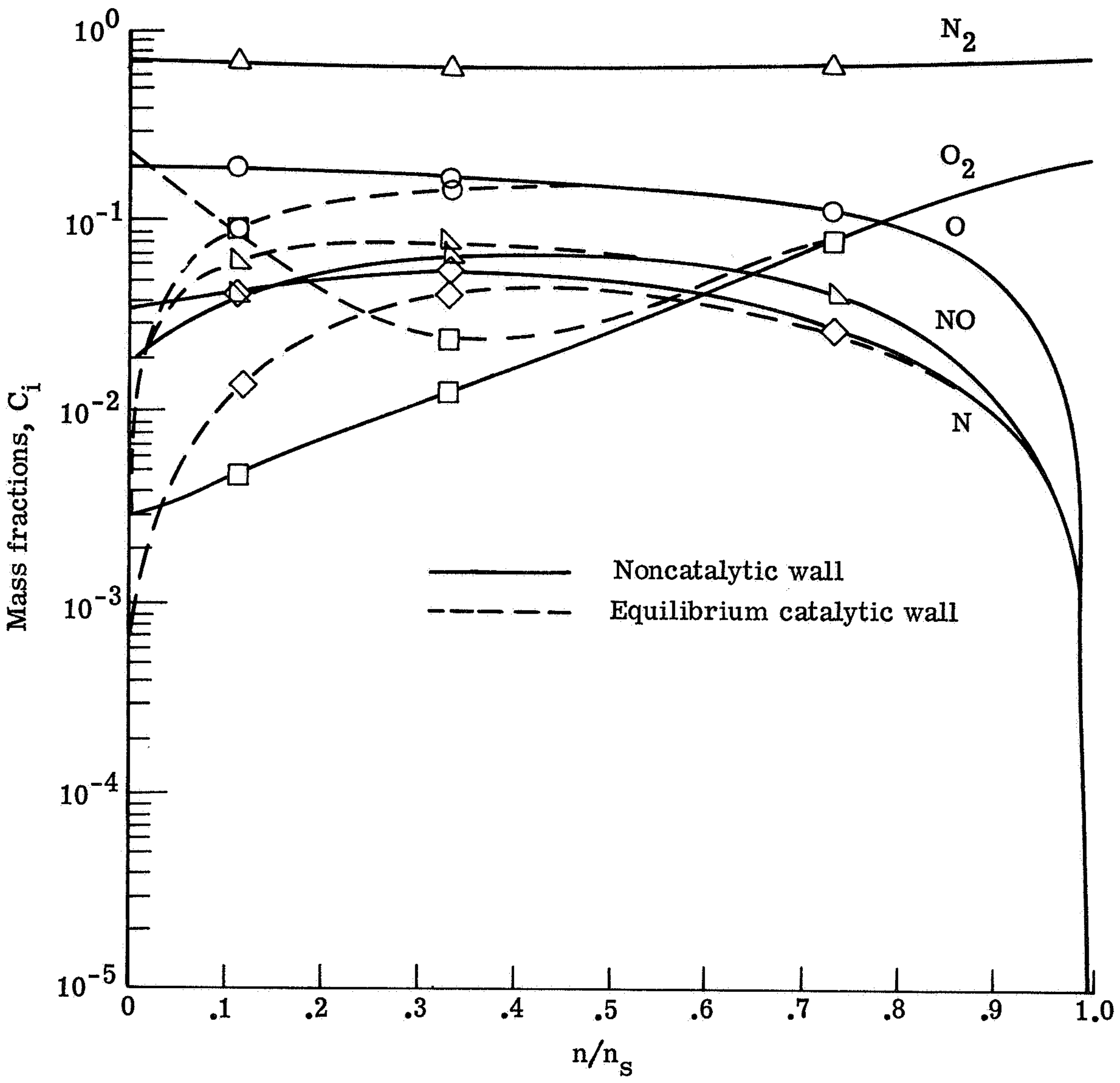

(a) $\xi = 0.0$.

Figure 24.- Effect of wall catalyticity on species profiles at an altitude of 60.96 km. $U_\infty^* = 6.10$ km/s; $T_w^* = 1500$ K; $a^* = 2.54$ cm; multicomponent diffusion.

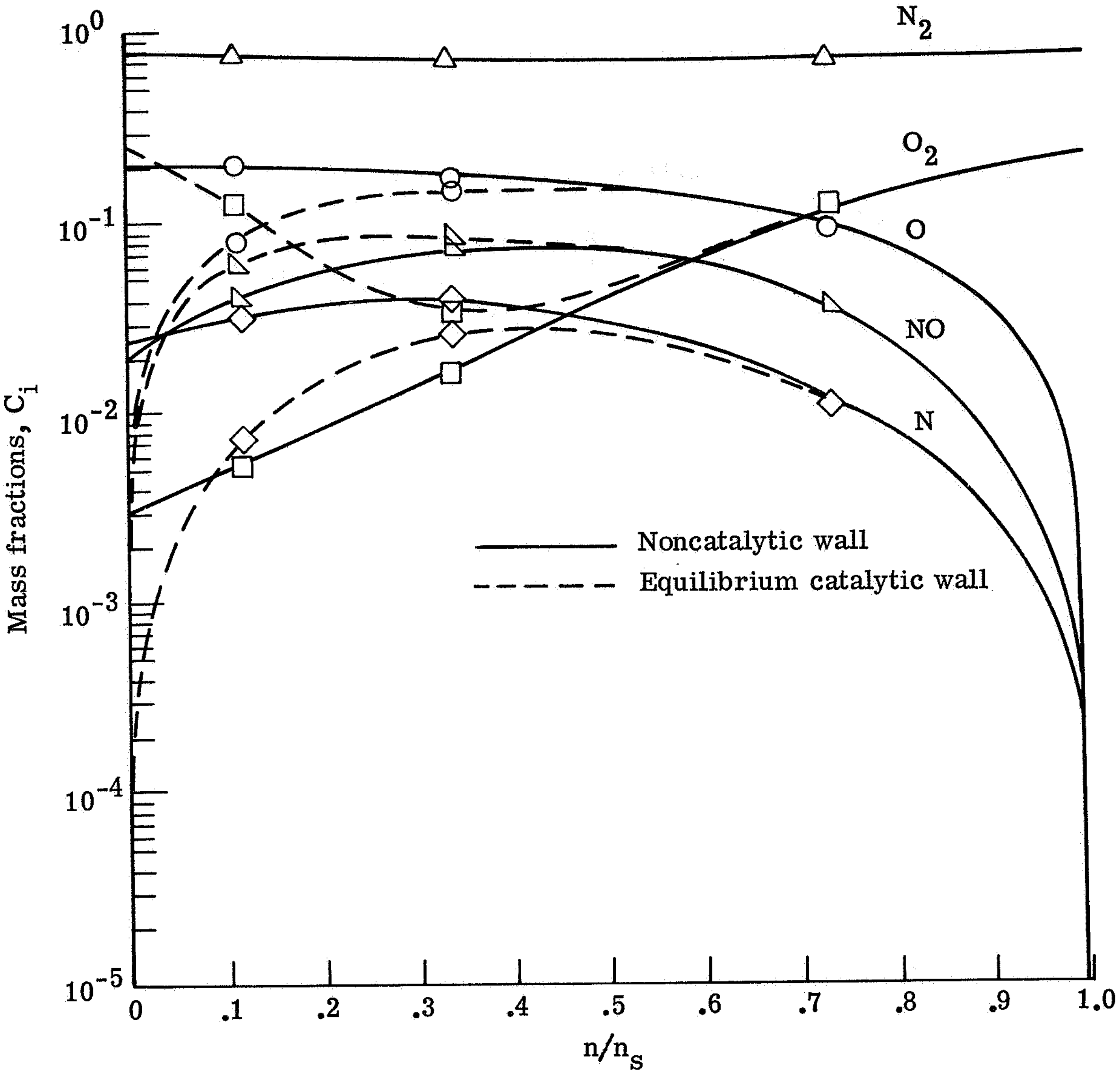

(b) $\xi = 1.0$.

Figure 24.- Continued.

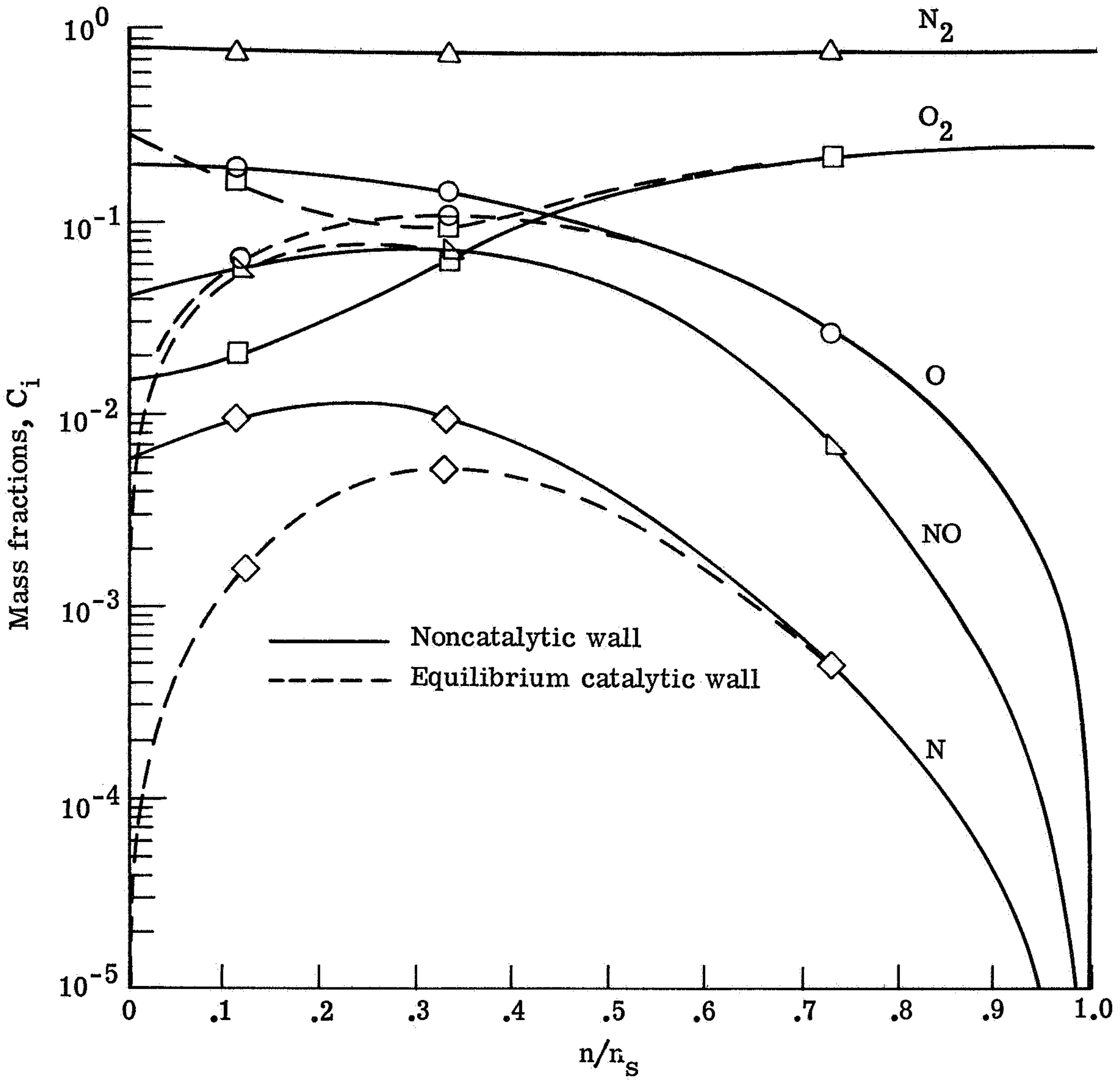

(c) $\xi = 3.0$.

Figure 24.- Concluded.

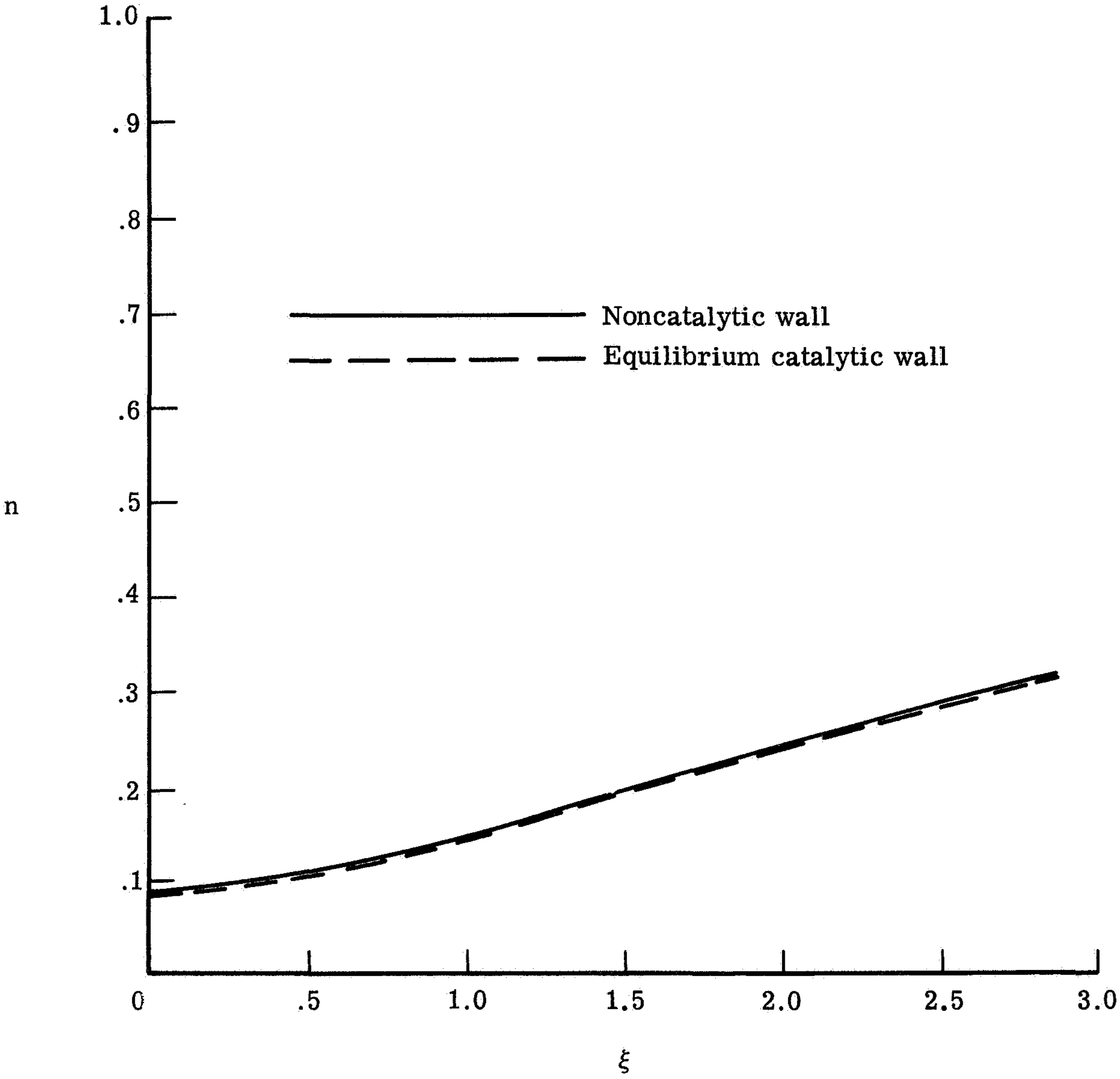

Figure 25.- Effect of wall catalyticity on shock standoff distance at an altitude of 60.96 km. $U_\infty^* = 6.10$ km/s; $T_w^* = 1500$ K; $a^* = 2.54$ cm; multicomponent diffusion.

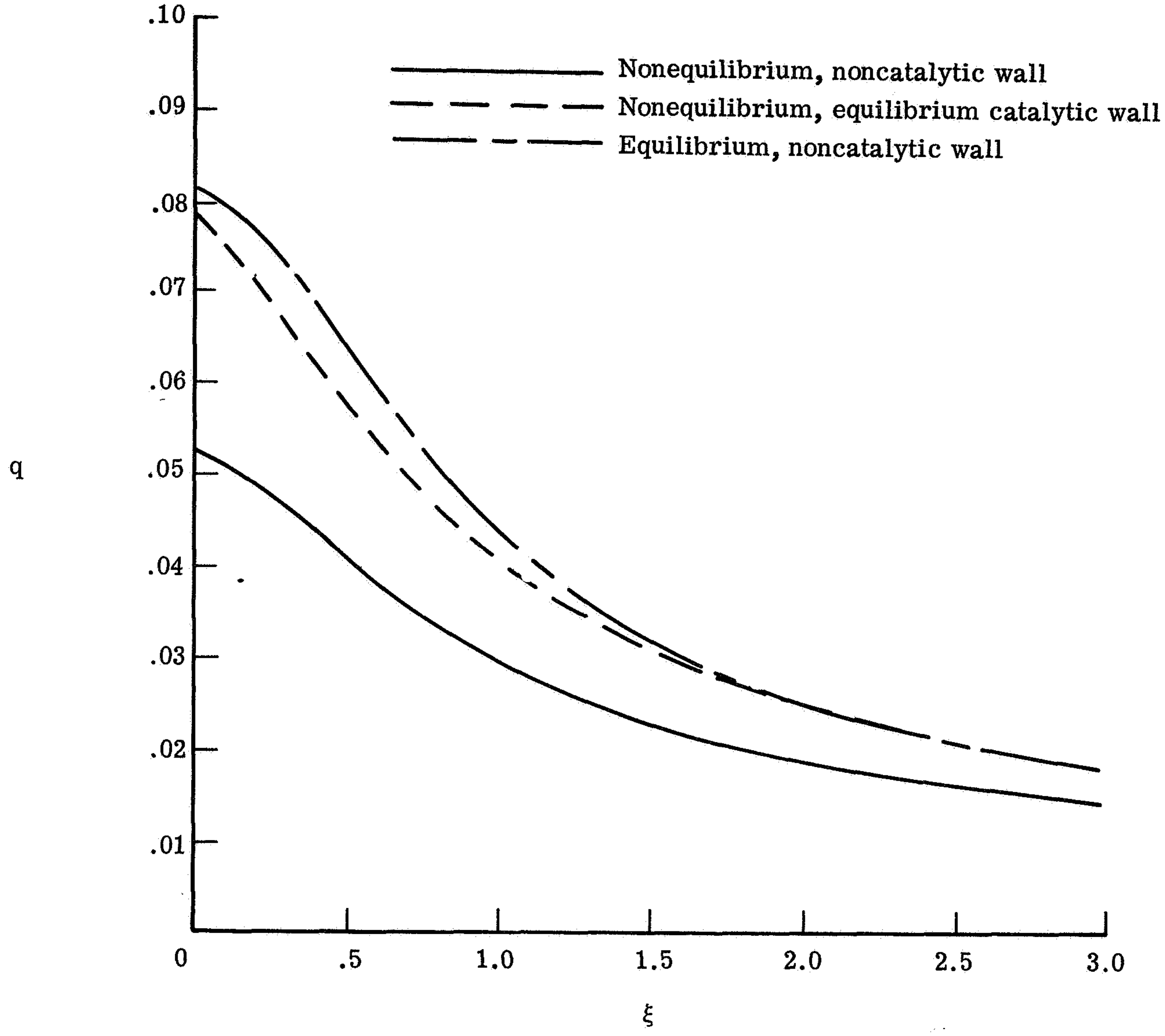

Figure 26.- Effect of wall catalyticity on nondimensional heat transfer at an altitude of 60.96 km. $U_\infty^* = 6.10$ km/s; $T_w^* = 1500$ K; $a^* = 2.54$ cm; multicomponent diffusion.

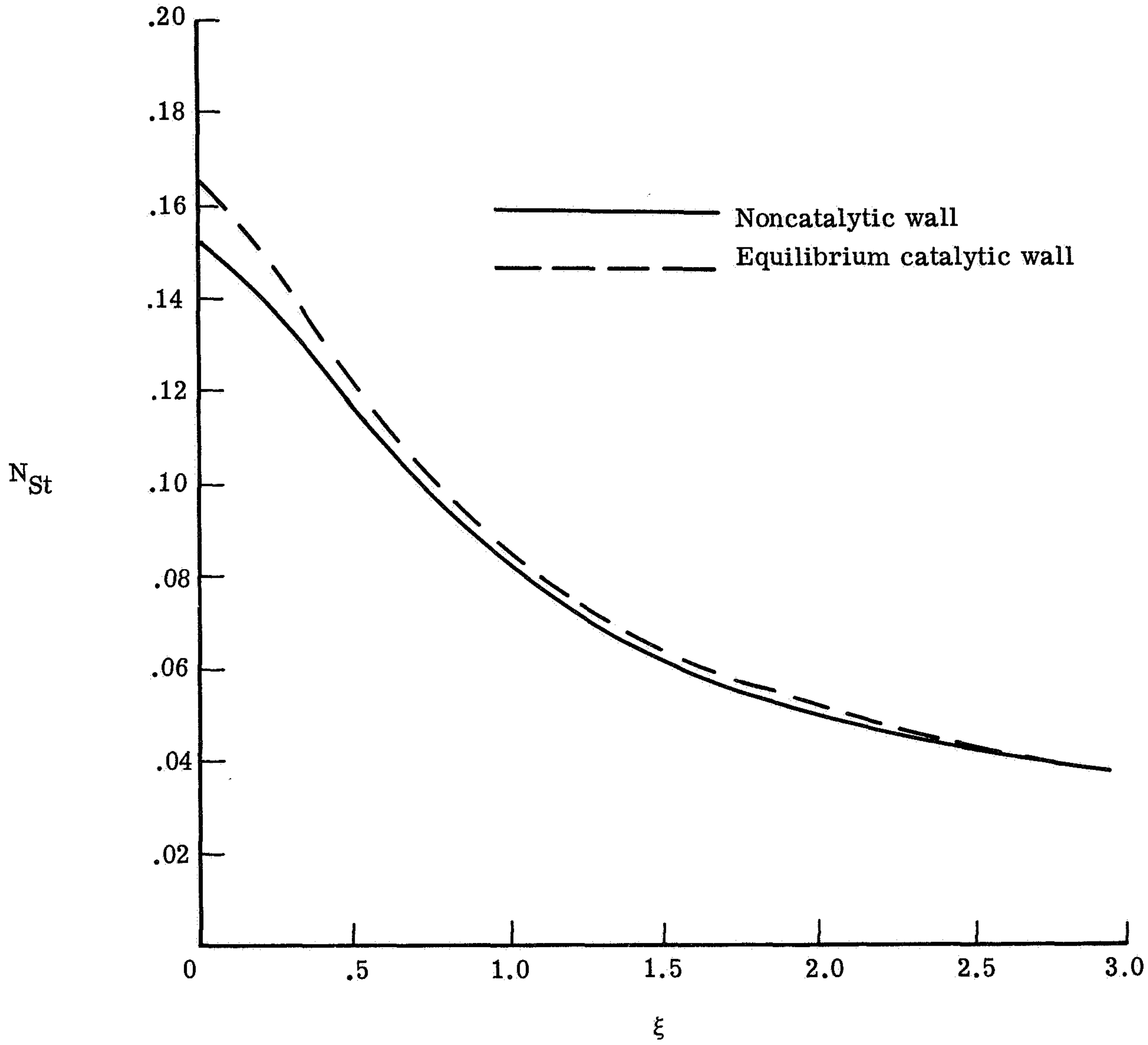

Figure 27.- Effect of wall catalyticity on Stanton number at an altitude of 60.96 km. $U_\infty^* = 6.10$ km/s; $T_w = 1500$ K; $a^* = 2.54$ cm; multicomponent diffusion.

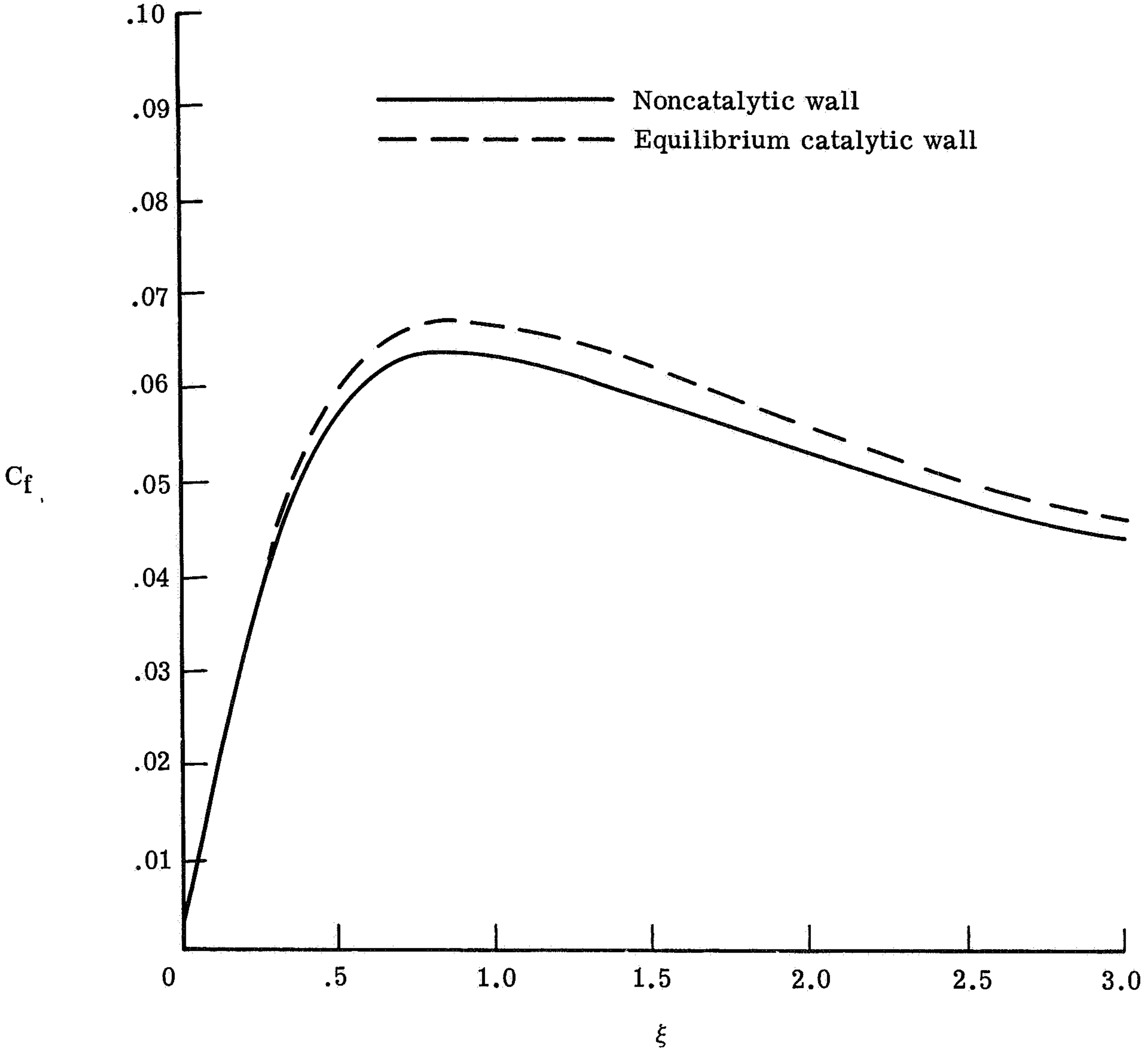

Figure 28.- Effect of wall catalyticity on skin-friction coefficient at an altitude of 60.96 km. $U_\infty^* = 6.10$ km/s; $T_w = 1500$ K; $a^* = 2.54$ cm; multicomponent diffusion.

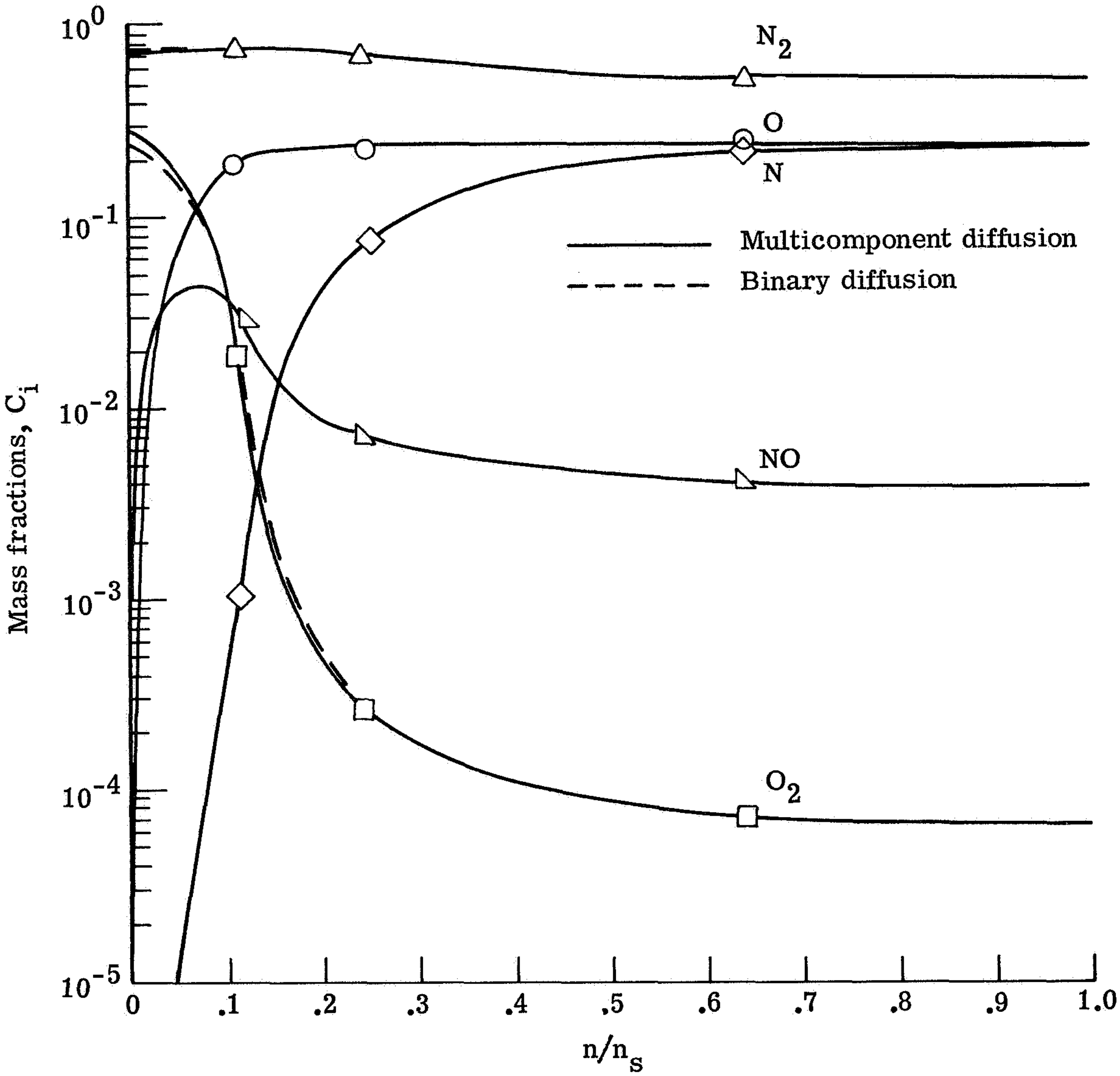

(a) $\xi = 0.0$.

Figure 29.- Effect of diffusion model on species profiles for equilibrium air at an altitude of 60.96 km. $U_\infty^* = 6.10$ km/s; $T_w^* = 1500$ K; $a^* = 2.54$ cm.

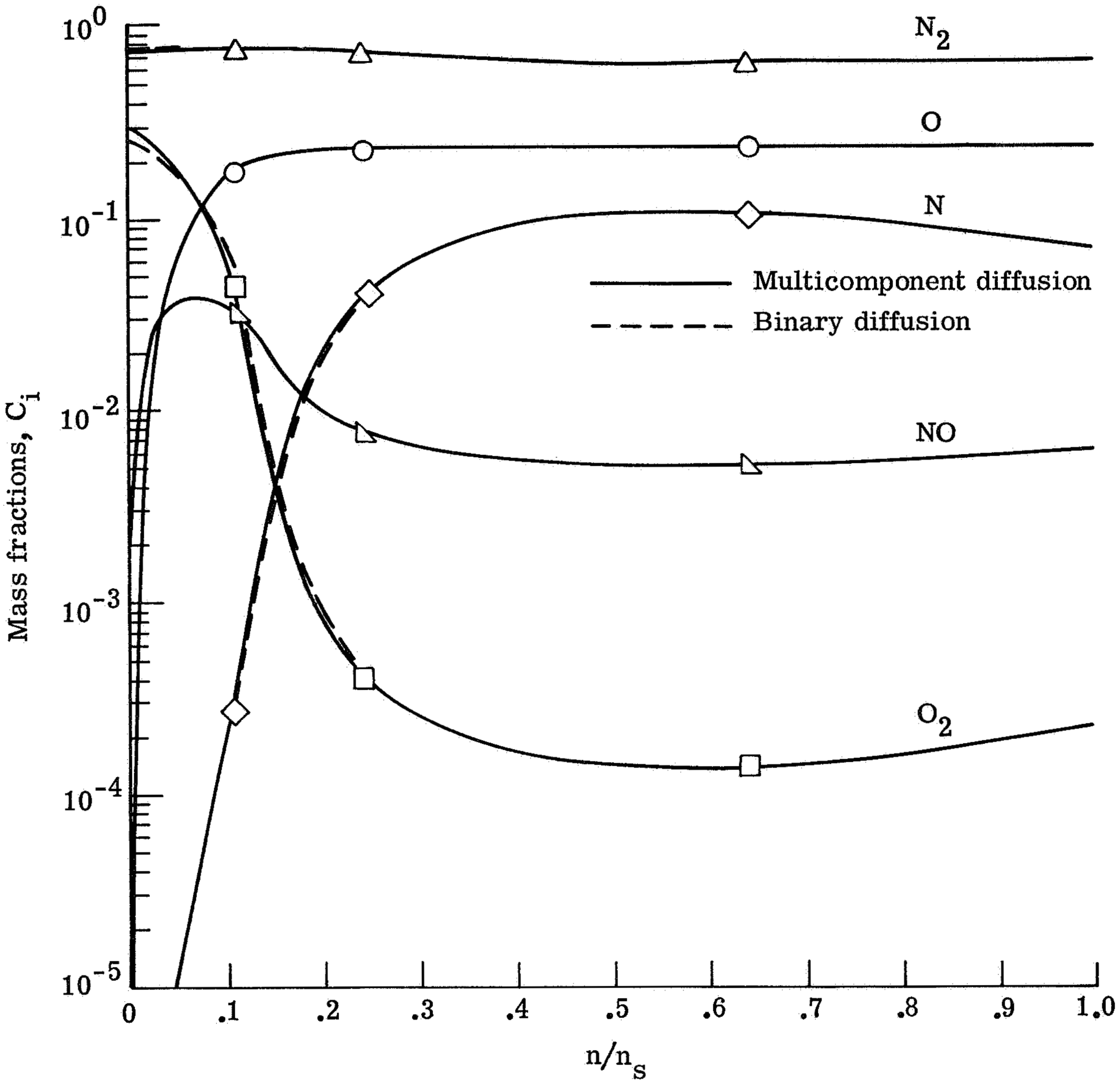

(b) $\xi = 1.0$.

Figure 29.- Concluded.

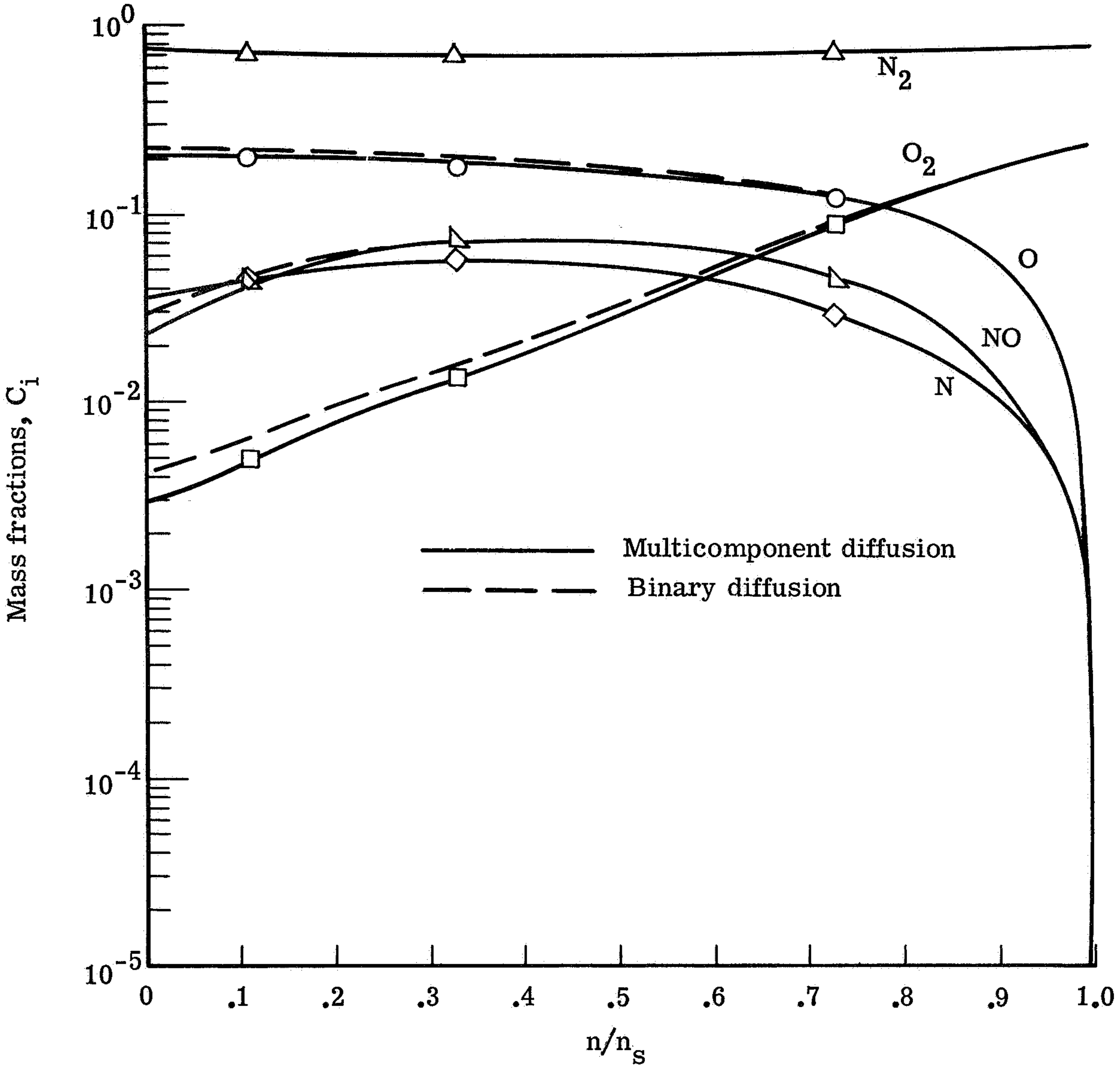

(a) $\xi = 0.0$.

Figure 30.- Effect of diffusion model on species profiles for nonequilibrium air at an altitude of 60.96 km. $U_\infty^* = 6.10$ km/s; $T_w^* = 1500$ K; $a^* = 2.54$ cm.

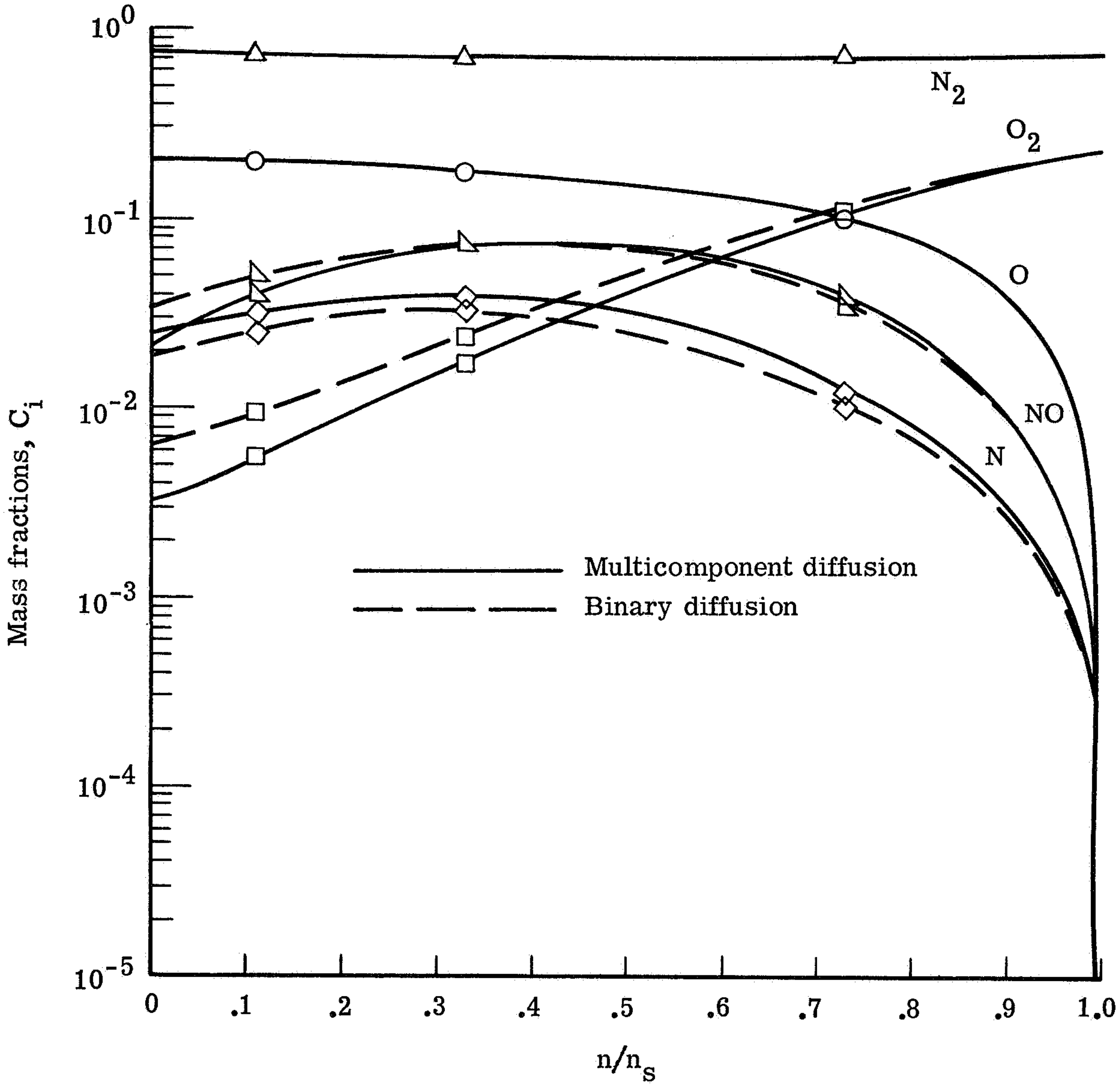

(b) $\xi = 1.0$.

Figure 30.- Concluded.

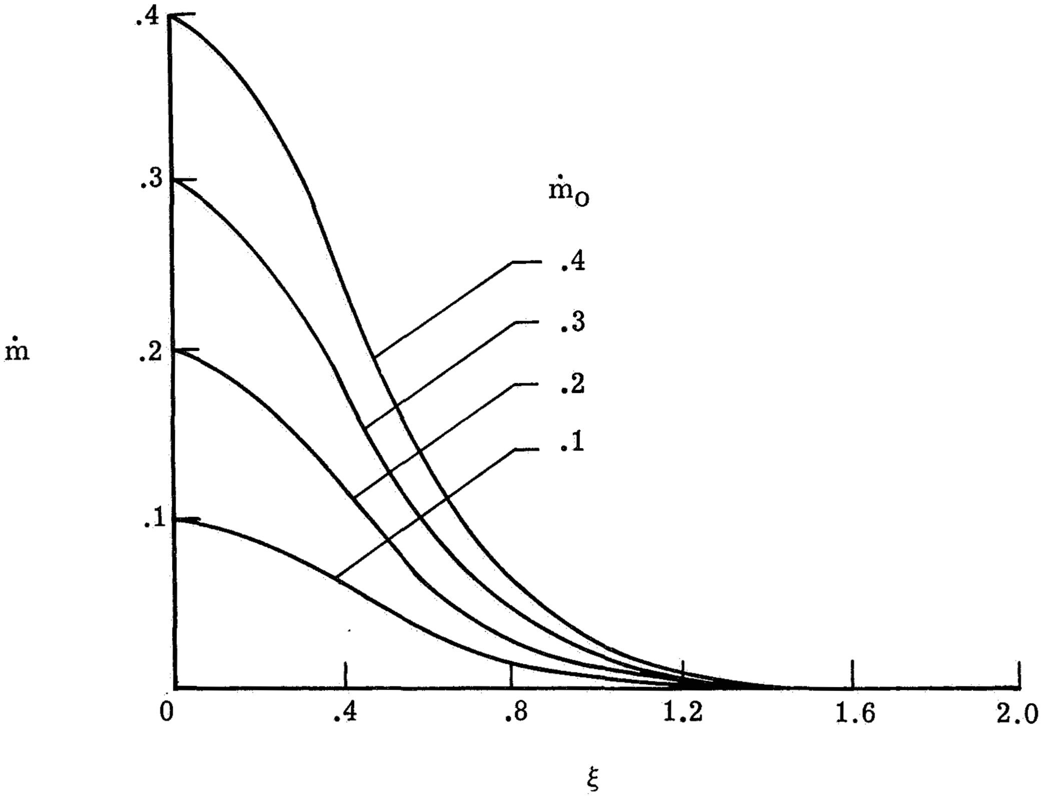

Figure 31.- Nondimensional mass-injection distributions.

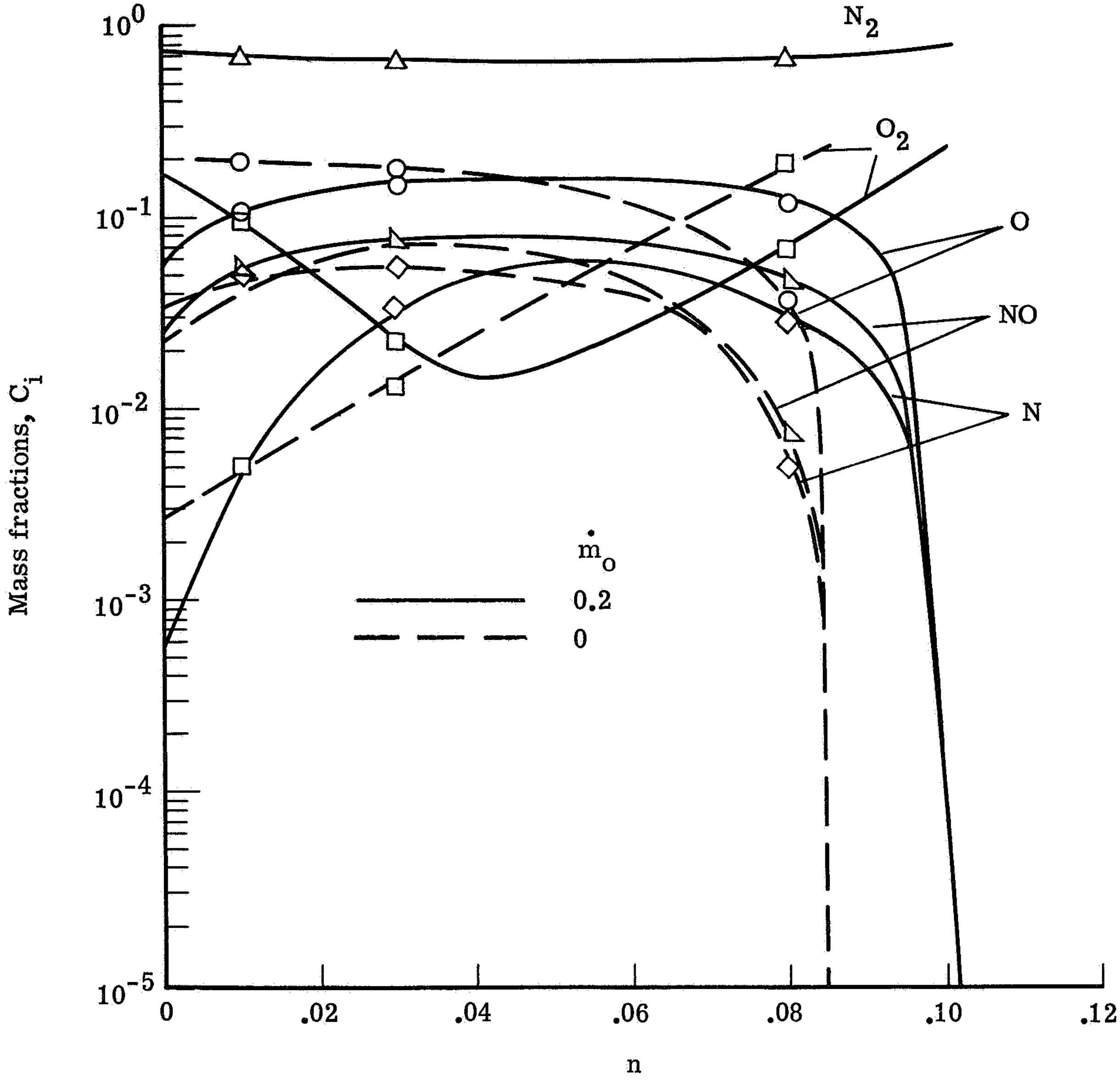

(a) $\xi = 0.0$.

Figure 32.- Comparison of nonequilibrium species profiles with and without mass injection of equilibrium air at an altitude of 60.96 km. $U_\infty^* = 6.10$ km/s; $T_w^* = 1500$ K; $a^* = 2.54$ cm; multicomponent diffusion; noncatalytic wall.

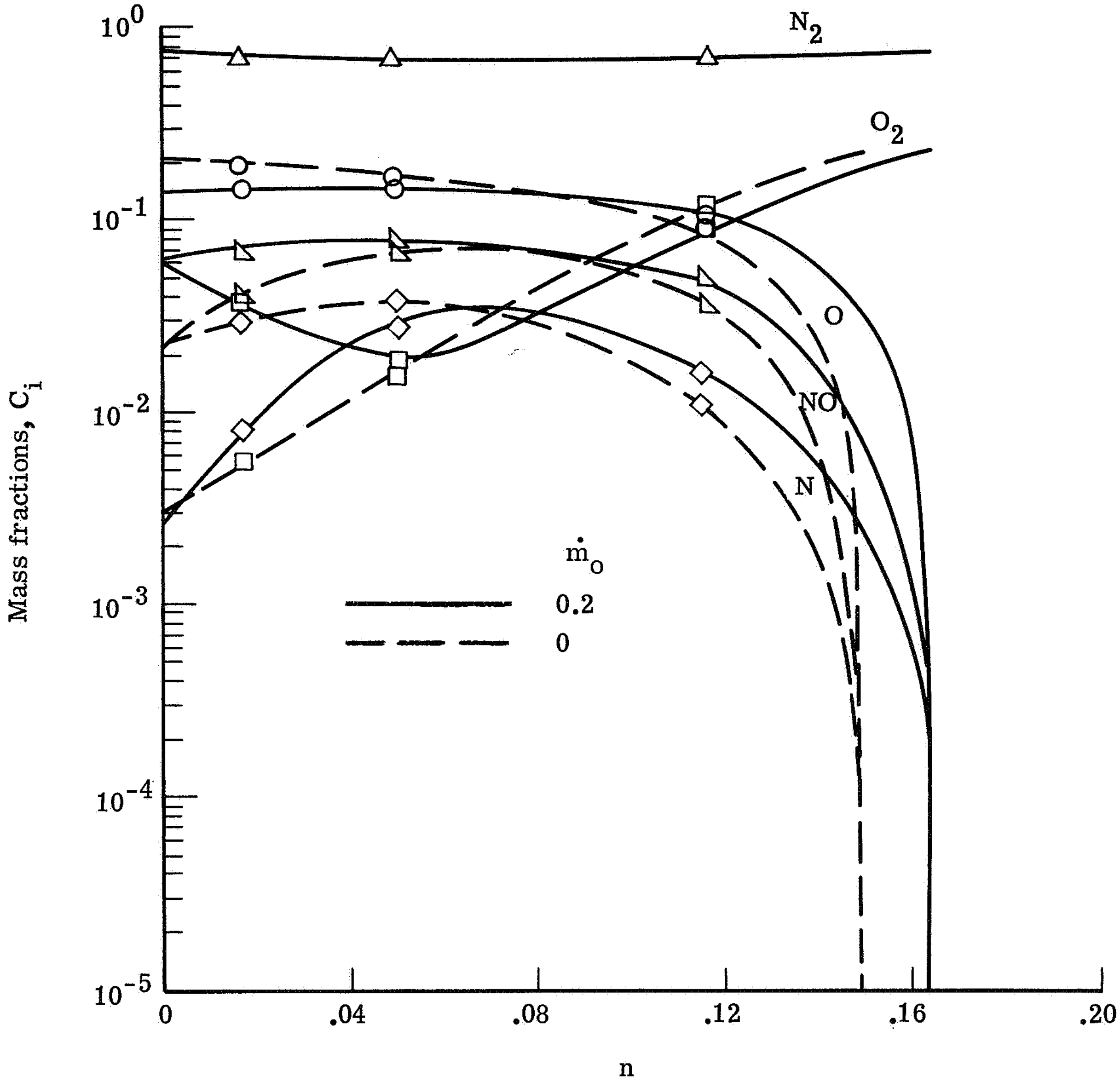

(b) $\xi = 1.0$.

Figure 32.- Continued.

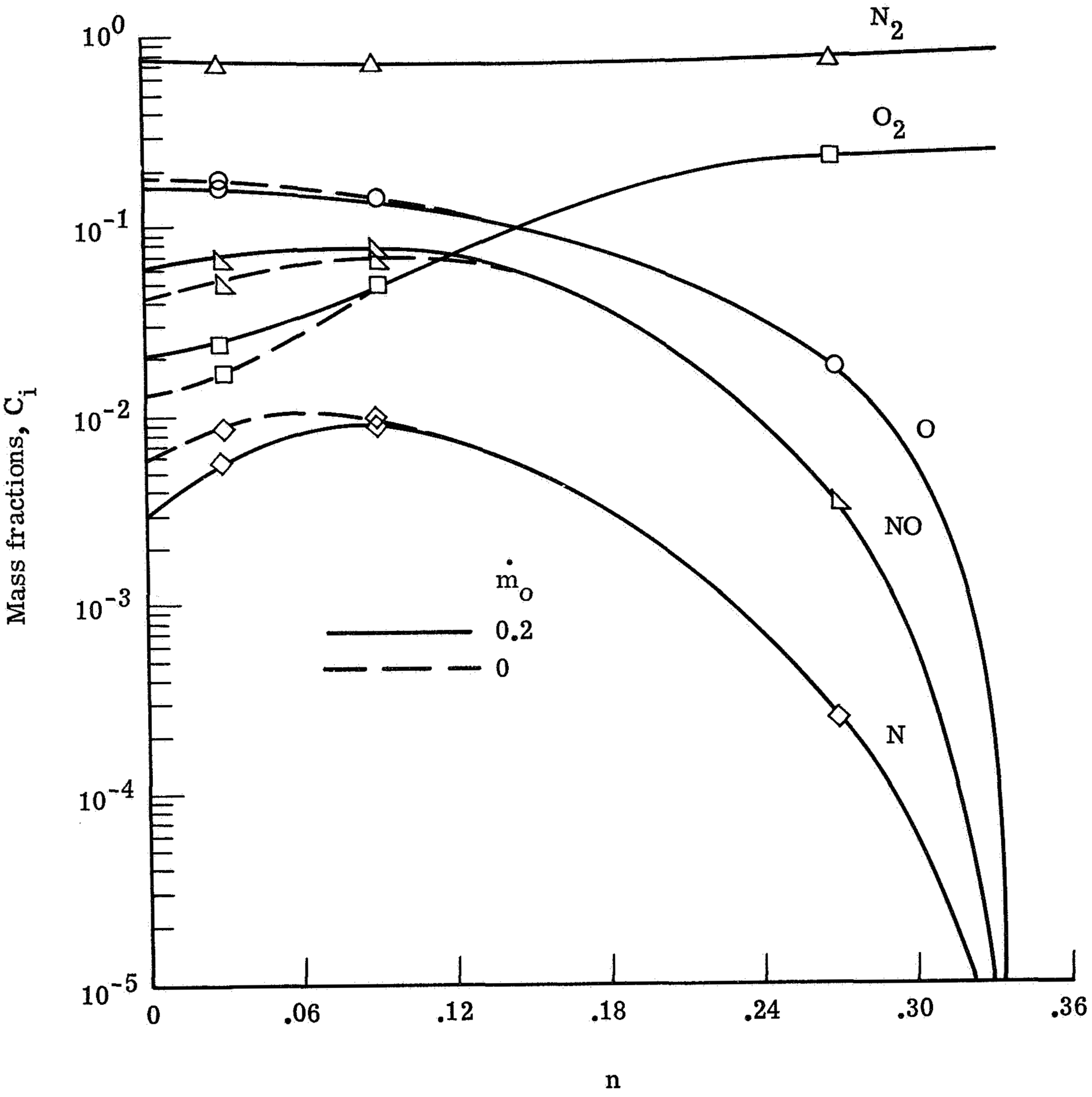

(c) $\xi = 3.0$.

Figure 32.- Concluded.

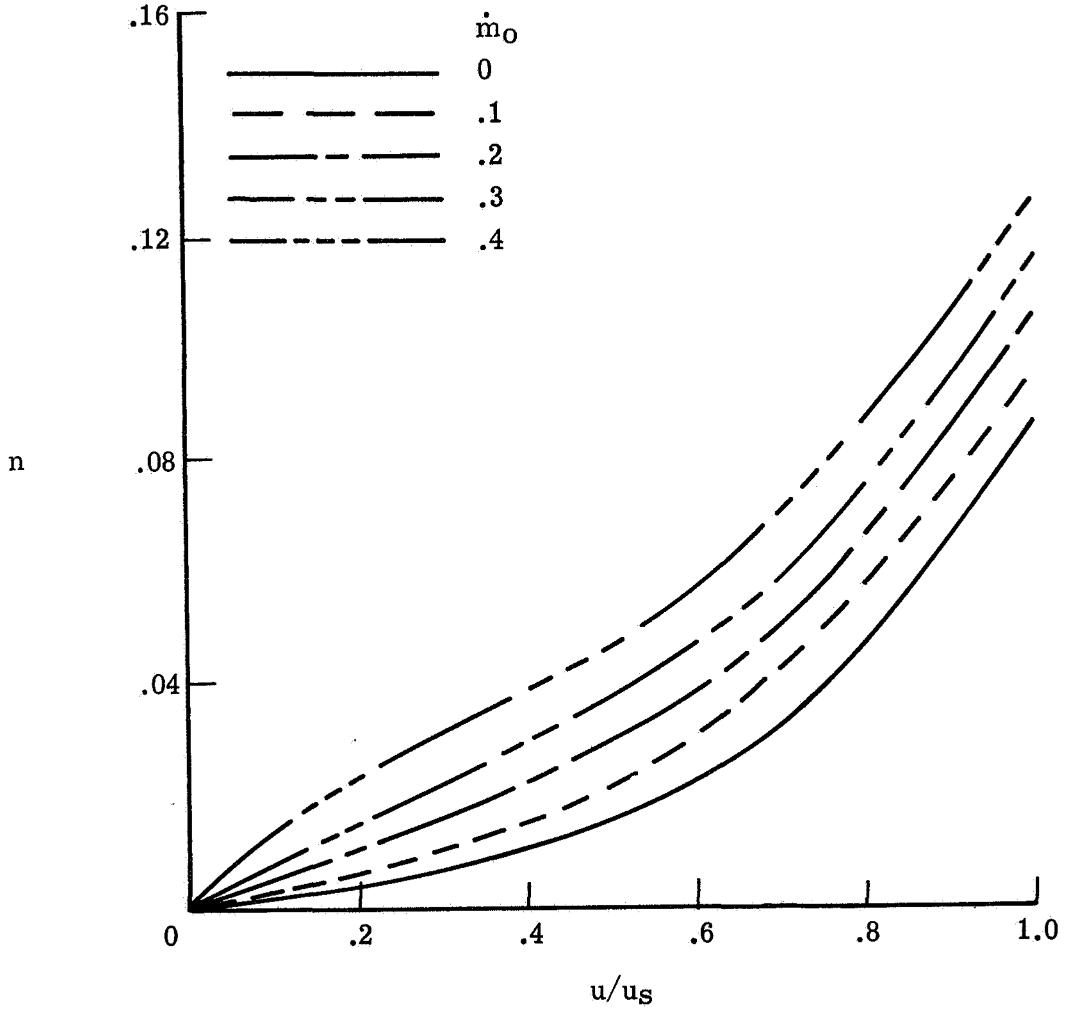

Figure 33.- Stagnation tangential velocity ratio profiles for different injection rates of equilibrium air into reacting nonequilibrium air at an altitude of 60.96 km. $U_\infty^* = 6.10$ km/s; $T_w^* = 1500$ K; $a^* = 2.54$ cm; multicomponent diffusion; noncatalytic wall.

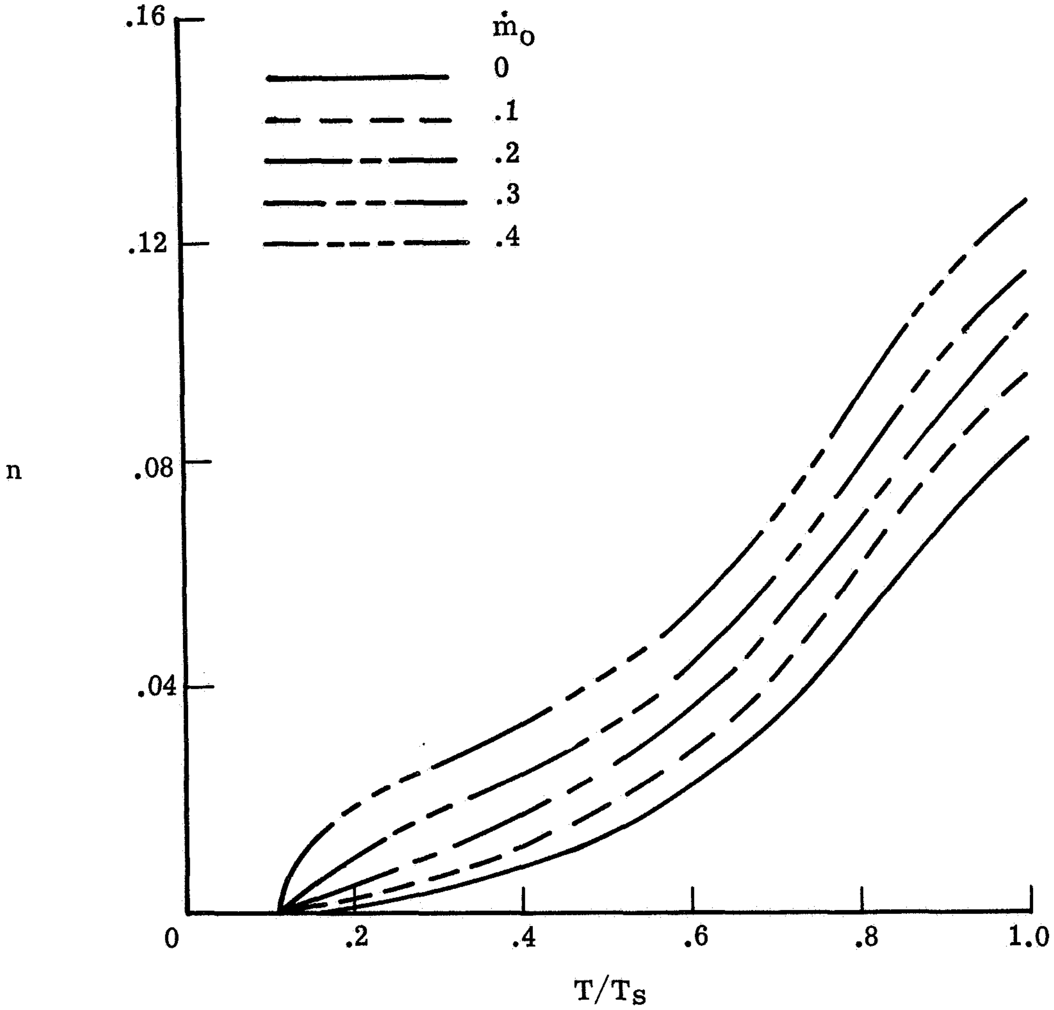

Figure 34.- Stagnation temperature profiles for different injection rates of equilibrium air into reacting nonequilibrium air at an altitude of 60.96 km. $U_\infty^* = 6.10$ km/s; $T_w^* = 1500$ K; $a^* = 2.54$ cm; multicomponent diffusion; noncatalytic wall.

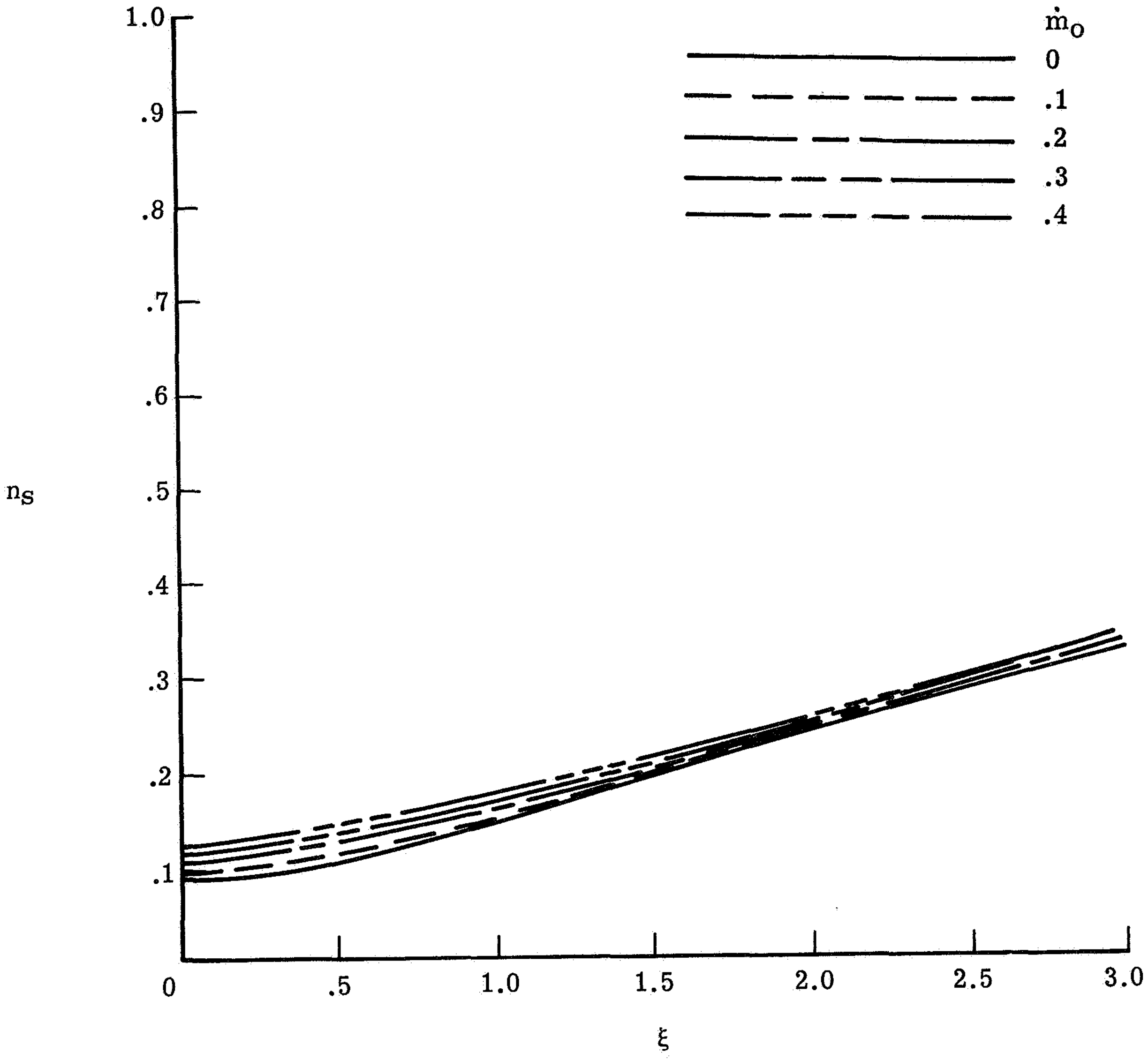

Figure 35.- Comparison of shock standoff distances for different injection rates of equilibrium air into reacting nonequilibrium air at an altitude of 60.96 km. $U_\infty^* = 6.10$ km/s; $T_w^* = 1500$ K; $a^* = 2.54$ cm; multicomponent diffusion; noncatalytic wall.

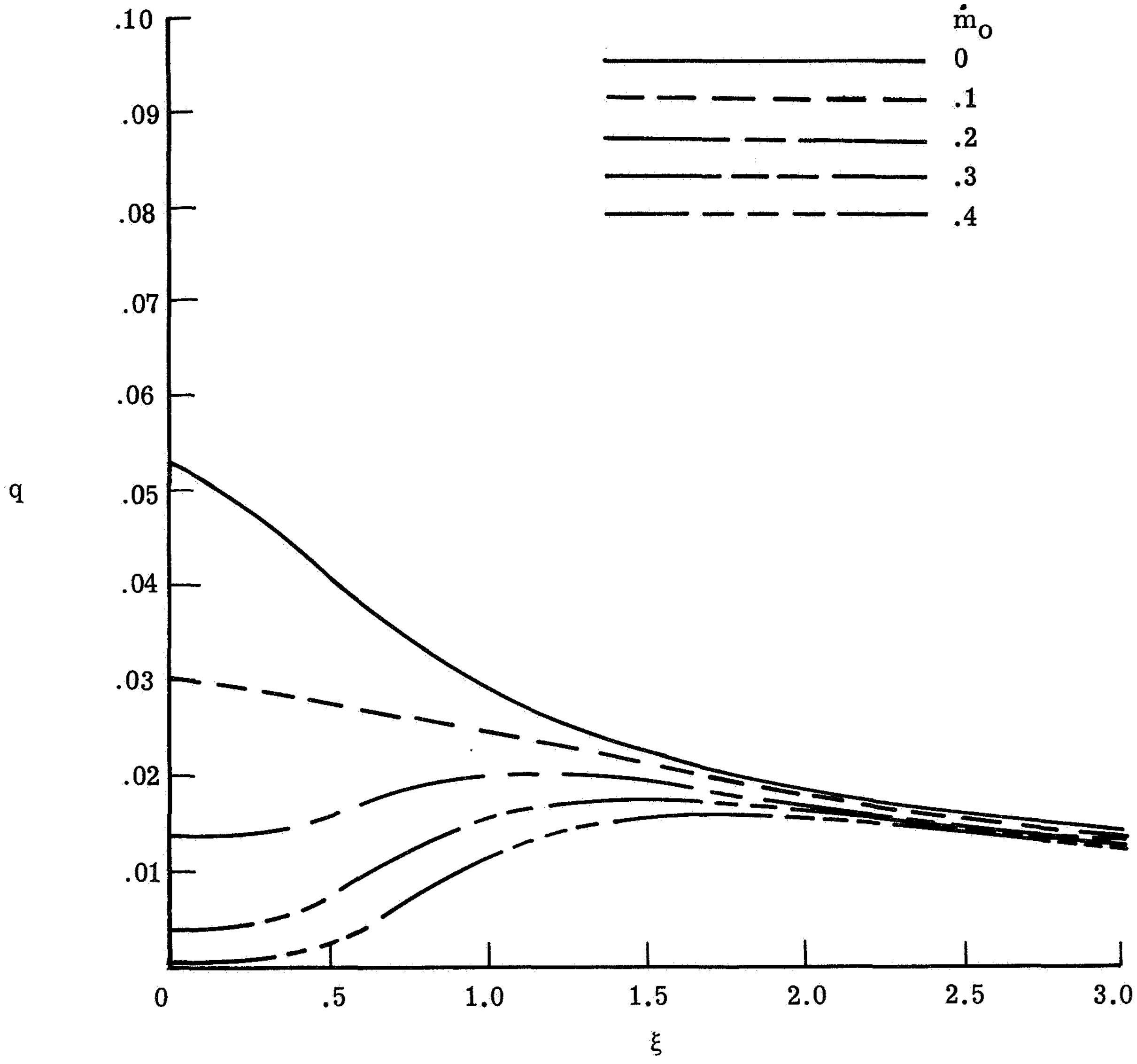

Figure 36.- Comparison of nondimensional heat-transfer distributions for different injection rates of equilibrium air into reacting nonequilibrium air at an altitude of 60.96 km. $U_\infty^* = 6.10$ km/s; $T_w^* = 1500$ K; $a^* = 2.54$ cm; multicomponent diffusion; noncatalytic wall.

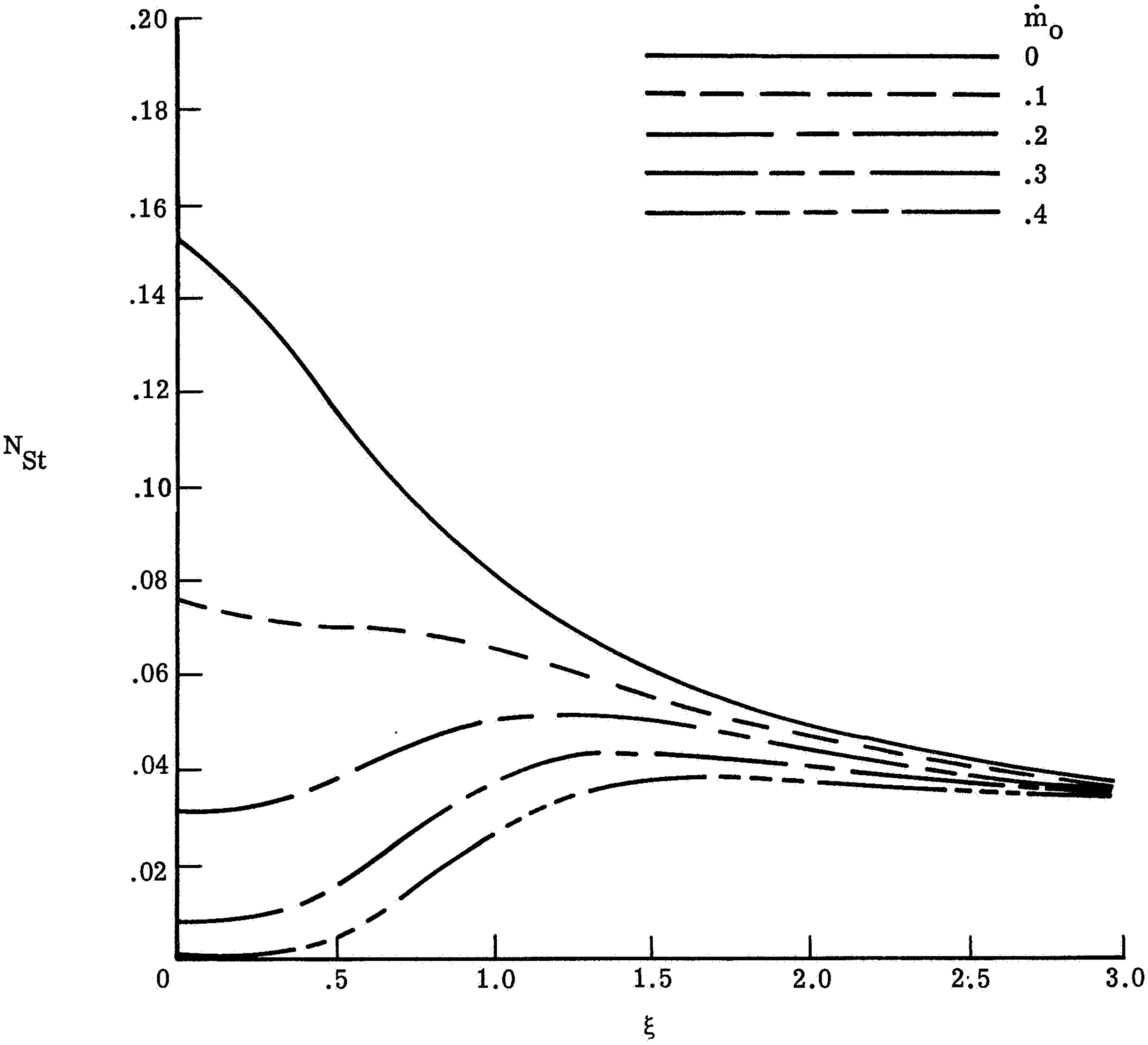

Figure 37.- Comparison of Stanton number distributions for different injection rates of equilibrium air into reacting nonequilibrium air at an altitude of 60.96 km. $U_\infty^* = 6.10$ km/s; $T_w^* = 1500$ K; $a^* = 2.54$ cm; multicomponent diffusion; noncatalytic wall.

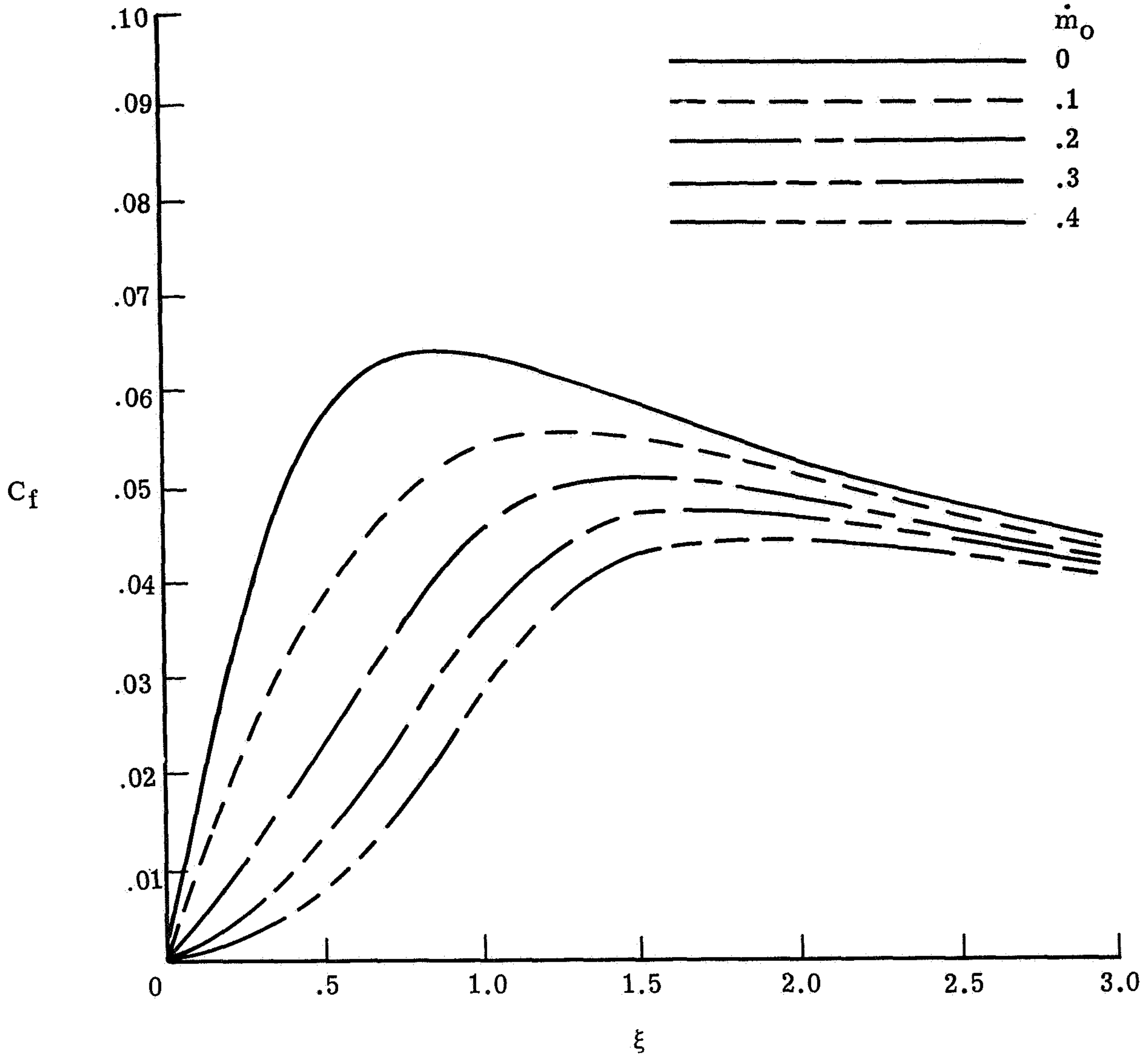

Figure 38.- Comparison of skin-friction coefficient distributions for different injection rates of equilibrium air into reacting nonequilibrium air at an altitude of 60.96 km. $U_\infty^* = 6.10$ km/s; $T_w^* = 1500$ K; $a^* = 2.54$ cm; multicomponent noncatalytic wall.

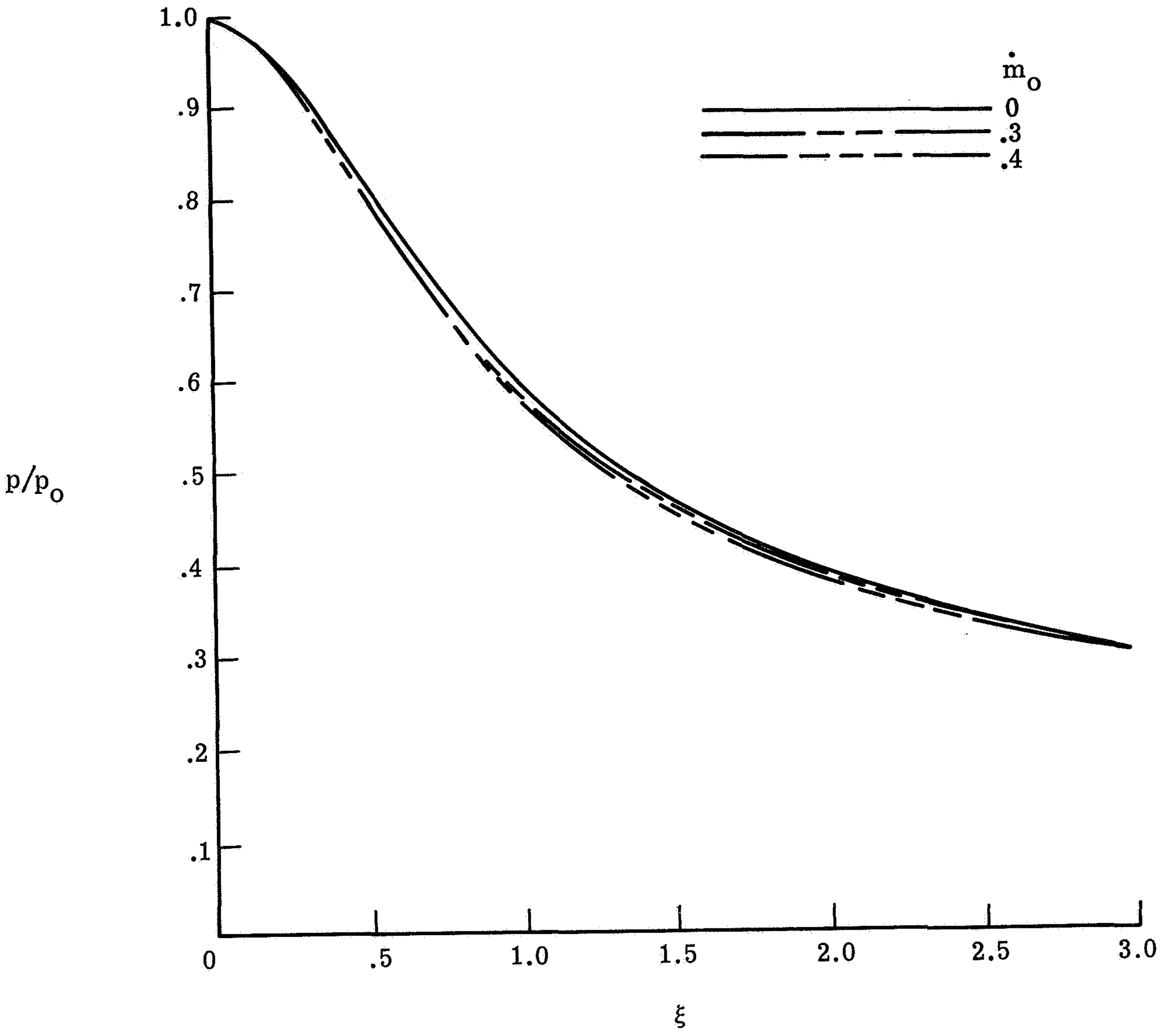

Figure 39.- Comparison of wall pressure ratio distributions for different injection rates of equilibrium air into reacting nonequilibrium air at ar altitude of 60.96 km. $U_\infty^* = 6.10$ km/s; $T_w^* = 1500$ K; $a^* = 2.54$ cm; multicomponent diffusion; noncatalytic wall.

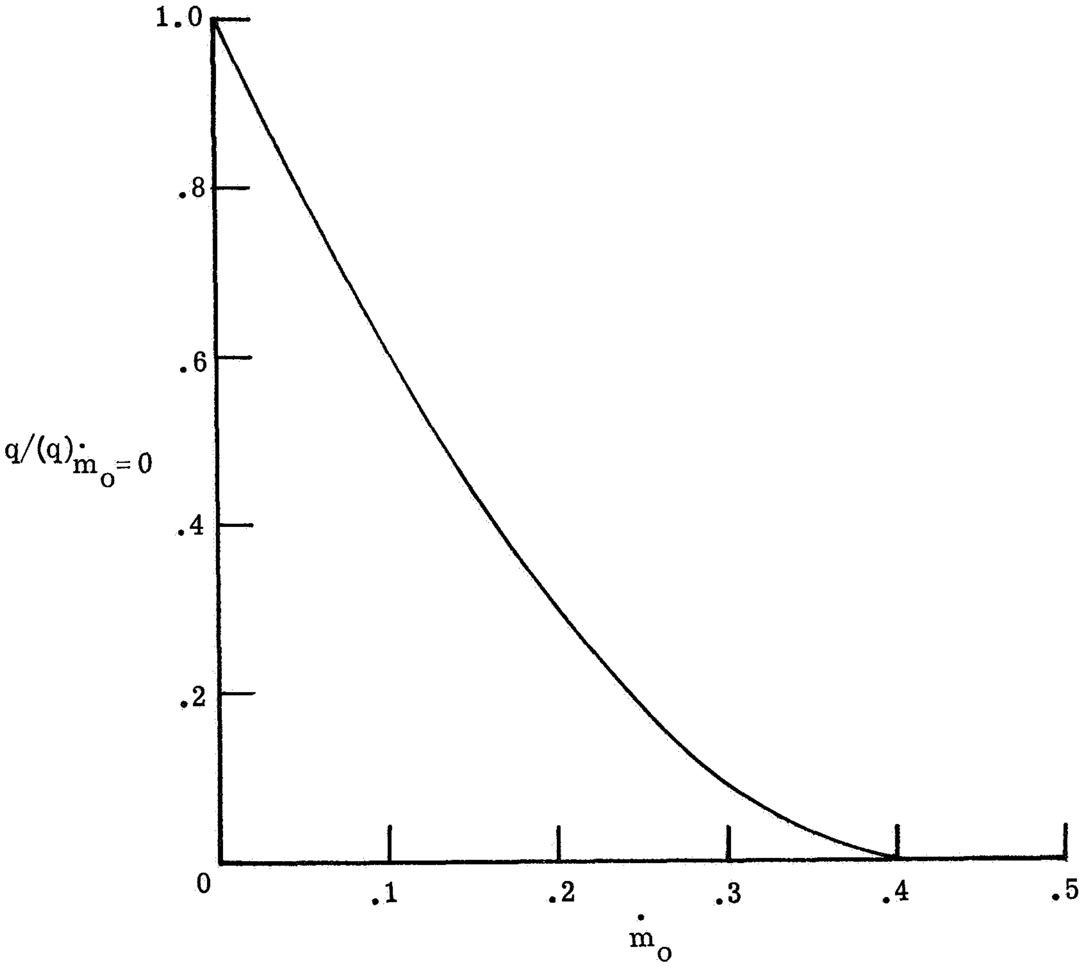

Figure 40.- Stagnation heat transfer as influenced by injecting equilibrium air into reacting equilibrium air at an altitude of 60.96 km. $U_\infty^* = 6.10$ km/s; $T_w^* = 1500$ K; $a^* = 2.54$ cm; binary diffusion.

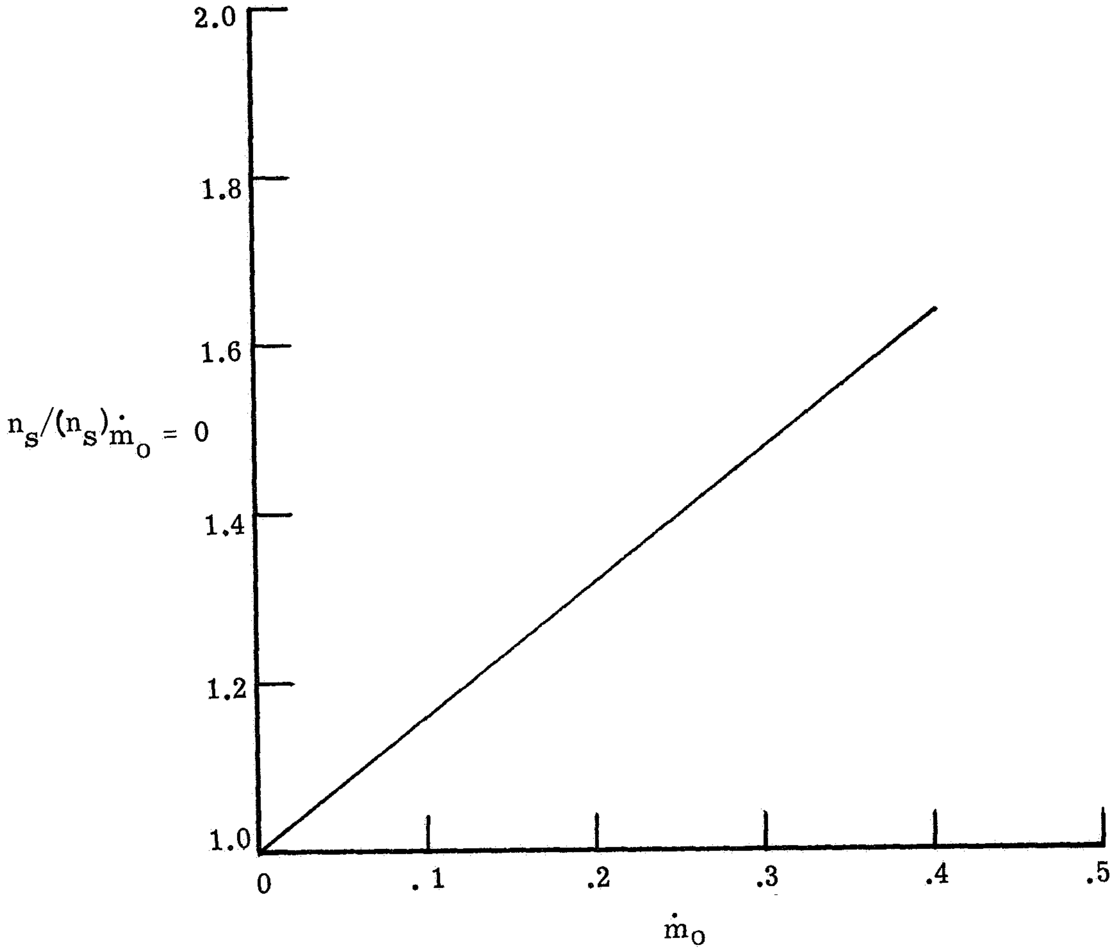

Figure 41.- Stagnation shock standoff distances as influenced by injection of equilibrium air into reacting equilibrium air at an altitude of 60.96 km. $U_\infty^* = 6.10$ km/s; $T_w^* = 1500$ K; $a^* = 2.54$ cm; binary diffusion.

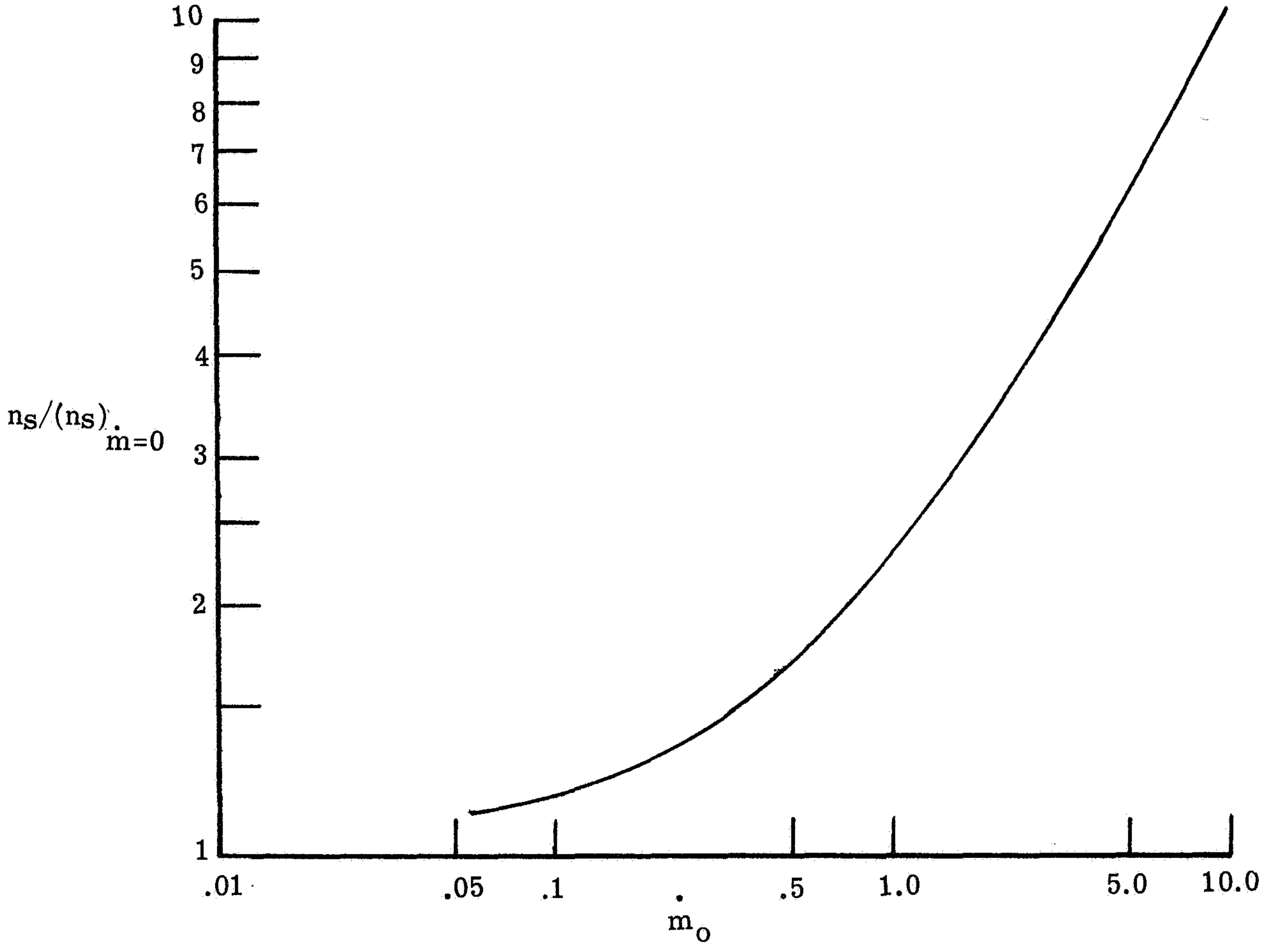

Figure 42.- Stagnation shock standoff distance as influenced by large mass injection rates of equilibrium air into reacting equilibrium air at an altitude of 60.96 km. $U_\infty^* = 6.10$ km/s; $T_w^* = 1500$ K; $a^* = 2.54$ cm; binary diffusion.

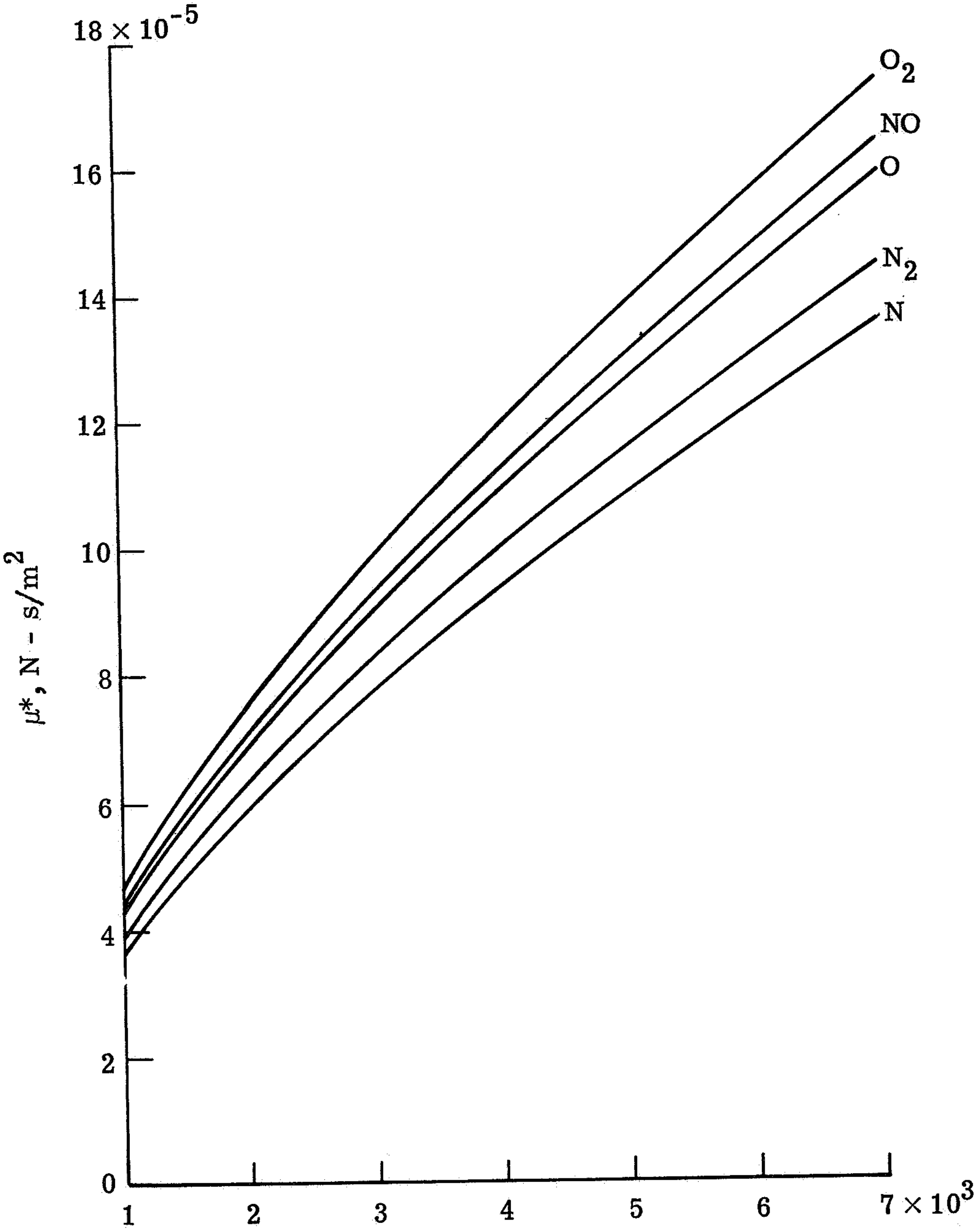

Figure 43.- Species viscosity.

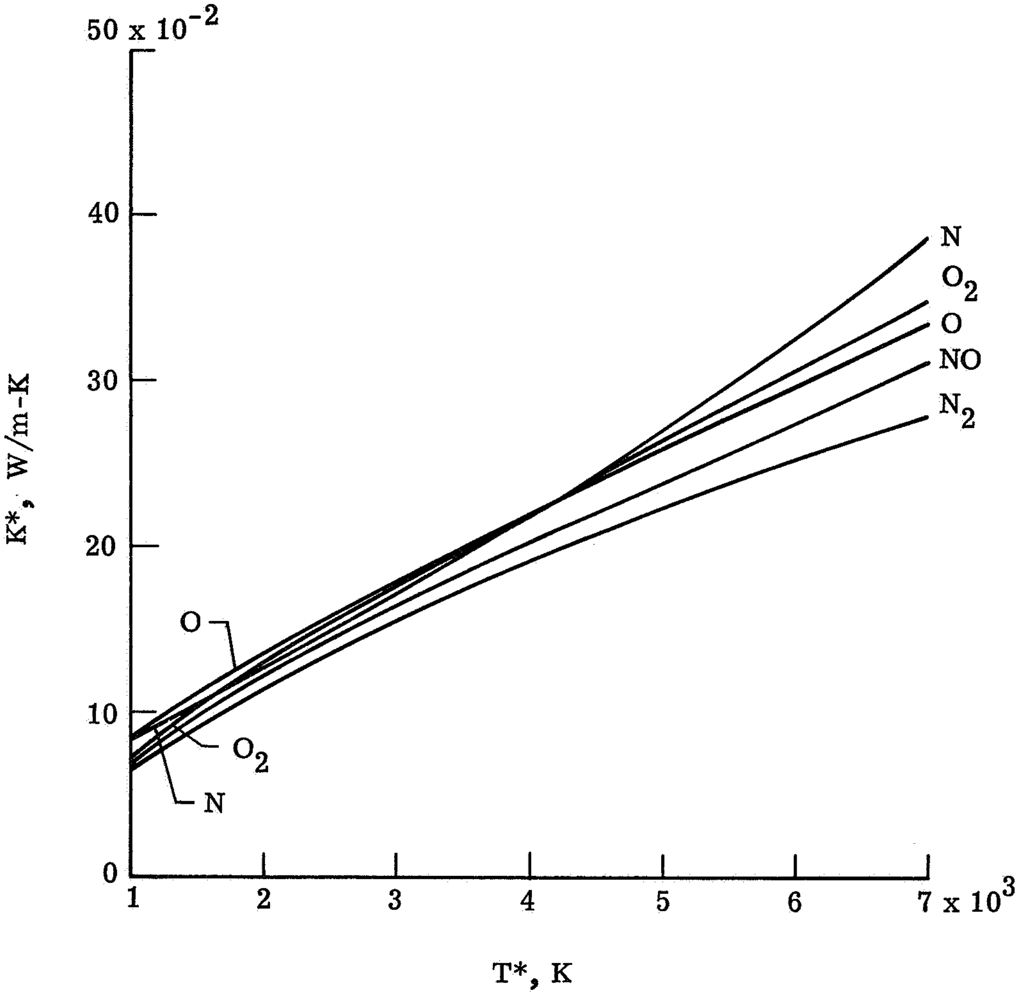

Figure 44.- Species thermal conductivity.

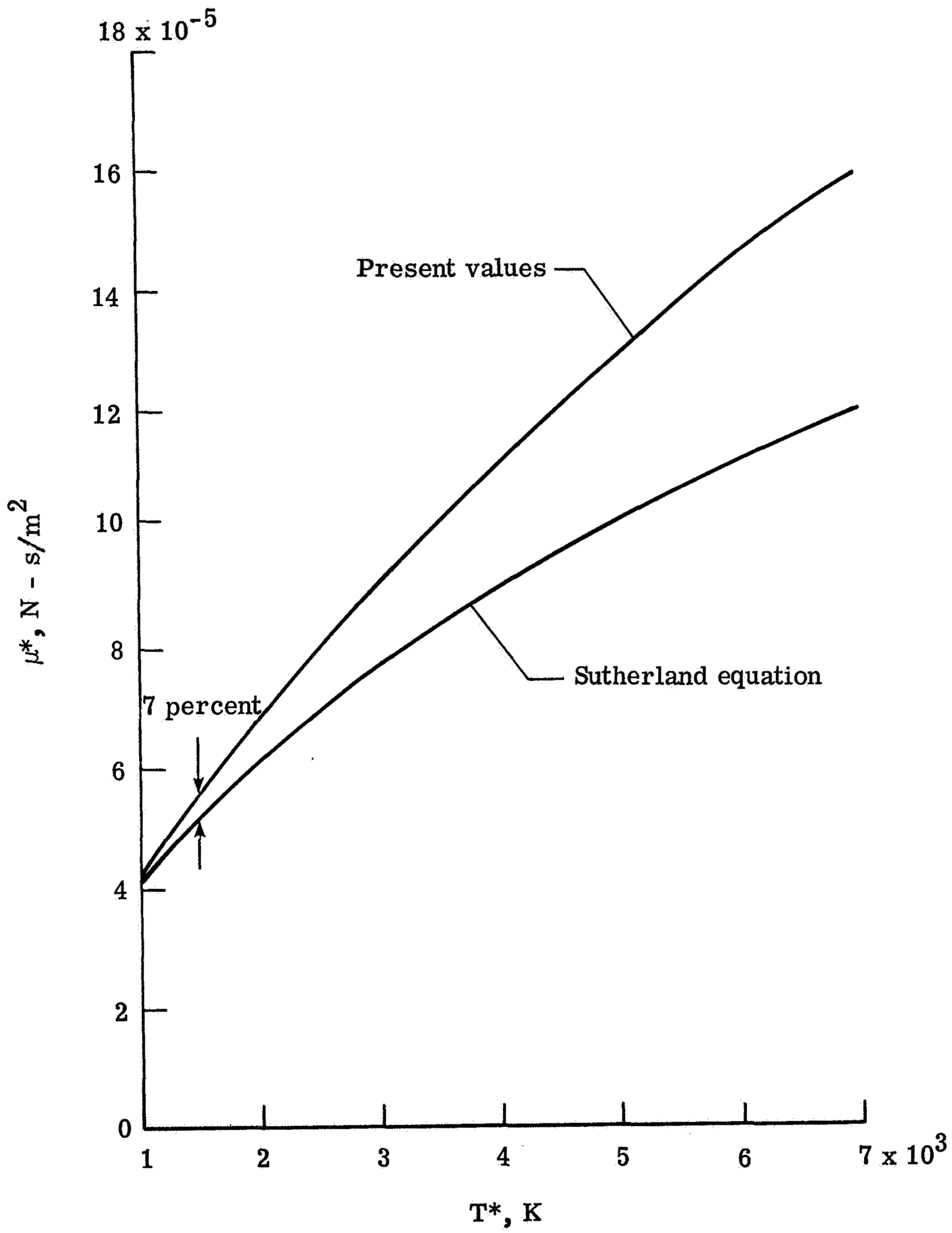

Figure 45.- Viscosity for equilibrium air at a pressure of 1 atmosphere.

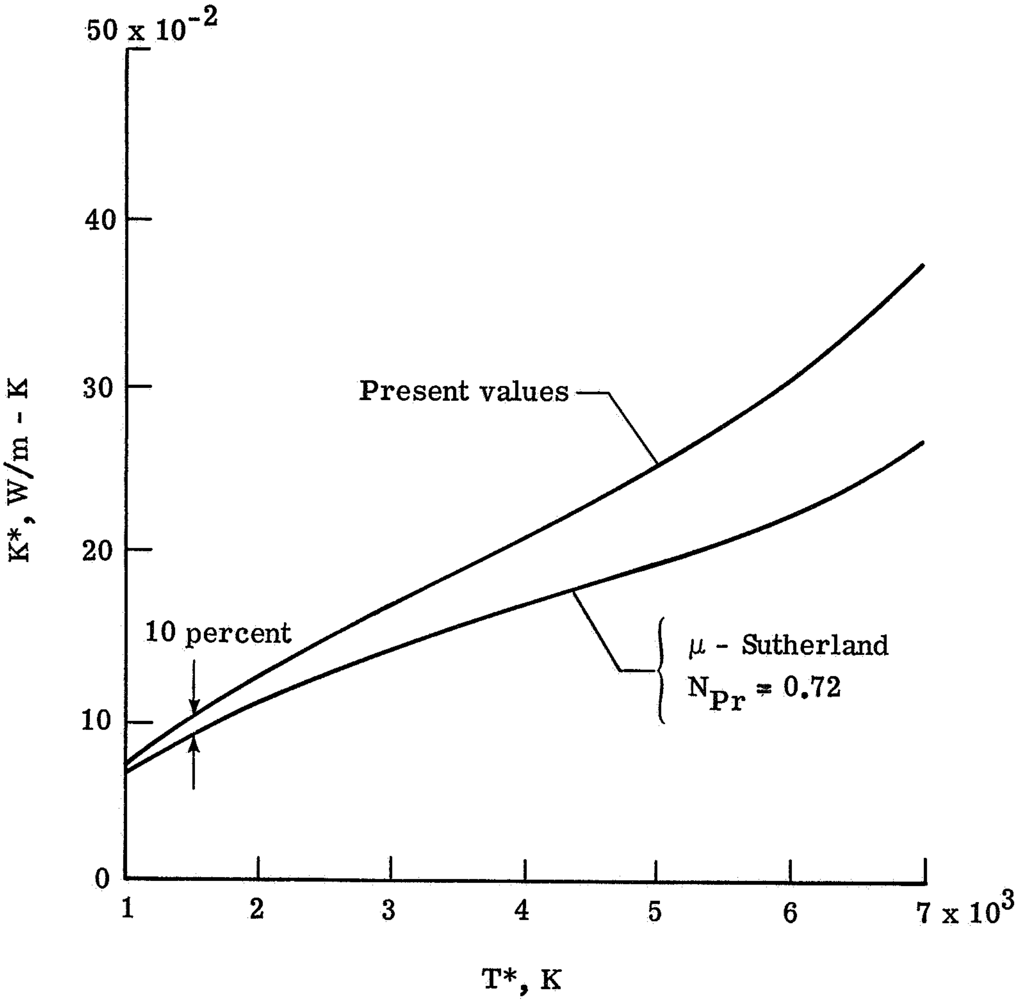

Figure 46.- Thermal conductivity of equilibrium air at a pressure of 1 atmosphere.

NASA-Langley, 1974 L-8861

NATIONAL AERONAUTICS AND SPACE ADMINISTRATION
WASHINGTON, D.C. 20546

OFFICIAL BUSINESS
PENALTY FOR PRIVATE USE $300

SPECIAL FOURTH-CLASS RATE
BOOK

POSTAGE AND FEES PAID
NATIONAL AERONAUTICS AND
SPACE ADMINISTRATION
451

U.S.MAIL

POSTMASTER: If Undeliverable (Section 158
Postal Manual) Do Not Return

> *"The aeronautical and space activities of the United States shall be conducted so as to contribute . . . to the expansion of human knowledge of phenomena in the atmosphere and space. The Administration shall provide for the widest practicable and appropriate dissemination of information concerning its activities and the results thereof."*
>
> —NATIONAL AERONAUTICS AND SPACE ACT OF 1958

NASA SCIENTIFIC AND TECHNICAL PUBLICATIONS

TECHNICAL REPORTS: Scientific and technical information considered important, complete, and a lasting contribution to existing knowledge.

TECHNICAL NOTES: Information less broad in scope but nevertheless of importance as a contribution to existing knowledge.

TECHNICAL MEMORANDUMS: Information receiving limited distribution because of preliminary data, security classification, or other reasons. Also includes conference proceedings with either limited or unlimited distribution.

CONTRACTOR REPORTS: Scientific and technical information generated under a NASA contract or grant and considered an important contribution to existing knowledge.

TECHNICAL TRANSLATIONS: Information published in a foreign language considered to merit NASA distribution in English.

SPECIAL PUBLICATIONS: Information derived from or of value to NASA activities. Publications include final reports of major projects, monographs, data compilations, handbooks, sourcebooks, and special bibliographies.

TECHNOLOGY UTILIZATION PUBLICATIONS: Information on technology used by NASA that may be of particular interest in commercial and other non-aerospace applications. Publications include Tech Briefs, Technology Utilization Reports and Technology Surveys.

Details on the availability of these publications may be obtained from:

SCIENTIFIC AND TECHNICAL INFORMATION OFFICE

NATIONAL AERONAUTICS AND SPACE ADMINISTRATION

Washington, D.C. 20546